

**TRAPPING BOUNDARIES AND DROPOUTS OF  
SOLAR ENERGETIC PARTICLES**

**ACHARA SERIPIENLERT**

**A THESIS SUBMITTED IN PARTIAL FULFILMENT  
OF THE REQUIREMENTS FOR  
THE DEGREE OF DOCTOR OF PHILOSOPHY  
(PHYSICS)  
FACULTY OF GRADUATE STUDIES  
MAHIDOL UNIVERSITY  
2010**

**COPYRIGHT OF MAHIDOL UNIVERSITY**

Thesis  
entitled

**TRAPPING BOUNDARIES AND DROPOUTS OF SOLAR  
ENERGETIC PARTICLES**

.....  
Ms. Achara Seripienlert  
Candidate

.....  
Prof. David Ruffolo,  
Ph.D. (Physics)  
Major advisor

.....  
Asst. Prof. Michael Allen,  
Ph.D. (Physics)  
Co-advisor

.....  
Asst. Prof. Tanakorn Osotchan,  
Ph.D. (Physics)  
Co-advisor

.....  
Prof. Banchong Mahaisavariya, M.D.  
Dean  
Faculty of Graduate Studies  
Mahidol University

.....  
Assoc. Prof. Wannapong Triampo,  
Ph.D. (Physics)  
Program Director  
Doctor of Philosophy Program  
in Physics  
Faculty of Science  
Mahidol University

Thesis  
entitled

**TRAPPING BOUNDARIES AND DROPOUTS OF SOLAR  
ENERGETIC PARTICLES**

was submitted to the Faculty of Graduate Studies, Mahidol University  
for the degree of Doctor of Philosophy (Physics)

on  
June 15, 2010

.....  
Ms. Achara Seripienlert  
Candidate

.....  
Lect. Piyanate Chuychai,  
Ph.D. (Physics)  
Chair

.....  
Prof. David Ruffolo,  
Ph.D. (Physics)  
Member

.....  
Asst. Prof. Tanakorn Osotchan,  
Ph.D. (Physics)  
Member

.....  
Asst. Prof. Michael Allen,  
Ph.D. (Physics)  
Member

.....  
Prof. Banchong Mahaisavariya, M.D.  
Dean  
Faculty of Graduate Studies  
Mahidol University

.....  
Prof. Skorn Mogkolsuk,  
Ph.D. (Biological Science)  
Dean  
Faculty of Science  
Mahidol University

## ACKNOWLEDGEMENTS

First of all, I wish to sincerely express my gratitude to my advisor, Prof. David Ruffolo, for always giving me supervision and encouragement during my graduate study. Without his guidance and rescue, I could not finish this work.

I would like to give my gratitude to my thesis committee, Dr. Piyanate Chuychai, Asst. Prof. Michael Allen, and Asst. Prof. Tanakorn Osotchan for their kind suggestions.

I would like to thank Asst. Prof. Michael Allen for the Latex template of this thesis, and Alejandro Sáiz for the IDL programming.

Much help during the work was provided by many people. I would like to thank Dr. Piyanate Chuychai and Dr. Paisan Tooprakai for discussions and suggestions about physics, turbulence and computer simulations. I would like to thank my collaborators: Mr. Wirin, Mr. Rakpong, Dr. Watcharawuth, Mr. Pat, and everyone in the Space Physics and Energetic Particles Lab.

I would like to thank Miss Suchada Kittirisopit for standing by me.

Finally I would like to thank my family that always supports and takes care of me.

Achara Seripienlert

**TRAPPING BOUNDARIES AND DROPOUTS OF SOLAR ENERGETIC PARTICLES.**

ACHARA SERIPIENLERT 4938556 SCPY/D

Ph.D. (PHYSICS)

THESIS ADVISORY COMMITTEE : DAVID RUFFOLO, Ph.D. (PHYSICS), MICHAEL ALLEN, Ph.D. (PHYSICS), TANAKORN OSOTCHAN, Ph.D. (PHYSICS)

**ABSTRACT**

As seen in recent observations by the *Advanced Composition Explorer (ACE)*, the intensity of solar energetic particles (SEPs) exhibits sudden, large changes known as dropouts. These have been explained in terms of turbulence or a flux tube structure in the solar wind. Computer simulations of a random-phase model of magnetic turbulence have indicated a spatial association between dropout features and local trapping boundaries (LTBs) defined for a two-dimensional (2D) + slab model of turbulence. Previous observations have shown that dropout features are not strongly associated with sharp magnetic field changes, as might be expected in the flux tube model. Random-phase turbulence models do not properly treat sharp changes in the magnetic field, such as current sheets, and thus cannot be tested in this way. Here we explore the properties of a more realistic two-dimensional magnetohydrodynamic (2D MHD) turbulence model, in which current sheets develop and the current and magnetic field have characteristic non-Gaussian statistical properties. For this model, computer simulations indicate that sharp particle gradients should frequently be associated with LTBs, sometimes with strong 2D magnetic fluctuations, and infrequently with current sheets. Thus the 2D MHD + slab model of turbulent fluctuations includes some realistic features of the flux tube view.

Besides simulations in Cartesian geometry, we also perform simulations of particle transport using a 2D MHD + slab model in spherical geometry, including particle focusing. We have discovered collimation of beams of charged particles toward a high (low) potential for a positive (negative) charge. In the solar wind, this should occur only for relativistic particles. For future work, we will investigate whether this effect can be applied to help understand the highest energy SEPs.

**KEY WORDS : SOLAR ENERGETIC PARTICLES / MAGNETIC TURBULENCE  
TRAPPING BOUNDARIES / COLLIMATION**

103 pages.

ขอบเขตการกักและครอปเอาต์ของอนุภาคพลังงานสูงจากดวงอาทิตย์

TRAPPING BOUNDARIES AND DROPOUTS OF SOLAR ENERGETIC PARTICLES

อัจฉรา เสรีเพียรเลิศ 4938556 SCPY/D

ปร.ด. (ฟิสิกส์)

คณะกรรมการที่ปรึกษาวิทยานิพนธ์: เดวิด รูฟโฟโล, Ph.D. (PHYSICS), ไมเคิล อลีน, Ph.D. (PHYSICS), ธนากร โอสดจันทร, Ph.D. (PHYSICS)

บทคัดย่อ

จากผลการสังเกตอนุภาคพลังงานสูงจากดวงอาทิตย์ด้วยยานอวกาศแอดวานซ์คอมโพสิชันเอ็กพลอเรอร์ พบการเปลี่ยนแปลงความเข้มของอนุภาคอย่างรวดเร็วเรียกว่าครอปเอาต์ ซึ่งสามารถอธิบายได้ด้วยความปั่นป่วนหรือโครงสร้างท่อฟลักซ์ในลมสุริยะ จากการจำลองด้วยคอมพิวเตอร์โดยแบบจำลองเฟสสุมของสนามแม่เหล็กปั่นป่วน พบความเกี่ยวข้องระหว่างลักษณะของครอปเอาต์และขอบเขตการกักในบริเวณใกล้เคียงซึ่งนิยามสำหรับแบบจำลองสนามแม่เหล็กปั่นป่วนแบบสองมิติ + แบบแผ่น จากการสังเกตที่ผ่านมาพบว่าครอปเอาต์ไม่มีความเกี่ยวข้องมากนักกับการเปลี่ยนแปลงที่ฉับพลันของสนามแม่เหล็กที่พบจากแบบจำลองท่อฟลักซ์ เนื่องจากแบบจำลองเฟสสุมของสนามแม่เหล็กแบบปั่นป่วนไม่สามารถให้การเปลี่ยนแปลงที่ฉับพลันของสนามแม่เหล็กที่สามารถเกิดขึ้นในแบบจำลองแผ่นกระแสดังนั้นจึงไม่สามารถใช้ทดสอบได้ในกรณีนี้ ในงานนี้เราได้สำรวจสมบัติของแบบจำลองที่ใกล้เคียงความจริงมากขึ้นอย่างแบบจำลองอุทกพลศาสตร์เชิงแม่เหล็กในสองมิติ ซึ่งสามารถเกิดแผ่นกระแสดังขึ้นได้ แผ่นกระแสดและสนามแม่เหล็กนี้มีสมบัติทางสถิติไม่เป็นแบบเกาส์เซียน การคำนวณด้วยคอมพิวเตอร์โดยใช้แบบจำลองนี้ได้แสดงให้เห็นว่าในบริเวณที่พบครอปเอาต์ก็จะมักพบขอบเขตการกักในบริเวณใกล้เคียงด้วย เราพบครอปเอาต์กับความปั่นป่วนของสนามแม่เหล็กแบบสองมิติที่แรงบางบริเวณ และไม่พบครอปเอาต์กับแผ่นกระแสดในบริเวณใกล้เคียงกัน ดังนั้นแบบจำลองใหม่นี้ได้รวมความสมจริงของผลจากการสังเกตของมุมมองโครงสร้างท่อฟลักซ์ไว้ด้วย

นอกจากการจำลองในเรขาคณิตพิกัดฉากแล้ว ในงานนี้เรายังได้ทำการจำลองการขนส่งของอนุภาคในสนามแม่เหล็กที่ใช้แบบจำลองอุทกพลศาสตร์เชิงแม่เหล็กในสองมิติ + แบบแผ่นในเรขาคณิตพิกัดทรงกลมซึ่งจะรวมกระบวนการโฟกัสของอนุภาคด้วย เราค้นพบปรากฏการณ์ร่วมกับเป็นลำของอนุภาคมีประจุที่บริเวณศักย์สูง (ด้า) สำหรับอนุภาคประจุบวก (ลบ) ในลมสุริยะปรากฏการณ์นี้จะเกิดกับอนุภาคพลังงานสูงมากเท่านั้น ในอนาคตเราหวังว่าจะสามารถประยุกต์ใช้ปรากฏการณ์นี้อธิบายผลการสังเกตอนุภาคที่มีระดับพลังงานสูงสุดจากดวงอาทิตย์

## CONTENTS

	<b>Page</b>
<b>ACKNOWLEDGEMENTS</b>	<b>iii</b>
<b>ABSTRACT (ENGLISH)</b>	<b>iv</b>
<b>ABSTRACT (THAI)</b>	<b>v</b>
<b>LIST OF TABLES</b>	<b>ix</b>
<b>LIST OF FIGURES</b>	<b>x</b>
<b>CHAPTER I Introduction</b>	<b>1</b>
1.1 Solar Events	1
1.2 Solar Wind	2
1.3 Interplanetary Magnetic Field	3
1.4 Solar Energetic Particles and Dropouts	6
1.5 Local Trapping Boundaries and Current Sheets	9
1.6 Motivation and Objectives of This Study	10
1.7 Outline of the Thesis	12
<b>CHAPTER II Theoretical Background and Literature Review</b>	<b>13</b>
2.1 Turbulence	13
2.2 Magnetohydrodynamics	16
2.2.1 General	16
2.2.2 Waves	18
2.2.3 Magnetic Reconnection	21
2.3 Magnetohydrodynamic Turbulence in the Solar Wind	22
2.4 Literature Review	25
<b>CHAPTER III Existing Numerical Techniques</b>	<b>32</b>
3.1 Magnetic Field Model	32
3.1.1 Cartesian Geometry	32
3.1.2 Spherical Geometry	33

## CONTENTS (cont.)

	<b>Page</b>
3.2 Slab Field Generation	34
3.3 2D Field Generation	36
3.3.1 2D Random-Phase Field	36
3.3.2 2D MHD Field	37
3.4 Field Line Tracing	39
3.4.1 Cartesian Geometry	39
3.4.2 Spherical Geometry	40
3.5 Particle Tracing	42
3.5.1 Cartesian Geometry	42
3.5.2 Spherical Geometry	44
<b>CHAPTER IV New Numerical Simulation Techniques</b>	<b>45</b>
4.1 Test with a Uniform Magnetic Field in the $x$ Direction	46
4.2 Test with a Radial Field	47
4.3 Finding LTBs	54
<b>CHAPTER V Local Trapping Boundaries in a 2D MHD + Slab Field</b>	<b>56</b>
5.1 Characteristics of the 2D MHD Field	57
5.2 Reasons for Dropout Features	64
5.3 Associations with Dropout Features	66
<b>CHAPTER VI Collimation of Particle Trajectories in Spherical Geometry</b>	<b>70</b>
6.1 Low-Energy Particle Trajectories and Dropouts	70
6.2 Collimation of Particle Beams in a Gaussian Flux Rope	71
6.2.1 Simulations	71
6.2.2 Theory	76
6.3 Simulation of Collimation of Particle Beams by 2D Turbulent Structure	79
6.3.1 Pure 2D Turbulence	79
6.3.2 2D MHD + Slab Turbulence	81



**CONTENTS (cont.)**

	<b>Page</b>
<b>CHAPTER VII</b> Conclusions	<b>83</b>
<b>REFERENCES</b>	<b>85</b>
<b>APPENDIX A</b> Non-dimensionalization	<b>93</b>
<b>APPENDIX B</b> Derivation of Equations of Particle Motion in Spherical Geometry	<b>95</b>
<b>APPENDIX C</b> Curvature Drift in a Conical Flux Rope: Hamiltonian Approach	<b>100</b>
<b>BIOGRAPHY</b>	<b>103</b>

## LIST OF TABLES

<b>Tables</b>	<b>Page</b>
4.1 Gyro-radius of protons at various energies for initial input and also for $B = 5$ nT (at $r = 1.0$ AU) from theory, simulations and from graphs.	52
4.2 Gyro-frequency of protons at various energies for initial input and also for $B = 5$ nT (at $r = 1.0$ AU) from theory, simulations and from graphs.	53
5.1 Moments of various quantities for magnetic field models	63

## LIST OF FIGURES

<b>Figures</b>	<b>Page</b>
1.1 Observation of an impulsive flare event at the Sun. [Image credit: Yohkoh Soft X-Ray Telescope]	2
1.2 A large coronal mass ejection (CME) on 20 April 1998. A disk blocks the Sun so that the LASCO instrument can observe the structures of the CME and the corona in visible light. The white circle represents the size and position of the Sun. [Image credit: SOHO observatory (NASA/ESA)]	3
1.3 Observed solar wind from SOHO during solar minimum. [Image credit: SOHO]	4
1.4 Structures of magnetic fields of the sun during solar minimum. [Image credit: Cravens 1997]	5
1.5 Warped current sheets. [Image credit: J. R. Jokipii, University of Arizona]	6
1.6 Illustration of plasma and magnetic fields in the inner solar system. Blue arrows indicate solar wind flow. Green lines are interplanetary magnetic field lines and the blue line indicates particle motion.	7
1.7 Energetic particle velocity dispersion and interplanetary magnetic field direction during 1999 January 9-10. (a) H to Fe ion energy versus time; (b) histogram of ion count rate; (c) magnetic field azimuth direction in geocentric-solar-ecliptic (GSE) coordinates; (d) GSE magnetic field altitude direction. [Image credit: Mazur et al. 2000]	8
1.8 Illustration of interplanetary magnetic field lines populated with SEPs from a localized source region near the Sun. The field lines are filamented according to the small scale topology of solar wind turbulence. [Image credit: Ruffolo et al. 2003]	9
2.1 The spectrum of turbulence from Kolmogorov theory.	15
2.2 Schematic Alfvén wave.	20
2.3 Schematic magnetosonic wave.	20

## LIST OF FIGURES (cont.)

Figures	Page
2.4 (a) Field lines with opposite directions moving toward each other. (b) Neutral region (green shading), where the magnetic diffusion is high and magnetic field lines are reconnecting. (c) New topology of the magnetic field lines.	22
2.5 (a) Plasma regions with opposed magnetic fields flow into each other. (b) There are 2 $X$ -points, $X_1$ and $X_2$ . (c) A neutral current sheet occurs between the incoming flows.	23
2.6 Schematic of Sweet-Parker magnetic reconnection.	24
2.7 Power spectrum of magnetic field fluctuations from a 74-minute interval of 0.12-second-averaged <i>Mariner 10</i> magnetometer data. [Image credit: Goldstein et al. 1995]	25
2.8 Contour plot of the two-dimensional correlation function of solar wind fluctuations as a function of distance parallel and perpendicular to the mean magnetic field using <i>ISEE 3</i> magnetometer data. [Image credit: Matthaeus et al. 1990]	26
2.9 Schematic of populations of fluctuations in the solar wind.	26
2.10 Contour plot of the potential function $a(x, y)$ for a representation of 2D turbulence, indicating O-points and X-points. [Image credit: Chuychai et al. 2007]	28
2.11 Scatter plots of magnetic field line trajectories at various distances $z$ . [Image credit: Chuychai et al. 2007]	30
3.1 Illustration of slab fluctuations, $\mathbf{b}^{slab}(z)$ .	33
3.2 An example of contour plot of a 2D potential function $a(x, y)$ . Arrows indicate directions of magnetic fields. Darker shading represents higher values of the potential function, whereas lighter shading represents lower values of the potential function. Near a maximum of the potential function, the magnetic field lines will go in the counter-clockwise direction. On the other hand, near minimum values of the potential function, the magnetic field lines will go in the clockwise direction.	34

## LIST OF FIGURES (cont.)

Figures	Page
3.3	Coordinates for simulations in spherical geometry. <span style="float: right;">35</span>
3.4	(a) Contour plot of a 2D random-phase potential function. (b) Same field after a 2D MHD procedure. <span style="float: right;">37</span>
3.5	Example of two trajectories of magnetic field lines in pure slab turbulence. <span style="float: right;">40</span>
3.6	Example of a trajectory of a magnetic field line in pure 2D turbulence. <span style="float: right;">41</span>
3.7	Example of two trajectories of magnetic field lines in 2D+slab turbulence. <span style="float: right;">42</span>
3.8	Example of a trajectory of a magnetic field line in spherical geometry. <span style="float: right;">43</span>
4.1	Components of $\hat{\Lambda}$ in spherical geometry. <span style="float: right;">45</span>
4.2	Test particles of 1 GeV in (a) spherical geometry and transforming to (b) Cartesian coordinates. <span style="float: right;">46</span>
4.3	Trajectories of particles in the $y$ - $z$ plane vs. time. The gyromotions are circles (shown in grey color) moving clockwise with time. <span style="float: right;">47</span>
4.4	Upper panel shows $\varphi$ versus time and lower panel shows $\Lambda$ versus time from simulations of 1 MeV protons. <span style="float: right;">49</span>
4.5	Upper panel shows $\varphi$ versus time and lower panel shows $\Lambda$ versus time from simulations of 10 MeV protons. <span style="float: right;">50</span>
4.6	Upper panel shows $\varphi$ versus time and lower panel shows $\Lambda$ versus time from simulations of 100 MeV protons. <span style="float: right;">51</span>
4.7	Upper panel shows $\varphi$ versus time and lower panel shows $\Lambda$ versus time from simulations of 1 GeV protons. <span style="float: right;">52</span>

## LIST OF FIGURES (cont.)

Figures	Page
5.1 A 2D component of magnetic turbulence can be defined in terms of an irregular potential function $a(x, y)$ , whose curl is $\mathbf{b}^{2D}$ . We compare contours of constant potential, i.e., magnetic flux surfaces, for (a) a 2D random-phase field, in which $a$ is a random function with a turbulent power spectrum, and (b) the same field after a 2D MHD procedure. A darker shading indicates a higher value of $a$ . For the 2D MHD field, the contours of constant potential are superimposed with coloring to indicate (c) $b^2$ and (d) $j^2$ , for a current $\mathbf{j} = \nabla \times \mathbf{b}$ . The 2D MHD field is a more physically realistic model, reproducing aspects of the flux tube viewpoint, but with the current concentrated in narrow current sheets. The present work examines the level of association between $b^2$ or $j^2$ and sharp changes in field line connection over a distance of 1 AU, which relates to dropouts (sharp density changes) in solar energetic particles as observed near Earth.	59
5.2 Omnidirectional power spectra of 2D random-phase and 2D MHD turbulent magnetic field models, normalized to the same total energy. After the fixed-time 2D MHD procedure, the high-wavenumber portion of the spectrum has been eroded by the turbulent cascade, which affects the overall normalization.	60
5.3 Comparison of quantities pertaining to two models of 2D magnetic turbulence, 2D random-phase (left panels) and 2D MHD (right panels): (a)-(b) Magnetic potential, $a$ . (c)-(d) Magnetic energy, $b^2$ . (e)-(f) $j_{FD}^2$ , where the current $\mathbf{j}_{2D}$ is determined from finite differencing of $\mathbf{b}$ . In the more physical 2D MHD model, $a$ is smoother, $b$ varies more gradually, and $j$ is concentrated in narrow current sheets.	61

## LIST OF FIGURES (cont.)

Figures	Page
<p>5.4 For a mean magnetic field along <math>\hat{\mathbf{z}}</math> and two-component magnetic turbulence, we trace 10,000 magnetic field lines from initial locations within a circle of radius 0.1 AU. These scatter plots show <math>(x, y)</math> locations of field lines after a distance <math>z</math> of 1.0 AU, superimposed with indications of (a) contours of constant potential <math>a(x, y)</math> at equal intervals <math>\Delta a</math> (b) local trapping boundaries (LTBs; contours) (green), (c) <math>b^2</math> (red), and (d) <math>j^2</math> (blue). Sharp gradients in magnetic connection to the source, i.e., dropout features, are seen to be associated frequently with LTBs, sometimes with large <math>b^2</math>, and infrequently with current sheets.</p>	67
<p>5.5 Scatter plots of magnetic field lines and particle trajectories in 2D MHD+slab turbulence at <math>z = 1.0</math> AU.</p>	68
<p>6.1 Scatter plots of magnetic field trajectories and proton trajectories for various energies at 1 AU. The upper left panel is a scatter plot of magnetic field lines. The upper right panel is for 1 MeV protons. The bottom left panel is for 10 MeV protons and the bottom right panel is for 1 GeV protons.</p>	71
<p>6.2 Surface plot of a positive 2D Gaussian potential function.</p>	72
<p>6.3 Field line trapping in a positive 2D Gaussian magnetic island + slab turbulence. [Image Credit: Chuychai et al. 2007]</p>	73
<p>6.4 Scatter plots of 10 GeV proton trajectories at various distances in a positive 2D Gaussian island. The upper left panel shows initial positions of particles at <math>r = 0.1</math> AU. The next panel is for particles at <math>r = 0.5</math> AU. The bottom left panel is for particles at <math>r = 1.0</math> AU and the last panel is for particles at <math>r = 2.0</math> AU.</p>	74
<p>6.5 Surface plot of a negative 2D Gaussian potential function.</p>	75
<p>6.6 Scatter plots of 10 GeV proton trajectories at various distances in a negative 2D Gaussian island. The upper left panel shows initial positions of particles at <math>r = 0.1</math> AU. The next panel is for particles at <math>r = 0.5</math> AU. The bottom left panel is for particles at <math>r = 1.0</math> AU and the last panel is for particles at <math>r = 2.0</math> AU.</p>	76
<p>6.7 Definitions of <math>\mathbf{K}</math> and <math>\beta</math> for a conical flux rope.</p>	77

## LIST OF FIGURES (cont.)

Figures	Page
6.8 Scatter plots of 10 GeV proton trajectories at various distances. The upper left panel is a contour plot of the vector potential. Darker color indicates higher potential values and lighter color indicates lower potential values. The next panel is for particles at $r = 0.25$ AU. The bottom left panel is for particles at 0.5 AU. The last panel is for particles at 1.0 AU.	80
6.9 Scatter plots of magnetic field trajectories and proton trajectories for various energies at 2 AU. The upper left panel is a scatter plot of magnetic field lines. The upper right panel is for 10 MeV protons. The bottom left panel is for 3 GeV protons and the bottom right panel is for 10 GeV protons.	81



# CHAPTER I

## INTRODUCTION

### 1.1 Solar Events

When viewing the solar atmosphere in visible light, one can see dark regions called sunspots. A sunspot is a dark patch resulting from a localized fall in temperature to about 4000 K. Most spots have a central dark umbra surrounded by a lighter penumbra. Sunspots tend to occur in clusters and last about two weeks. Their occurrence is much more frequent every 11 years (the solar cycle). They also have more intense magnetic fields than their surroundings. Magnetic loops are magnetic flux tubes rising through the photosphere. Both ends of the tubes continually move due to the motion of plasma in the solar atmosphere. When they are moving, they can build up magnetic stress. When magnetic loops have more stress, they tend to release energy in sudden events. These processes are called solar activity or solar storms. Solar activity can be classified as solar flares and coronal mass ejections. A solar flare is a burst at the surface of the Sun, defined in terms of heating of plasma as observed by enhanced  $H\alpha$  line emission or soft X-rays. There are two types of solar flares:

- **Impulsive flare:** A small burst at the solar surface, or a so-called confined flare. When an impulsive event occurs, we can observe type III and type V radio bursts. The observed soft X-ray duration is less than one hour. The duration of the  $H\alpha$  event is a few minutes.

- **Gradual flare:** A so-called eruptive flare, observed by radio bursts of type II and IV. The soft X-ray duration is greater than or in the order of one hour. The  $H\alpha$  event can last for hours. These flares are usually associated with a coronal mass ejection.

Another major type of solar activity is a coronal mass ejection (CME). A

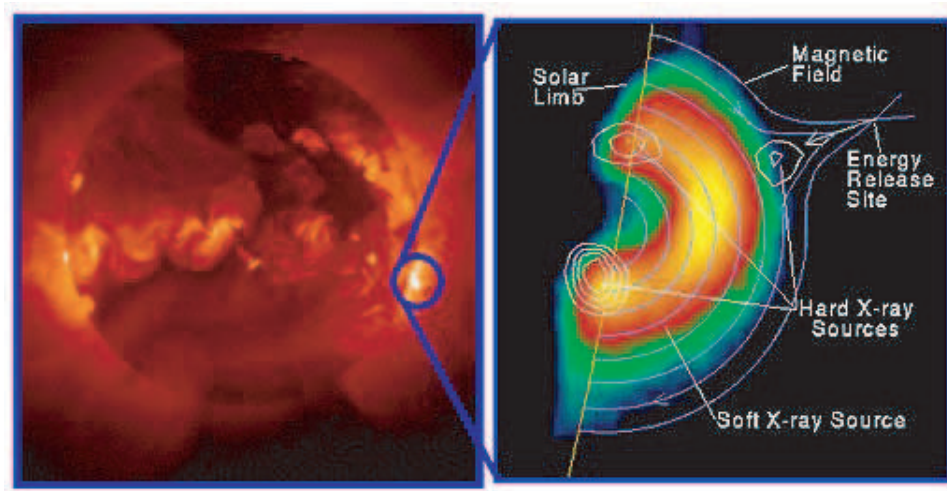


Figure 1.1: Observation of an impulsive flare event at the Sun. [Image credit: Yohkoh Soft X-Ray Telescope]

coronal mass ejection is an ejection of a giant blob of plasma from the corona with high speed (up to about 3,000 km/s). Gradual flares and the associated coronal mass ejection-driven shocks are the major sources of acceleration of energetic particles. Examples of solar events are shown in Figures 1.1 and 1.2.

## 1.2 Solar Wind

The solar wind is a continuous outward flow of plasma, made up of charged particles, mostly protons and electrons, from the corona into interplanetary space, in all directions. The plasma is controlled by the Sun's magnetic field and is able to escape from the Sun's gravitational field because of its high thermal energy. The solar wind is fully ionized plasma, and its typical temperature is 10,000 K (Meyer-Vernet 2007). The composition of solar wind is mainly hydrogen (96%) and most of the remainder is helium. The speed of the solar wind varies with solar latitude and also during the solar cycle. The typical speed of the solar wind toward Earth is approximately 400 km/s (we call this slow wind). Fast wind has a speed of 700-800 km/s. During solar minimum, slow wind is mainly observed between 20° N and 20° S, and fast wind is mainly at higher latitudes, as shown in Figure 1.3.

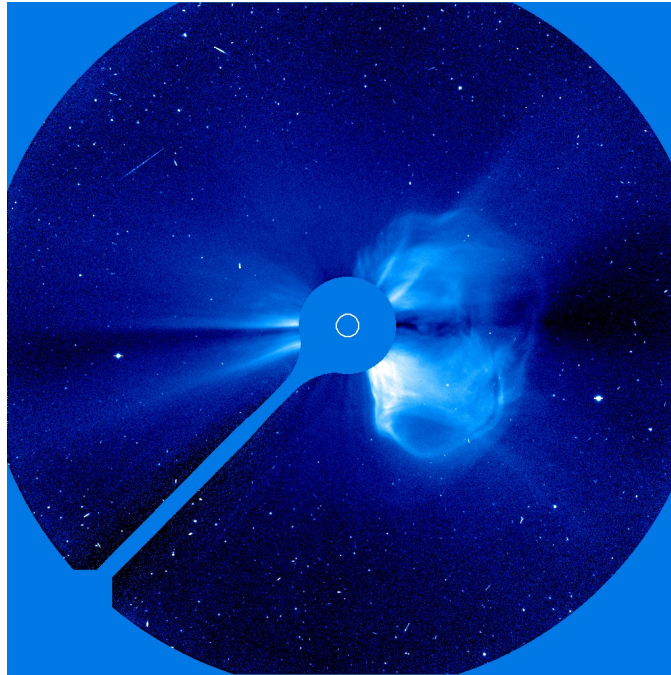


Figure 1.2: A large coronal mass ejection (CME) on 20 April 1998. A disk blocks the Sun so that the LASCO instrument can observe the structures of the CME and the corona in visible light. The white circle represents the size and position of the Sun. [Image credit: SOHO observatory (NASA/ESA)]

During solar maximum, the solar wind is different, because magnetic fields at the photosphere (solar surface) are much more complex, leading to complex structures of magnetic fields at the surface of the Sun, which inhibit fast solar wind.

### 1.3 Interplanetary Magnetic Field

The solar wind also drags the magnetic field from the Sun into interplanetary space to become the interplanetary magnetic field (IMF). The magnetic field on the Sun can be dragged outward with the solar wind because of two reasons (Cravens 1997; Meyer-Vernet 2007): 1) For the solar wind, the ram pressure, defined as  $\rho v^2$  where  $\rho$  is density of the solar wind, is much greater than the magnetic pressure. 2) There is a high magnetic Reynolds number, defined as the ratio between the convective term and the diffusive term in the magnetic transport equation of MHD (see Section 2.2), i.e.,  $(UB/L)/(D_B D/L^2) = UL/D_B$ , where  $D_B = 1/\sigma\mu_0$  is the magnetic diffusion coefficient.

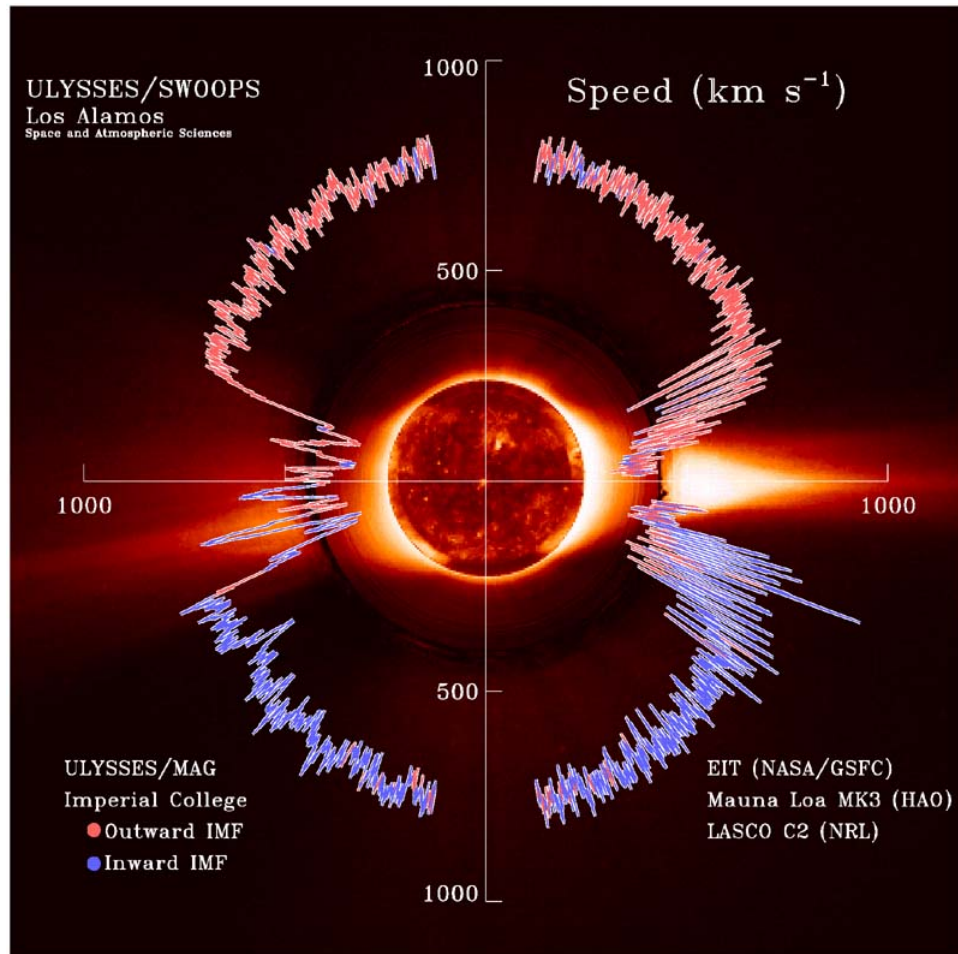


Figure 1.3: Observed solar wind from SOHO during solar minimum. [Image credit: SOHO]

In the ionized solar wind, the electrical conductivity  $\sigma$  is very high, so magnetic diffusion can be neglected. Therefore, the magnetic field will be convected by the solar wind. During solar minimum, the magnetic field in the northern hemisphere on average has one polarity and the southern hemisphere has the opposite polarity. Figure 1.4 shows a schematic of the magnetic field during solar minimum.

Since the solar wind is highly turbulent, the magnetic field is turbulent too. This makes magnetic field lines look irregular as shown in Figure 1.6. The spiral shape is due to rotation of the Sun.

There is observational evidence of interplanetary fluctuations near Earth that

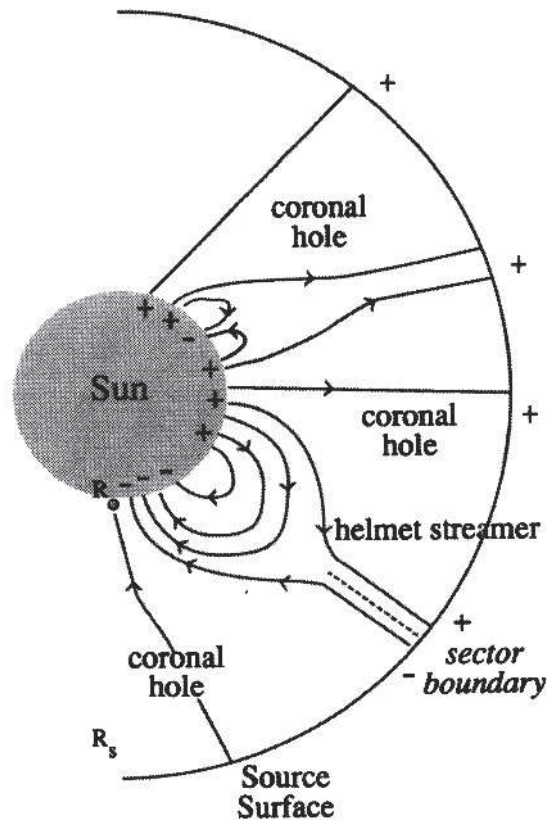


Figure 1.4: Structures of magnetic fields of the sun during solar minimum. [Image credit: Cravens 1997]

include wavevectors parallel and perpendicular to the mean magnetic field. These lead to a turbulent magnetic field model that we use in this work, the so-called two-component model. The details of the magnetic field model will be discussed more in Chapter 2.

In the region between the northern magnetic polarity and southern magnetic polarity of the Sun, a neutral current sheet is formed due to the change in magnetic field. This structure is also dragged out by the solar wind to become the heliospheric current sheet (the “ballerina skirt”) as shown in Figure 1.5

A number of studies (Matthaeus *et al.* 1990; Bieber *et al.* 1996) have observed that interplanetary magnetic fluctuations near Earth necessarily include wavevectors  $\mathbf{k}$  that are parallel (“slab” fluctuations) and perpendicular (“2D” fluctuations) to the large-scale field, with less power at oblique wavevectors. It has been proposed that

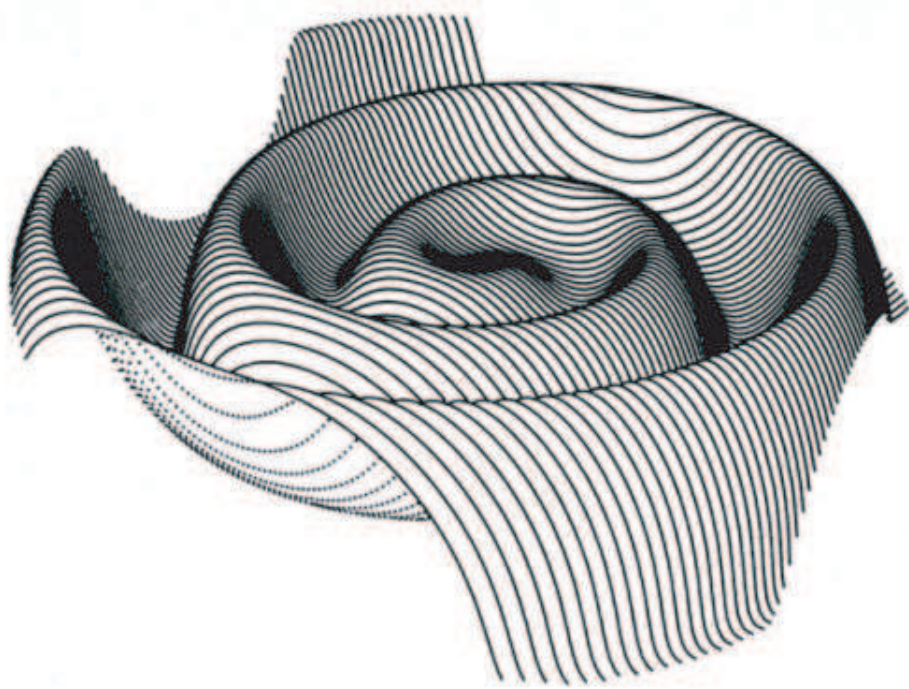


Figure 1.5: Warped current sheets. [Image credit: J. R. Jokipii, University of Arizona]

the interaction of counter-propagating fluctuations with a component of  $\mathbf{k}$  parallel to the mean field can naturally produce 2D fluctuations at much higher perpendicular  $\mathbf{k}$ , leading to a component that can become approximately 2D. MHD simulations have provided substantial evidence for this (Shebalin *et al.* 1983; Oughton *et al.* 1994), and various models (Montgomery 1982; Higdon 1984; Goldreich & Sridhar 1995) build in this anisotropy as an assumption.

#### 1.4 Solar Energetic Particles and Dropouts

We refer to the particles that are accelerated by solar storms as solar energetic particles (SEPs). While the energy is released by magnetic reconnection, the processes of SEP acceleration are stochastic acceleration and shock acceleration. SEPs can come to Earth by following the interplanetary magnetic field that is dragged outward from the Sun by the solar wind.

Recently there were observations of the distribution of SEPs from impulsive

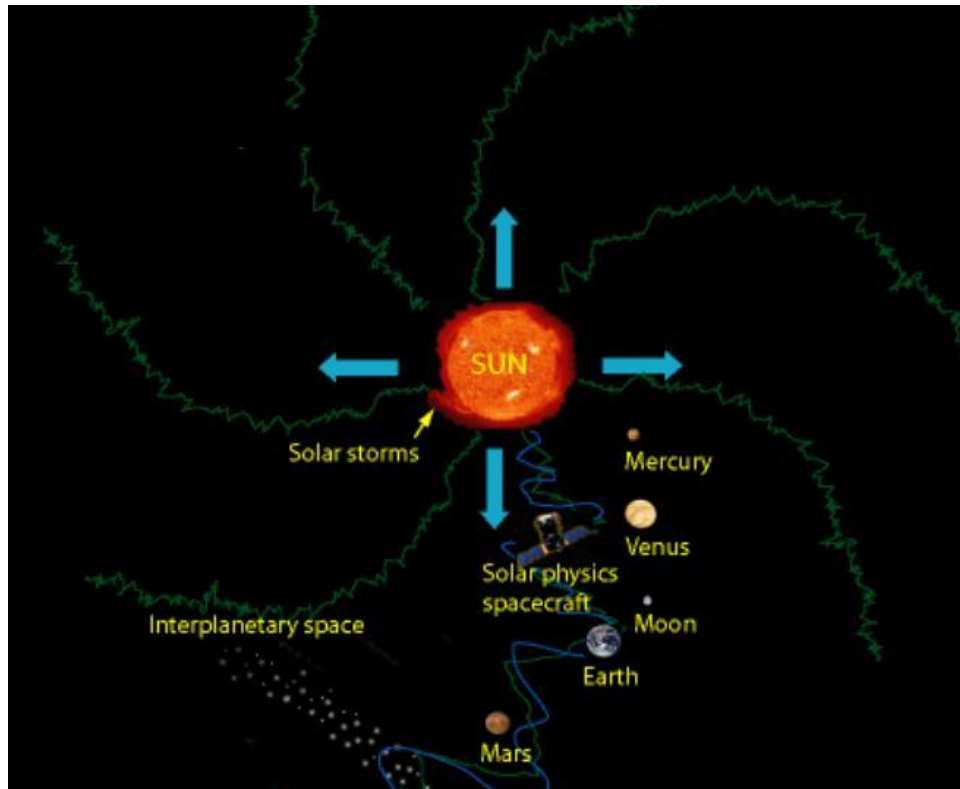


Figure 1.6: Illustration of plasma and magnetic fields in the inner solar system. Blue arrows indicate solar wind flow. Green lines are interplanetary magnetic field lines and the blue line indicates particle motion.

solar flare events by the *Advanced Composition Explorer (ACE)* (Mazur *et al.* 2000). Figure 1.7 shows the energy of all ions observed by the ULEIS instrument over the nuclear charge range of 1 to 26 (i.e., for elements from H to Fe) versus arrival time at 1 AU for impulsive events on January 9-10, 1999. Dropouts refer to discontinuous data where the intensity of SEPs repeatedly disappears and reappears. This observation indicates that SEPs are confined to filaments in space (Giacalone *et al.* 2000).

Given that large-scale diffusion of SEPs is quite rapid (McKibben *et al.* 2001; McKibben 2005), specific mechanisms are needed to explain sharp particle gradients over intermediate distance scales. Proposed mechanisms include temporary topological trap-

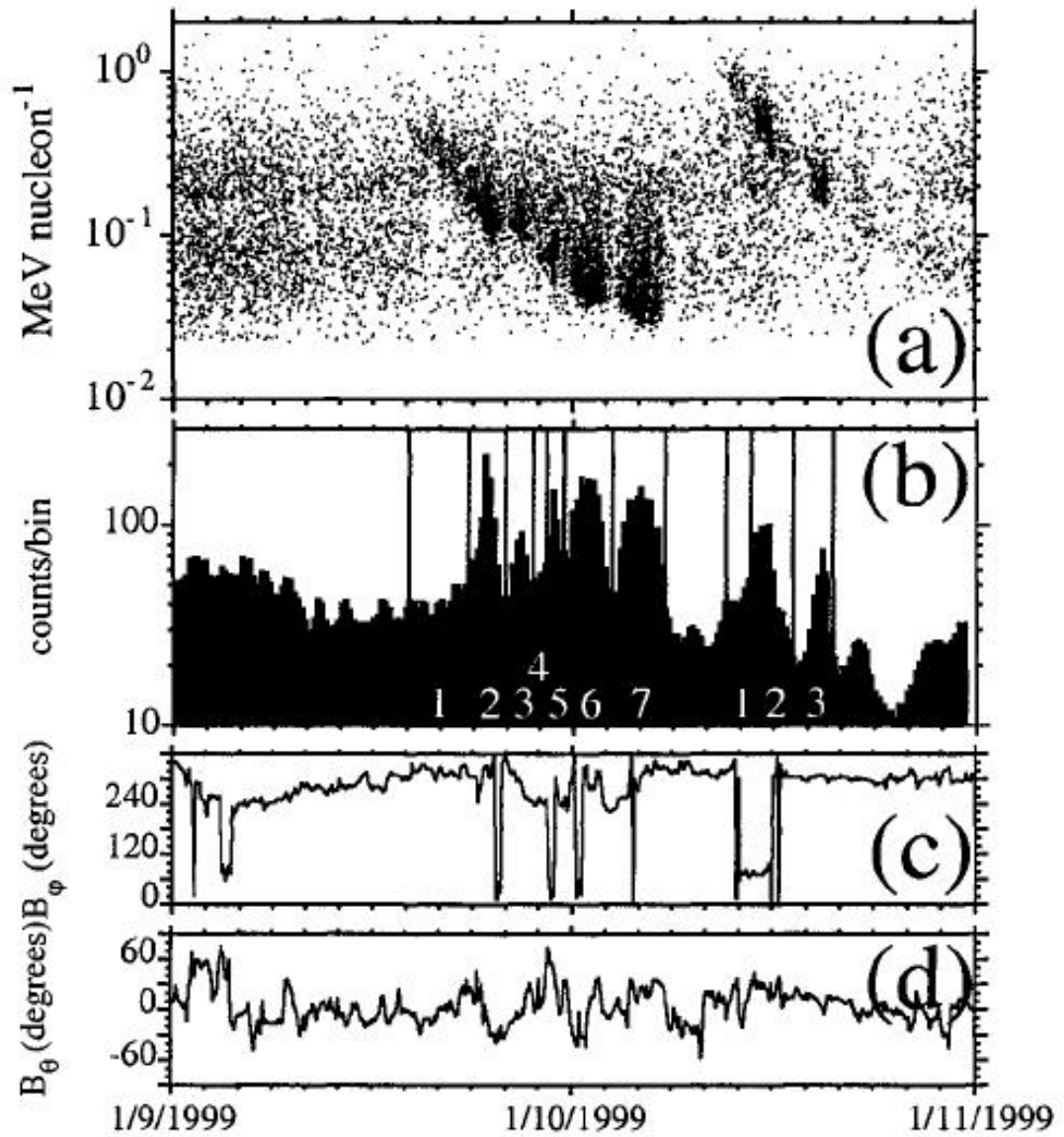


Figure 1.7: Energetic particle velocity dispersion and interplanetary magnetic field direction during 1999 January 9-10. (a) H to Fe ion energy versus time; (b) histogram of ion count rate; (c) magnetic field azimuth direction in geocentric-solar-ecliptic (GSE) coordinates; (d) GSE magnetic field altitude direction. [Image credit: Mazur et al. 2000]



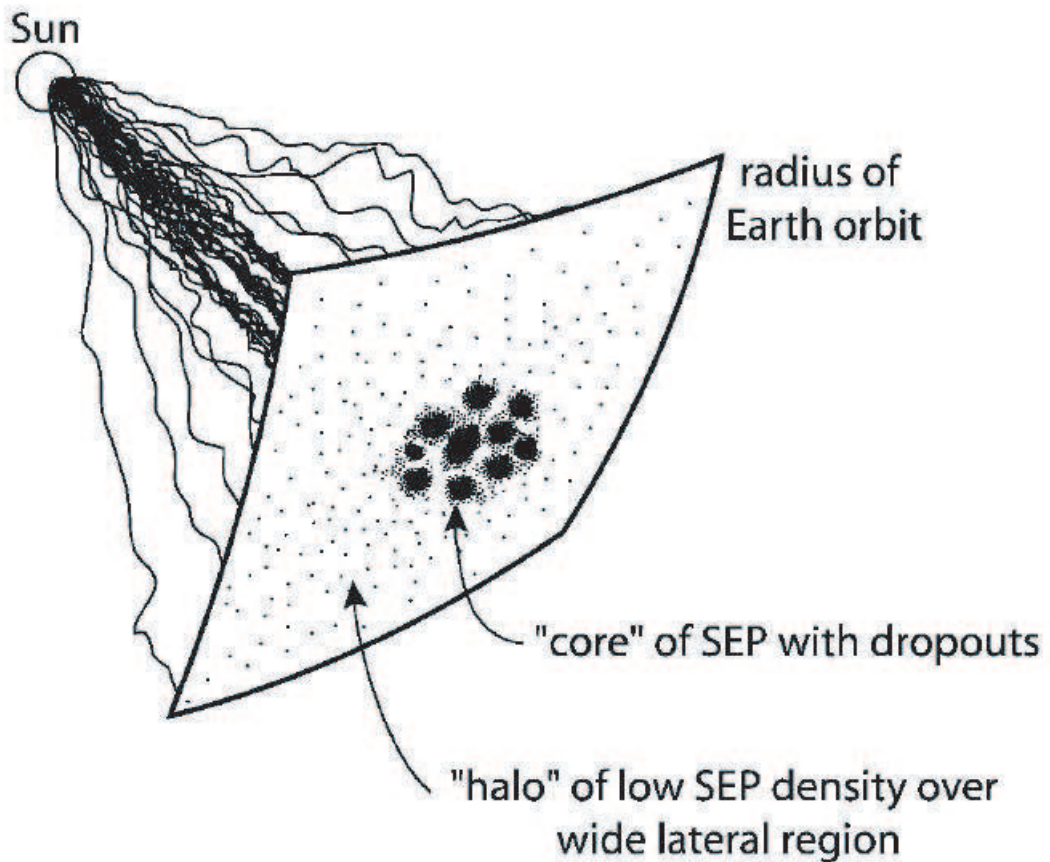


Figure 1.8: Illustration of interplanetary magnetic field lines populated with SEPs from a localized source region near the Sun. The field lines are filamented according to the small scale topology of solar wind turbulence. [Image credit: Ruffolo *et al.* 2003]

ping of field lines in “islands” of the 2D turbulence (Ruffolo *et al.* 2003) and suppressed diffusive escape where the 2D field is strong or irregular (Chuychai *et al.* 2005, 2007; Tooprakai *et al.* 2007). Over a long distance scale, magnetic field lines can escape their temporary topological traps and undergo rapid lateral diffusion. Figure 1.8 illustrates the concept of topological trapping.

### 1.5 Local Trapping Boundaries and Current Sheets

Naturally the question arises as to the boundary of the “islands” of field line trapping. Note that the turbulence is homogeneous, and there is no “input” structure; the “islands” are regions around local maxima and minima of a random 2D potential

function. In simulation results for random-phase 2D+slab turbulence, Chuychai *et al.* (2007) identified LTBs, defined as contours of constant 2D potential where  $|b^{2D}|_{av}^2$  is maximized with respect to neighboring contours, as frequently defining sharp changes in magnetic connection where dropout features would be expected, which in some cases can be interpreted as boundaries of trapping regions. The LTBs reflect the concept of temporary trapping along closed 2D orbits, with eventual escape due to slab fluctuations, as well as the suppression of slab diffusive escape where the 2D field is strong. Chuychai *et al.* (2007) showed that in random-phase simulations of turbulent 2D+slab magnetic fields, LTBs were well associated with dropout features.

On the other hand, random-phase models of turbulence do not contain current sheets, i.e., strong, thin current structures, which clearly are present in the interplanetary medium. Current sheets, or discontinuous or sharp magnetic features in general, require that a large number of Fourier modes have coordinated phases to create a jump that is spatially localized. The correlations required to establish these structures are generated rapidly by nonlinear turbulence processes (Servidio *et al.* 2008) that are associated with non-Gaussian statistics and intermittency (Wan *et al.* 2009). Random-phase models are also unable to explain the observed distributions of strong jumps in various properties of the solar wind as presented by Borovsky (2008). Chollet and Giacalone (2008) considered the possibility that current sheets, i.e., sharp changes in the magnetic field, might indicate the locations of dropout features.

## 1.6 Motivation and Objectives of This Study

In the present work, we aim to rectify these shortcomings in the turbulence models by replacing the 2D random-phase field by the output of a 2D MHD simulation. While computationally time-consuming, a 2D MHD model incorporates the microphysics of the plasma to produce current sheets and structures resembling flux tubes. In this way, the concepts of a flux tube view naturally appear in a more physical model of the turbulent magnetic field. A 2D MHD + slab field with filamentary magnetic connection

has previously been used in an explanation of “moss” emission in the solar transition region (Kittinaradorn *et al.* 2009). Here, we want to use this more realistic model to identify whether LTBs or current sheets provide better indicators for dropouts.

Another concern is that particle transport along the turbulent interplanetary magnetic field should include the effects of adiabatic focusing (Roelof 1969; Ruffolo & Khumlumlert 1995). This process conserves the magnetic moment, i.e.,  $p_{\perp}^2/2mqB \propto 1 - \mu^2/B = \sin^2 \theta/B$ , where  $\theta$  is the pitch angle of the particle, which is defined by the angle between the momentum of the particle and the magnetic field direction. As a particle moves to higher magnetic field strength, the pitch angle increases to conserve the magnetic moment. In the same time, there is also a conservation of kinetic energy of the particle, which implies that  $v^2 = v_{\perp}^2 + v_{\parallel}^2$ . This has a consequence: as the pitch angle increases,  $v_{\parallel}$  will decrease. If it reaches zero, then the particle will turn around and move back. This is called magnetic mirroring. Therefore, in the present work we perform particle trajectory simulations in spherical geometry, where focusing is naturally included. We aim to explore the results of particle trajectory simulations in 2D random-phase fields and 2D MHD+slab fields.

The objectives of this research are

1. To investigate dropout patterns of particle trajectories in a Cartesian geometry.
2. To identify local trapping boundaries.
3. To investigate the relationship between local trapping boundaries and current sheets and their roles in defining dropout patterns.
4. To study the behavior of charged particle motion in a spherical geometry, comparing 2D MHD and 2D random-phase fields.

### **Expected benefits**

The work will give us a better understanding of dropout patterns and other particle transport processes in turbulent magnetic fields, which have applications in

heliospheric physics, space physics, and astrophysics.

## 1.7 Outline of the Thesis

This thesis is organized as follows: Chapter 1 introduces solar storms, solar energetic particles, dropouts, local trapping boundaries, and current sheets. The motivation, objectives of study, and expected benefits are also given in this chapter. Chapter 2 provides the physics of turbulence, magnetohydrodynamics and a literature review. Chapter 3 describes some existing numerical methods. This chapter introduces turbulent magnetic field modeling in both Cartesian geometry and spherical geometry, including how to generate the turbulent magnetic field and also how to find magnetic field line trajectories and particle trajectories. Chapter 4 presents some new numerical techniques. Chapter 5 gives the general properties of a 2D MHD field, in comparison with the random-phase field, and numerical results of simulations in Cartesian geometry including the role of LTBs for dropout features. Chapter 6 gives the results from numerical simulations in spherical geometry, including the collimation of beams of very high energy particles. Chapter 7 (the final chapter) provides the conclusions.

## CHAPTER II

# THEORETICAL BACKGROUND AND LITERATURE REVIEW

We briefly described the solar wind and interplanetary magnetic field in Chapter 1. In this chapter we will discuss their features in more detail. Before going into details of structures observed in the inner solar system, some basic physics about the structures is discussed, including turbulence and magnetohydrodynamics (MHD).

### 2.1 Turbulence

Turbulence is a type of flow that is complex. Turbulence is subset of randomness. To determine whether a flow is turbulent, we have to look at the characteristics of the flow. A flow considered turbulent must have following characteristics (Tennekes & Lumley 1972):

- **Irregularity.** Turbulence is generated by random perturbations and instabilities. Turbulence is subset of randomness which means that turbulence is random but random motion is not necessarily turbulent. Being random, a deterministic solution for turbulence is not possible. Statistical properties are used instead.
- **Diffusivity.** Diffusivity is an important characteristic of turbulence, because the mixing and transfer rates of heat, momentum and mass increase by this process (Tennekes & Lumley 1972).
- **3D vorticity fluctuations.** Turbulent motion must have vortex stretching, which results from the random motion of vorticity structures.
- **High Reynolds numbers.** The Reynolds number is the ratio between the inertial term and the viscous term in the momentum transfer equation of hydrodynamics

(HD) or MHD. The Reynolds number is defined by  $Re = UL/\nu$ , where  $U$  is a velocity scale of the fluid,  $L$  is a length scale and  $\nu$  is the molecular viscosity. At high Reynolds number, the flow will become unstable and then the instability causes turbulence.

- **Energy input and energy dissipation.** Turbulent flow is always dissipative. Dissipation is comparable with energy transfer in the dissipation range of length scales. Because turbulence is dissipative, then in the absence of energy input, turbulence will decay.
- **Continuum.** Turbulence is a fluid flow phenomenon. Turbulence only occurs over scale lengths in which particles or molecules flow as a fluid.

We cannot describe turbulent flow in detail with deterministic equations, so we need statistical descriptions instead. A statistical quantity that is very useful is variance, because it can be interpreted as energy. The mean fluctuation is not so useful because typically it equals zero. An important statistical quantity for turbulence is the correlation function, which tells us the correlation of variables between two different points in space or time. For example, the correlation length of the magnetic field is defined by

$$R_{ij}(x, \mathbf{r}) = \langle b_i(\mathbf{x})b_j(\mathbf{x} + \mathbf{r}) \rangle. \quad (2.1)$$

For homogeneous turbulence, we can write

$$R_{ij}(x, \mathbf{r}) = R_{ij}(\mathbf{r}) = \langle b_i(0)b_j(\mathbf{r}) \rangle. \quad (2.2)$$

The Fourier transform of the correlation function is the power spectrum,

$$P_{ij}(\mathbf{k}) = \frac{1}{(\sqrt{2\pi})^3} \int_{-\infty}^{\infty} R_{ij}(\mathbf{r}) \exp(i\mathbf{k} \cdot \mathbf{r}) d^3\mathbf{r}. \quad (2.3)$$

A power spectrum for a single component, for example  $P_{xx}(k)$ , can be interpreted in terms of the square of the magnetic field in Fourier space,  $P_{xx} = |B_x(k)|^2$ , so  $P_{xx}(k)$  represents the energy in  $b_x^2$  per unit  $k$ .

Kolmogorov (1941) was the first to develop a theory in which turbulent flow has a power spectrum with a spectral slope of  $-5/3$ . We call any power spectrum that has this slope over a range of distance scales a Kolmogorov spectrum. Figure 2.1 shows a typical power spectrum of a turbulence flow. Note that low  $k$  corresponds to a large distance scale and high  $k$  corresponds to a small distance scale.

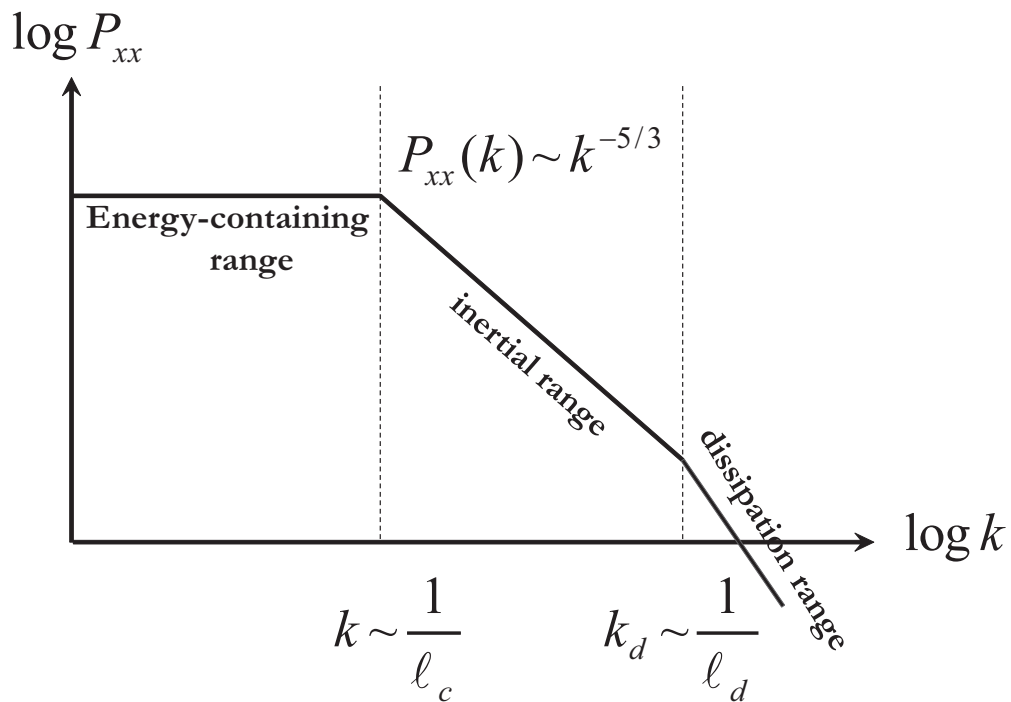


Figure 2.1: The spectrum of turbulence from Kolmogorov theory.

The spectrum has three ranges. The energy-containing range is the range of scales where turbulent energy is input. From here energy is transferred to the inertial range and then the dissipation range. In the inertial range, the inertial term is much greater than the dissipation term, i.e.,  $Re \gg 1$ . The inertial term causes vortex stretching. In a steady state, the energy transfer rate per mass is constant over all length scales. Finally the dissipation range is the range where the dissipative energy loss dominates the inertial energy transfer. The spectrum shown in Figure 2.1 can explain observations of the solar wind and also the magnetic field in space, as we will see later in this chapter.

## 2.2 Magnetohydrodynamics

### 2.2.1 General

Plasma phenomena are typically described in one of two ways: kinetic theory and magnetohydrodynamics (MHD). Kinetic theory will give us more details but the equations can be very complicated and difficult to understand or solve. Many phenomena can be explained well and much more simply using MHD, including various aspects of the solar wind. Here we will give a short review of MHD equations and MHD waves.

The MHD equations are:

**Continuity equation** - conservation of mass, can be used in both HD and MHD:

$$\frac{\partial \rho}{\partial t} + \nabla \cdot (\rho \mathbf{v}) = 0. \quad (2.4)$$

**Momentum equation** - effect of forces:

$$\rho \frac{\partial \mathbf{v}}{\partial t} + \rho(\mathbf{v} \cdot \nabla) \mathbf{v} = -\nabla p + \mathbf{J} \times \mathbf{B} + \rho \mathbf{g}. \quad (2.5)$$

**Magnetic induction equation**

$$\frac{\partial \mathbf{B}}{\partial t} = \nabla \times (\mathbf{v} \times \mathbf{B}) + D_B \nabla^2 \mathbf{B}. \quad (2.6)$$

The relation between current and magnetic field is governed by

$$\mathbf{J} = (\nabla \times \mathbf{B}) / \mu_0. \quad (2.7)$$

This set of equations is not yet complete. In addition, we need a so-called closure relation.

A common closure relation is the polytropic relation:

$$p/p_0 = (\rho/\rho_0)^\gamma, \quad (2.8)$$

where  $\gamma$  is the polytropic index.

Basically, the MHD equations allow us to study 3 types of problems (Goossens 2003):

1. Static equilibrium configurations of plasma.



2. Stability of a system that is perturbed by a small perturbation. This type problem concerns unstable motion of plasma that terminates equilibrium.
3. Some types of waves that can occur in a stable magnetic equilibrium configuration. For this problem, we study stable motions of a plasma until they are damped by dissipation.

Both 2. and 3. can be studied by using linearized MHD equations. Linearized MHD equations have limitations, i.e., we cannot study

- nonlinear evolution
- stability with large amplitude perturbation
- damping or excitation of waves.

The conditions for linearized MHD equations are: the plasma properties do not depend on time, i.e.,  $\partial/\partial t = 0$ , and there is static equilibrium if  $\mathbf{v} = 0$ . Substituting the conditions  $\rho = \rho_0 + \rho_1$ ,  $\mathbf{v} = \mathbf{v}_1$  and  $\mathbf{B} = \mathbf{B}_0 + \mathbf{B}_1$  into the MHD equations, where “0” quantities are constants in time and neglecting higher orders of small “1” quantities, we will get linearized MHD equations (neglecting magnetic diffusion and the gravitational potential):

$$\frac{\partial \rho_1}{\partial t} + \nabla \cdot (\rho_0 \mathbf{v}_1) = 0 \quad (2.9)$$

$$\rho_0 \frac{\partial \mathbf{v}_1}{\partial t} = -\frac{dp}{d\rho} \nabla \rho_1 + \frac{\nabla \times \mathbf{B}_1}{\mu_0} \times \mathbf{B}_0 + \frac{\nabla \times \mathbf{B}_0}{\mu_0} \times \mathbf{B}_1 \quad (2.10)$$

$$\frac{\partial \mathbf{B}_1}{\partial t} = \nabla \times (\mathbf{v}_1 \times \mathbf{B}_0). \quad (2.11)$$

### 2.2.2 Waves

After we get linearized MHD equations, now we introduce  $\mathbf{B}_0 = B_0 \hat{z}$ , let “0” quantities be constant in space, and assume plane wave solutions,

$$\rho_1 = \rho_1 \exp[i(\mathbf{k} \cdot \mathbf{r} - \omega t)] \quad (2.12)$$

$$\mathbf{v}_1 = v_1 \exp[i(\mathbf{k} \cdot \mathbf{r} - \omega t)] \quad (2.13)$$

$$\mathbf{B}_1 = B_1 \exp[i(\mathbf{k} \cdot \mathbf{r} - \omega t)]. \quad (2.14)$$

For a given  $\mathbf{k}$ , there are three possible solutions for  $\rho_1$ ,  $\mathbf{v}_1$  and  $\mathbf{B}_1$ . These solutions give us three kinds of MHD waves, namely, ion-acoustic waves, Alfvén waves, and magnetosonic waves.

• **Ion-acoustic waves (sound waves).** These waves are for  $B = 0$ . Then the linearized MHD equations are

$$\frac{\partial \rho_1}{\partial t} + \rho_0 \nabla \cdot \mathbf{v}_1 = 0, \quad (2.15)$$

$$\rho_0 \frac{\partial \mathbf{v}_1}{\partial t} = -\gamma \frac{p_0}{\rho_0} \nabla \rho_1. \quad (2.16)$$

Taking the derivative with respect to time of equation (2.14) and substituting into equation (2.15), we obtain

$$\frac{\partial^2 \rho_1}{\partial t^2} - V_s^2 \nabla^2 \rho_1 = 0, \quad (2.17)$$

where  $V_s = \sqrt{\gamma p_0 / \rho_0}$  is the speed of sound. Thus we obtain ordinary sound waves.

• **Alfvén waves.** Let us consider parallel-propagating Alfvén waves. Here  $\rho = \rho_0$ , a constant. The linearized MHD equations now include  $\mathbf{B} = \mathbf{B}_0 + \mathbf{B}_1$ , so we obtain

$$\rho_0 \frac{\partial \mathbf{v}_1}{\partial t} = \frac{1}{\mu_0} (\nabla \times \mathbf{B}_1) \times \mathbf{B}_0 \quad (2.18)$$

$$\frac{\partial \mathbf{B}_1}{\partial t} = \nabla \times (\mathbf{v}_1 \times \mathbf{B}_0). \quad (2.19)$$

Substituting the plane wave solutions into equations (2.17) and (2.22), and using  $\partial/\partial t \rightarrow$

$-i\omega, \nabla \rightarrow i\mathbf{k}$ , we get

$$-\omega\mathbf{B}_1 = \mathbf{k} \times (\mathbf{v}_1 \times \mathbf{B}_0) = (\mathbf{B}_0 \cdot \mathbf{k})\mathbf{v}_1 - \mathbf{B}_0(\mathbf{k} \cdot \mathbf{v}_1) \quad (2.20)$$

$$-\mu_0\rho_0\omega\mathbf{v}_1 = (\mathbf{k} \times \mathbf{B}_1) \times \mathbf{B}_0 = (\mathbf{B}_0 \cdot \mathbf{k})\mathbf{B}_1 - (\mathbf{B}_1 \cdot \mathbf{B}_0)\mathbf{k}. \quad (2.21)$$

A parallel-propagating Alfvén wave has  $\mathbf{k}$  parallel to  $B_0$  and  $\mathbf{v}_1$  perpendicular to  $\mathbf{k}$ . Then equations (2.19) and (2.20) become

$$-\omega\mathbf{B}_1 = B_0k\mathbf{v}_1 \quad (2.22)$$

$$-\mu_0\rho_0\omega\mathbf{v}_1 = B_0k\mathbf{B}_1 - (\mathbf{B}_1 \cdot \mathbf{B}_0)\mathbf{k}. \quad (2.23)$$

The second term of equation (2.22) equals zero since  $\mathbf{B}_1$  is parallel to  $\mathbf{v}_1$  and hence perpendicular to  $\mathbf{k}$ . Thus  $\mathbf{B}_1 \cdot \mathbf{B}_0 = 0$ . Equations (2.21) and (2.22) imply the dispersion relation  $\omega^2 = k^2V_A^2$ , where  $V_A = B_0/\sqrt{(\mu_0\rho_0)}$  is the Alfvén speed. A schematic Alfvén wave is shown in Figure 2.2. The magnetic tension force serves as the restoring force. If the Alfvén waves propagate with some angle  $\theta$  to  $\mathbf{B}_0$ , then the dispersion relation will become

$$\omega^2 = k^2V_A^2 \cos^2 \theta. \quad (2.24)$$

This is the so-called shear Alfvén wave.

• **Magnetosonic waves.** This wave mode arises from pressure, combining both ram pressure and magnetic pressure. The dispersion relation of magnetosonic waves is

$$\omega^2 = V_{ms}^2 k^2, \quad (2.25)$$

where  $V_{ms}^2 = V_A^2 + V_s^2$ . The phase velocity is

$$V_{ph}^2 = \frac{1}{2} \left[ (V_s^2 + V_A^2) \pm \sqrt{(V_s^2 + V_A^2)^2 - 4V_s^2V_A^2 \cos^2 \theta} \right] \quad (2.26)$$

The plus sign is for fast magnetosonic waves and the minus sign is for slow magnetosonic waves. A schematic magnetosonic wave is shown in Figure 2.3. The wave shown has  $\theta = 90^\circ$ , and is like an ion-acoustic wave in which  $\mathbf{B} \neq 0$ .

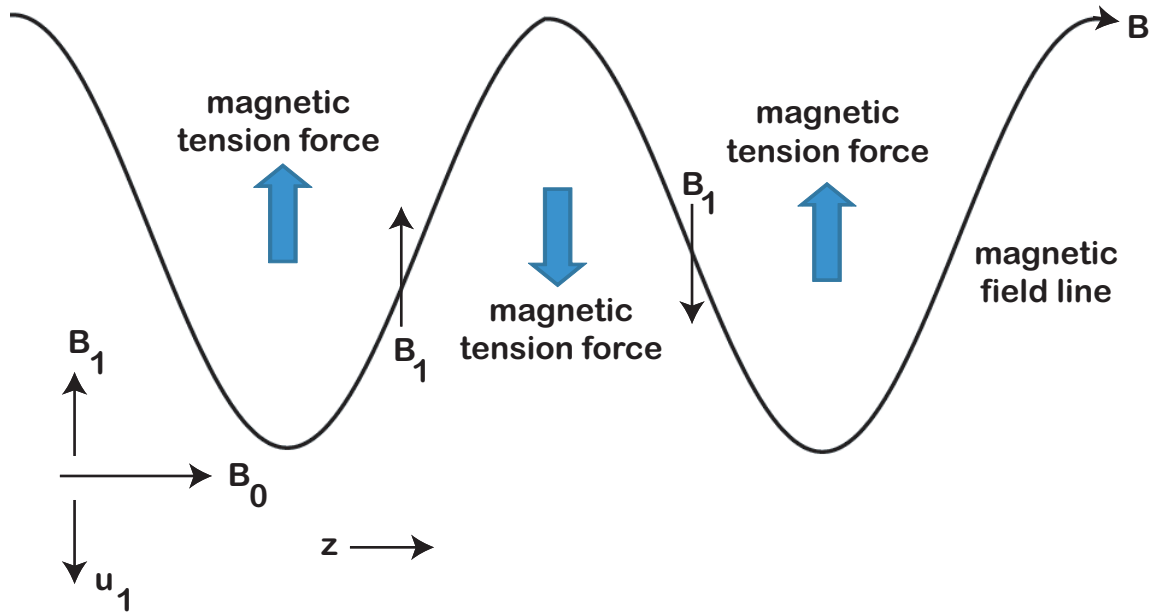


Figure 2.2: Schematic Alfvén wave.

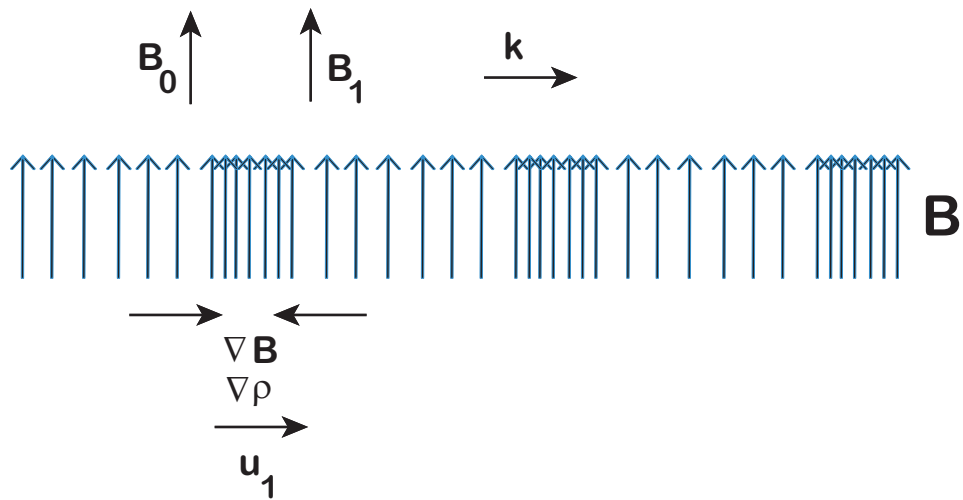


Figure 2.3: Schematic magnetosonic wave.

In sum, we conclude that for any  $\mathbf{k}$ , linearized MHD equations will have three solutions, giving us Alfvén waves (sometimes when  $\theta \neq 0^\circ$  called shear Alfvén waves), fast magnetosonic waves, and slow magnetosonic waves. Ion-acoustic waves are magnetosonic waves that have  $\mathbf{B} = 0$ .

### 2.2.3 Magnetic Reconnection

#### What is magnetic reconnection?

Recall the induction equation 2.6, which tells us that the magnetic field changes due to “advection” and “diffusion”. In a turbulent fluid such as the solar wind, typically the magnetic Reynolds number is high and we can neglect the diffusion term. Nevertheless, there are some spatial regions where the diffusion term is high. Such a region is where plasma elements with magnetic fields in opposite directions are coming toward each other, and the field lines reconnect in a new configuration. Such a region is called a “neutral sheet”, and the process is called “magnetic reconnection” (Priest 1994). A schematic of field lines reconnecting is shown in Figure 2.4.

#### Consequences of magnetic reconnection

1. Magnetic fields change their topology. This will affect particle trajectories because they are moving along field lines.
2. Magnetic energy is converted to kinetic energy and heat.
3. Large currents will occur, as well as electric fields, and sometimes there are slow shocks, which can accelerate particles.

#### Formation of a current sheet: X-type collapse

Suppose we have a magnetic field as follows:

$$B_x = y, \quad B_y = x. \quad (2.27)$$

We will have field lines along  $x^2 - y^2 = \text{constant}$ . In this case, magnetic fields are in pressure balance between the magnetic pressure force (acting toward  $y = 0$ ) and magnetic tension force (acting outward) (Priest 1994). The tension force acts so that magnetic field lines are like rubber bands that resist stretching. If the field is distorted such that the field lines along  $x$  have more curvature, in this case we expect an inward force along the  $y$  axis because the magnetic pressure force is larger than the magnetic tension force.

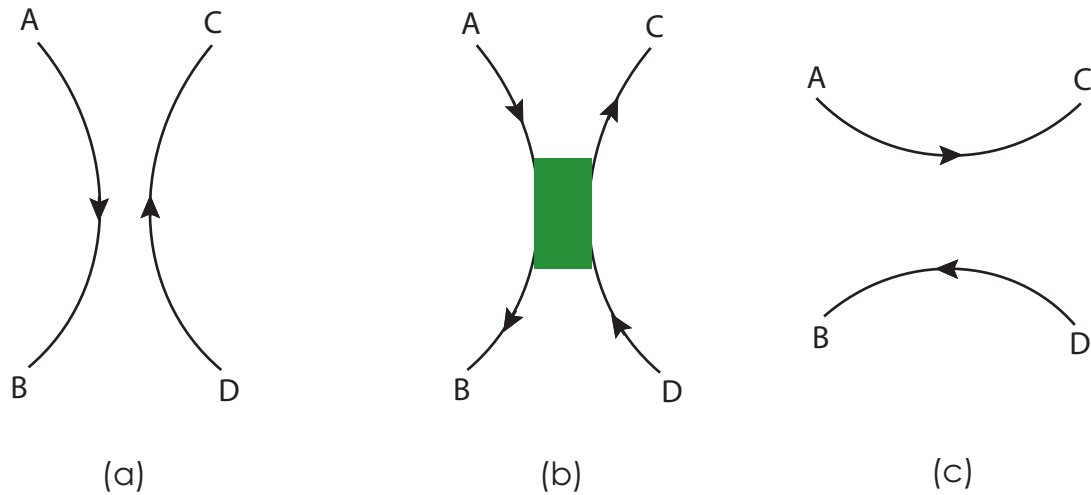


Figure 2.4: (a) Field lines with opposite directions moving toward each other. (b) Neutral region (green shading), where the magnetic diffusion is high and magnetic field lines are reconnecting. (c) New topology of the magnetic field lines.

We expect an outward force along the  $x$  axis because the tension force is higher due to more curvature of magnetic field lines (shown in Figure 2.5a). When this happens, at the X-point there will be a current  $\mathbf{J}$  flowing along the  $z$  axis. Then there will be 2 X-points to the left and right of  $\mathbf{J}$  as shown in Figure 2.5b. Then the 2 X-points will have current flowing along the  $z$  axis again. This process continues until there is a current sheet between the opposite inward flow (Figure 2.5c). Figure 2.6 shows a simple model of magnetic reconnection and a current sheet called the Sweet-Parker (Sweet 1958; Parker 1963a) model. Notice that  $a \gg b$ . Another model is called the Petscheck model, in which the significant difference is the width of  $a \sim b$ . For the Petscheck (Petschek 1964) model, the rate of magnetic reconnection is faster than in a pure Sweet-Parker model, and there are slow shock waves at the boundary layers between inflow and outflow.

### 2.3 Magnetohydrodynamic Turbulence in the Solar Wind

Observations from spacecraft show that the solar wind has both wavelike and turbulence-like properties. Alfvénic fluctuations are observed from magnetic field and flow velocity fluctuations. Evidence for turbulence comes from the power law spectra of

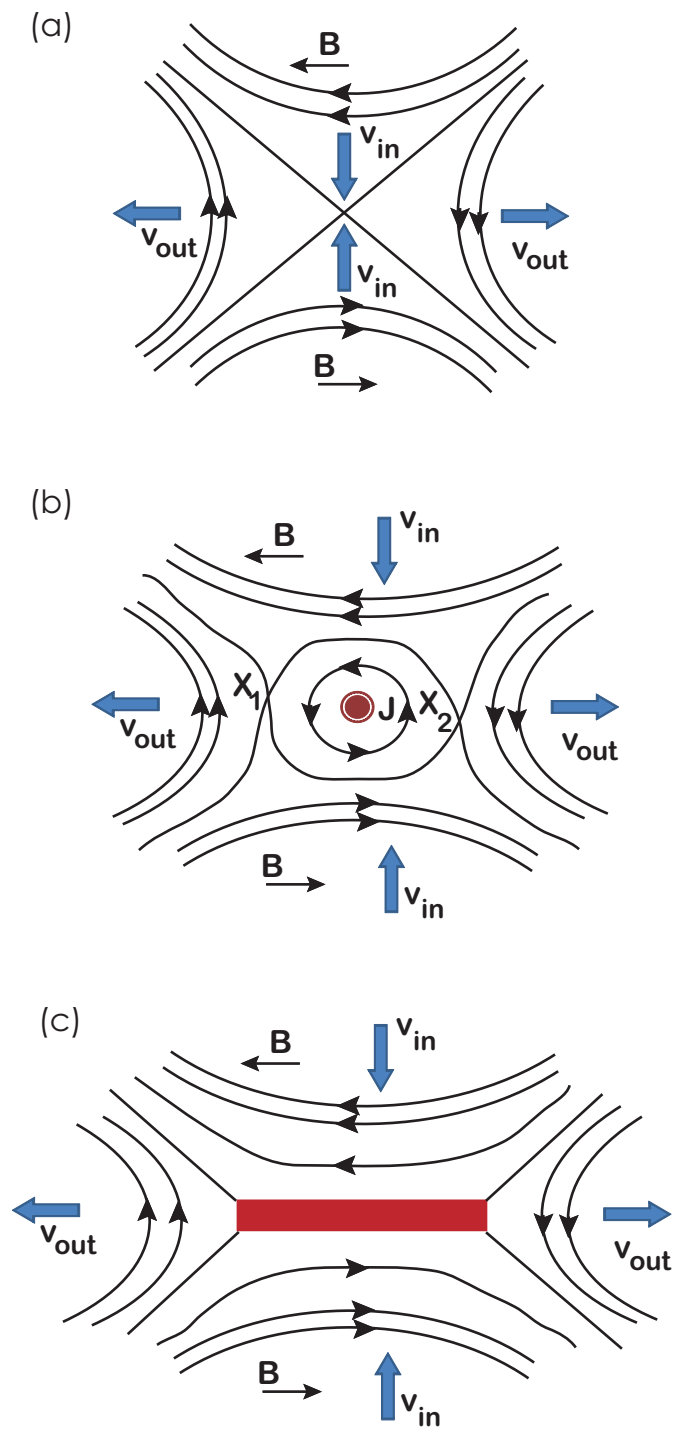


Figure 2.5: (a) Plasma regions with opposed magnetic fields flow into each other. (b) There are 2 X-points,  $X_1$  and  $X_2$ . (c) A neutral current sheet occurs between the incoming flows.

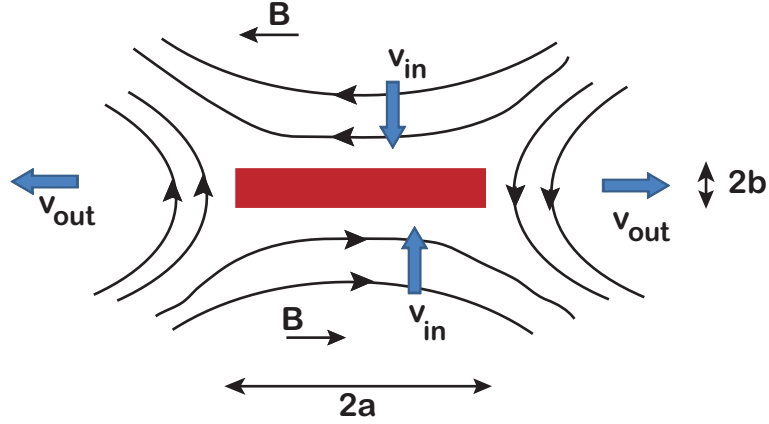


Figure 2.6: Schematic of Sweet-Parker magnetic reconnection.

velocity and magnetic field fluctuations, from which we infer non-linear evolution and an energy cascade. An example of a power spectrum of observed magnetic field fluctuations is shown in Figure 2.7. We can infer  $k$  from the horizontal axis of the graph by the relation  $f = \omega/2\pi = v_{sw}k/2\pi$ , where  $v_{sw}$  is the solar wind speed. To use this relation, we assume the “frozen-in” approximation. Note that in the inertial range, the slope of this log – log graph is nearly  $-5/3$ , which is characteristic of a Kolmogorov spectrum.

It is believed that MHD can explain the turbulent cascade process of the solar wind. Matthaeus *et al.* (1990) constructed a contour plot of the two-dimensional correlation function of magnetic field fluctuations from 16 months of *ISEE 3* magnetometer data as shown in Figure 2.8. This plot suggests that in addition to slab fluctuations (population parallel to the mean) there should be another population of the solar wind fluctuations that has wave vectors transverse to both the mean magnetic field and the fluctuations about the mean. This is the motivation for the so-called two-component magnetic field model.

For the two-component magnetic field model, or more precisely, the 2D+slab model, we assume  $\mathbf{B} = \mathbf{B}_0 + \mathbf{b}$ , where  $\mathbf{b} \perp \mathbf{B}_0$ . For a Cartesian geometry, typically we let  $\hat{z}$  be the mean field direction. The slab field, by definition, depends on the  $z$  coordinate, while the 2D field depends on  $x$  and  $y$  coordinates. A schematic of populations of



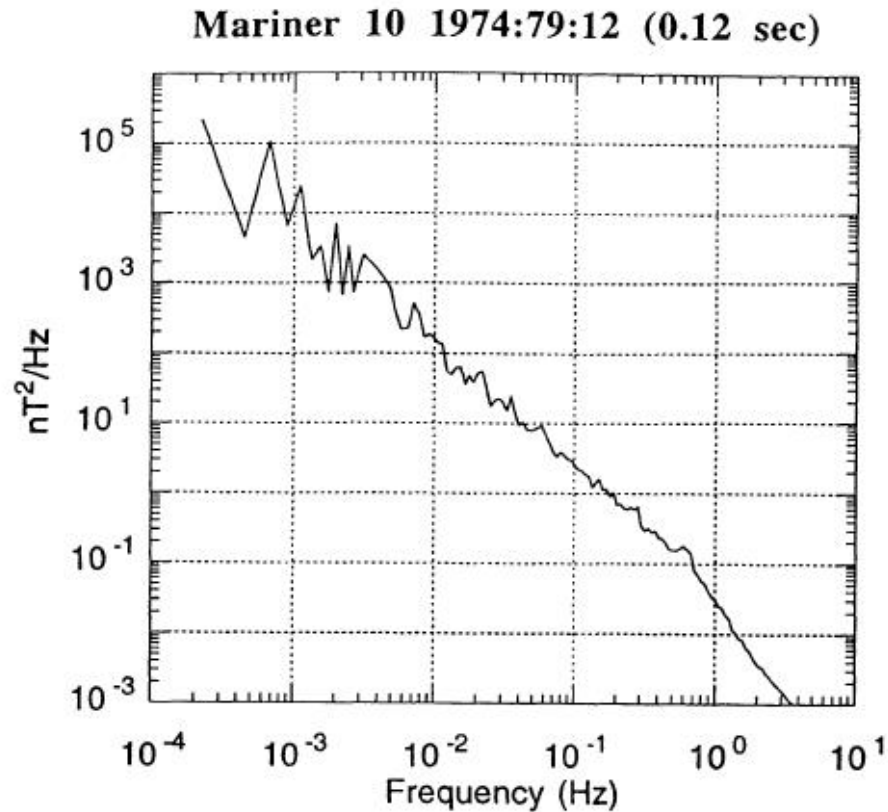


Figure 2.7: Power spectrum of magnetic field fluctuations from a 74-minute interval of 0.12-second-averaged *Mariner 10* magnetometer data. [Image credit: Goldstein et al. 1995]

fluctuations in the solar wind is shown in Figure 2.9. More details about numerical simulation will be given in Chapter 3.

## 2.4 Literature Review

The “dropouts” in solar energetic particles from impulsive solar flares (Mazur *et al.* 2000; Gosling *et al.* 2004), in which the measured particle flux undergoes sudden, large changes, frequently seeming to disappear and reappear, suggest a filamentary distribution of magnetic connection to the particle source (Giacalone *et al.* 2000; Ruffolo *et al.* 2003; Zimbardo *et al.* 2004). One interpretation of the filamentary connection to

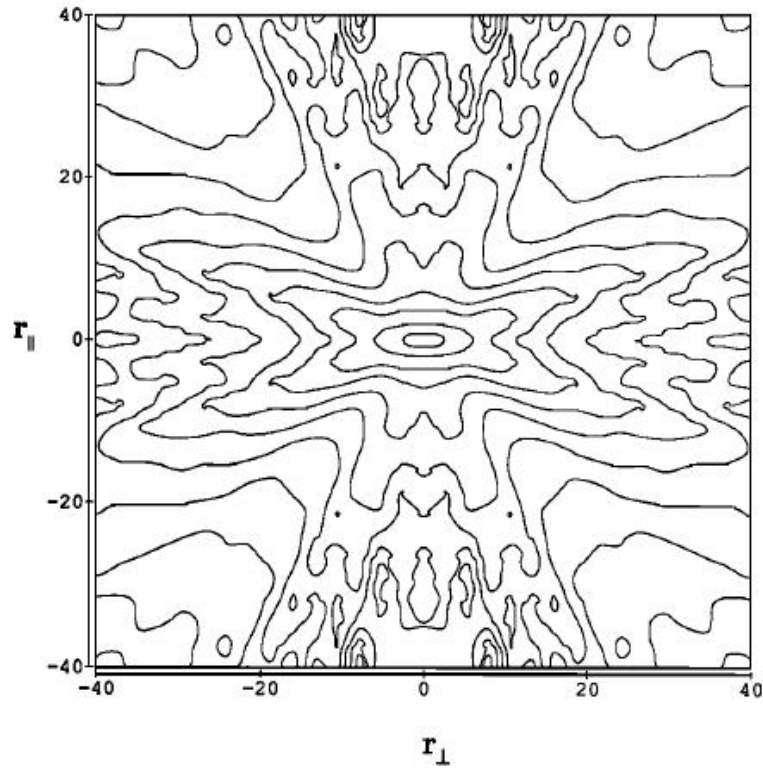


Figure 2.8: Contour plot of the two-dimensional correlation function of solar wind fluctuations as a function of distance parallel and perpendicular to the mean magnetic field using *ISEE 3* magnetometer data. [Image credit: Matthaeus et al. 1990]

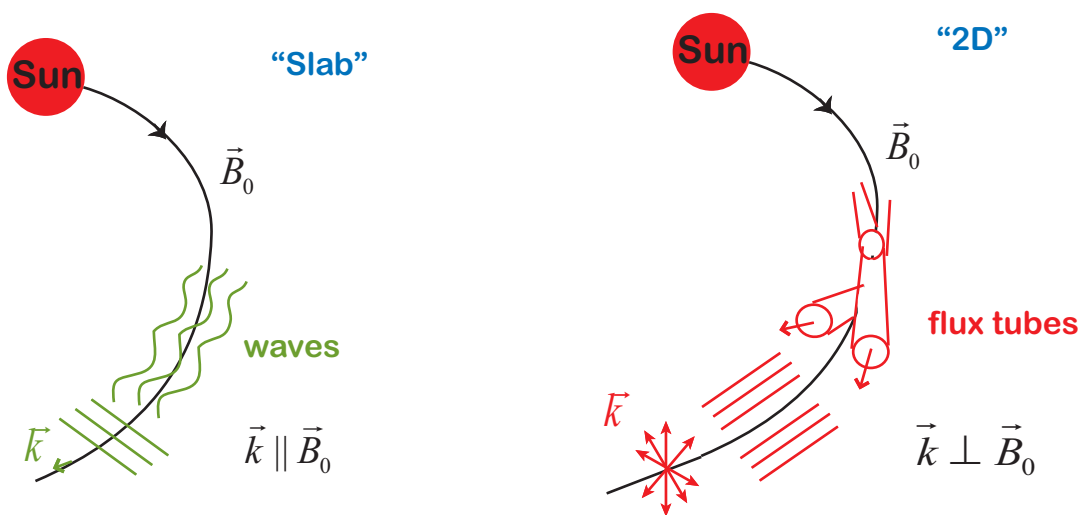


Figure 2.9: Schematic of populations of fluctuations in the solar wind.

the Sun is that the solar wind comprises “spaghetti” of winding flux tubes separated by sharp boundaries (Parker 1963b; McCracken & Ness 1966; Bruno *et al.* 2001; Borovsky 2008). In this view, the flux tube boundaries are taken to be distinct from the well-known magnetic fluctuations with a turbulent power spectrum (Jokipii & Coleman 1968). From another point of view, the apparent flux tube structure could be a natural consequence of the turbulent evolution of magnetic fluctuations in a plasma. Starting from fluctuations in the magnetic field at the solar wind source, the larger-scale structures evolve more slowly (Matthaeus *et al.* 1996), and could survive as “fossil turbulence” at a distance of 1 AU from the Sun (Giacone *et al.* 2006), while smaller-scale structures join a turbulent cascade (Kolmogorov 1941) to even smaller scales where the energy is dissipated (Coleman 1968; Verma *et al.* 1995; Leamon *et al.* 1998; Sahraoui *et al.* 2009).

Let us further discuss the turbulence point of view: Based on theoretical results that express the magnetic field line diffusion coefficient in terms of the turbulent power spectrum (Jokipii & Parker 1968; Matthaeus *et al.* 1995), it is a reasonable first step to model turbulent fluctuations by summing over Fourier modes with the appropriate power spectrum and to simply assign a random phase to each wave mode. Indeed, models of magnetic turbulence frozen-in from the solar source (Giacone *et al.* 2000), with two-components of slab and 2D fluctuations (Ruffolo *et al.* 2003; Chuychai *et al.* 2007), and with three-dimensional (3D) fluctuations (Zimbardo *et al.* 2004; Pommois *et al.* 2005) have all been able to generate filamentary magnetic connection that explain dropouts.

Ruffolo *et al.* (2003) proposed a new concept of transport, using the 2D+slab magnetic field model together with conditional statistics. The 2D field can be written in terms of a vector potential  $a(x, y)\hat{z}$ . An example of a contour plot of the potential function  $a(x, y)$  is illustrated in Figure 2.10. In the Figure, we identify O-points and X-points, where O-points are local minima or maxima of the potential function and X-points are saddle points. The conditional statistics concept is that the magnetic field lines that started from different locations will exhibit different transport. The field lines

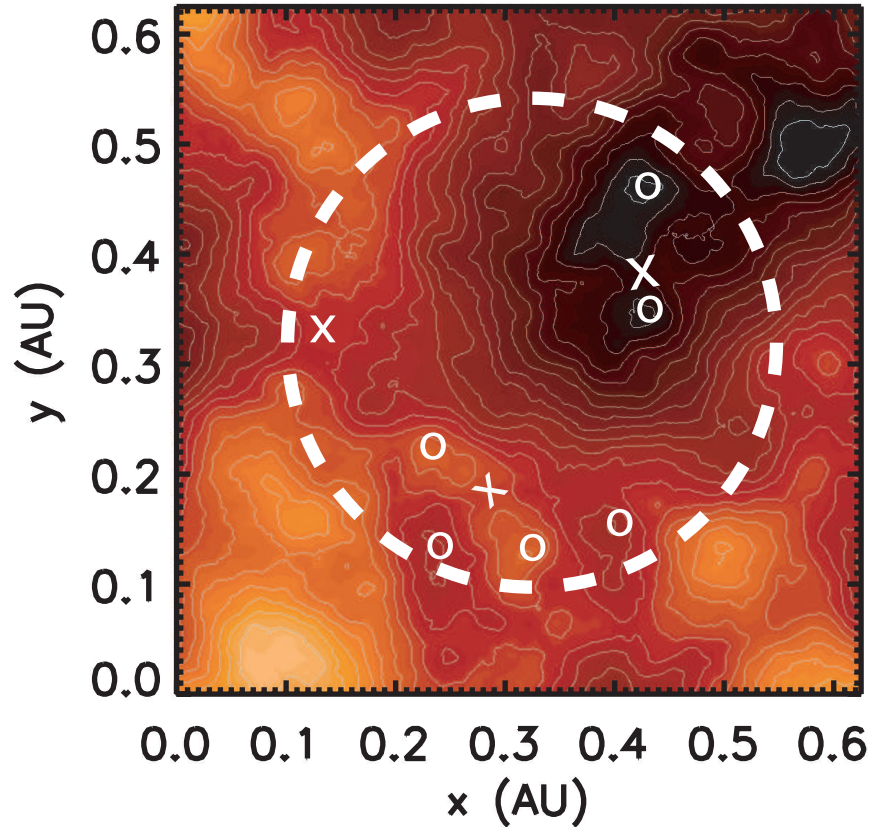


Figure 2.10: Contour plot of the potential function  $a(x, y)$  for a representation of 2D turbulence, indicating O-points and X-points. [Image credit: Chuychai et al. 2007]

that initially were near O-points experience only slab diffusion, and will be temporarily trapped in that local island, until they finally escape. In contrast, the field lines that initially start near X-points will experience normal diffusion, both slab diffusion and 2D diffusion, so they travel with a greater diffusion rate. This is the concept of temporary topological trapping.

Another mechanism to explain the sharp gradients in observed dropouts is suppressed diffusive escape. Chuychai *et al.* (2005) found that strong a 2D field can suppressed diffusion. They also calculated suppressed diffusion using quasi-linear theory. For 2D+slab turbulence, Chuychai *et al.* (2007) found that the filamentation of

magnetic connectivity to the source is sharply delineated by local trapping boundaries, defined as equipotential contours that have a maximum average 2D fluctuation energy compared with neighbouring contours. Figure 2.11 shows scatter plots of magnetic field line trajectories in 2D + slab turbulence at various distances  $z$ , for initial locations within a circular region at  $z = 0$ , for the same representation of 2D turbulence as in Figure 2.10. The blue curves are the mathematically defined LTBs. The red shading indicates the values of  $|b^{2D}|^2$  corresponding to the contour plot of  $a(x, y)$  in Figure 2.10. The LTBs reflect the concept of temporary trapping along closed 2D orbits, with eventual escape due to slab fluctuations, as well as the suppression of slab diffusive escape where the 2D field is strong.

Another concern is the space filling of the field line trapping regions (Kaghashvili *et al.* 2006), because a high space filling could inhibit the transport of particles perpendicular to the mean magnetic field. In the random-phase 2D+slab model, the 2D “islands” of temporary field line trapping are delineated by LTBs, yielding a moderate space filling (Chuychai *et al.* 2007). Field lines in the interstitial “network” can rapidly diffuse perpendicular to the mean field (Ruffolo *et al.* 2003). This result is consistent with observations of SEP from impulsive solar events. Flux-limited surveys, which require a substantial particle intensity, indicate a narrow distribution for such events in solar longitude (Reames 1992). This indicates only limited lateral spreading for the bulk of SEPs, which we attribute to trapping within small-scale topological islands, representing a “core” region of high particle density (see Figure 1.8). At the same time, observations of type III radio bursts, which are sensitive to very low particle fluxes, indicate that SEPs can undergo lateral motion by up to  $\sim 90^\circ$  in solar longitude during their transport from the Sun to Earth orbit (Cane & Erickson 2003). This laterally extended but less intense “halo” of SEPs corresponds to particles on field lines initially located in interstitial regions between the 2D islands. Indeed, the absence of these halo SEPs from the core region is manifested as dropouts.

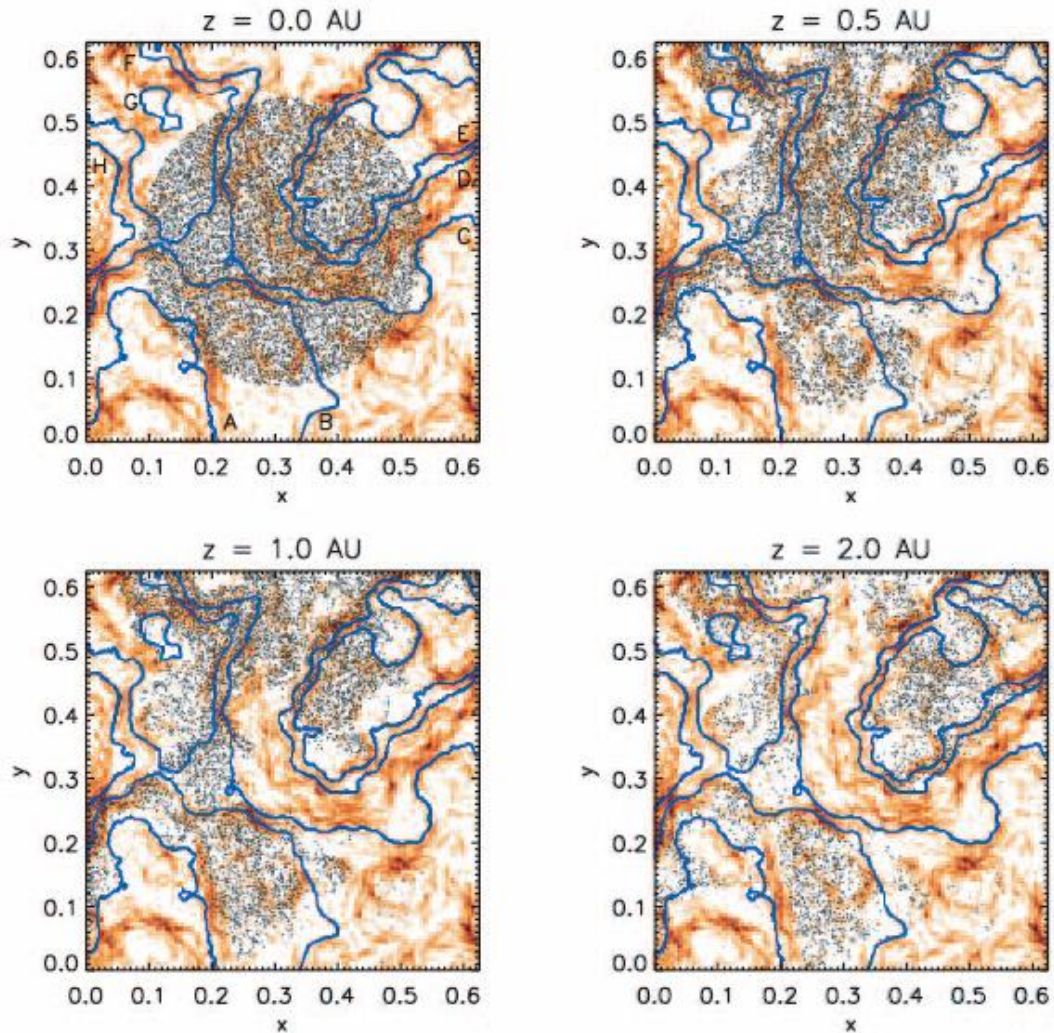


Figure 2.11: Scatter plots of magnetic field line trajectories at various distances  $z$ . [Image credit: Chuychai et al. 2007]

In contrast, descriptions of the flux tube viewpoint typically propose space-filling trapping regions, sometimes with a strict interpretation of field line confinement in the flux tubes (see Figure 1 and Section 8.1 of Borovsky 2008). Even if one invokes a “cross-field” diffusion mechanism whereby particles can cross field lines, it is difficult to reconcile escape that is slow enough to preserve dropout features with the rapid diffusion of SEPs as inferred from observations over short time scales (Cane & Erickson 2003) and

long time scales (McKibben *et al.* 2001; McKibben 2005), as well as the important role played by perpendicular diffusion in the solar cycle dependent modulation of Galactic cosmic rays (Parker 1965; Moraal 1976; Cane *et al.* 1999; Reinecke *et al.* 2000).

Now the distinctions between the flux tube view and the turbulence view are sometimes not recognized. For example, in the context of observationally testing the concepts developed from turbulence models, Chollet & Giacalone (2008) pointed out that dropout features are not well correlated with sharp magnetic field changes (such as current sheets). However, that observation actually addresses the flux tube view, in which trapping within flux tubes is naturally envisioned as delineated by magnetic field changes, whereas simulations of random-phase turbulence had indicated trapping within LTBs. In general, the lack of an observed association between dropouts and features of the magnetic field or current (Mazur *et al.* 2000; Gosling *et al.* 2004; Chollet & Giacalone 2008) is problematic for the flux tube view, in which the only surfaces available to trap plasma and field lines are, by assumption, the flux tube boundaries themselves.

Random-phase turbulence models do not properly treat sharp changes in the magnetic field, such as current sheets, and thus cannot be tested in this way. In this work, we explore the properties of a more realistic two-dimensional magnetohydrodynamic (2D MHD) turbulence model, in which current sheets develop and the current and magnetic field have characteristic non-Gaussian statistical properties. We find that the 2D MHD + slab model of turbulent fluctuations includes some realistic features of the flux tube view and is consistent with the lack of an observed association between dropouts and intense magnetic fields or currents.

## CHAPTER III

### EXISTING NUMERICAL TECHNIQUES

This chapter explains details of the magnetic field model, how to generate slab field and 2D field (both 2D random-phase field and 2D MHD field), and how to trace magnetic field lines and charged particle trajectories in both Cartesian and spherical geometry. These are existing numerical techniques that I made use of in my work.

#### 3.1 Magnetic Field Model

##### 3.1.1 Cartesian Geometry

In this work, we express the interplanetary magnetic field as

$$\mathbf{B} = B_0 \hat{\mathbf{z}} + \mathbf{b}(x, y, z), \quad (3.1)$$

where  $B_0 \hat{\mathbf{z}}$  is a constant mean field and  $\mathbf{b}$  is the transverse fluctuating part, which can be separated into two components, a “slab” component that depends only on the  $z$  coordinate and a “2D” component that depends only on the  $x$  and  $y$  coordinates. The motivation for this two-component model was provided in Section 2.3. Thus  $\mathbf{b}$  can be written as

$$\mathbf{b}(x, y, z) = \mathbf{b}^{slab}(z) + \mathbf{b}^{2D}(x, y). \quad (3.2)$$

Because  $\nabla \cdot \mathbf{B} = 0$ , we have  $\nabla \cdot \mathbf{b}^{2D} = 0$  and  $\mathbf{b}^{2D} = \nabla \times [a(x, y) \hat{\mathbf{z}}]$  for a scalar potential function  $a(x, y)$ . Illustrations of slab and 2D fluctuations are shown in Figs. 3.1 and 3.2, respectively. If there were only 2D fluctuations, the magnetic field lines would exactly follow 2D flux surfaces defined by contours of constant potential, but the addition of the slab component allows field lines to diffuse away from the 2D flux surfaces, yielding a fully three-dimensional model.

This magnetic field model was motivated by the work of Matthaeus *et al.* (1990), who found that the fluctuation power of the solar wind is concentrated at wave



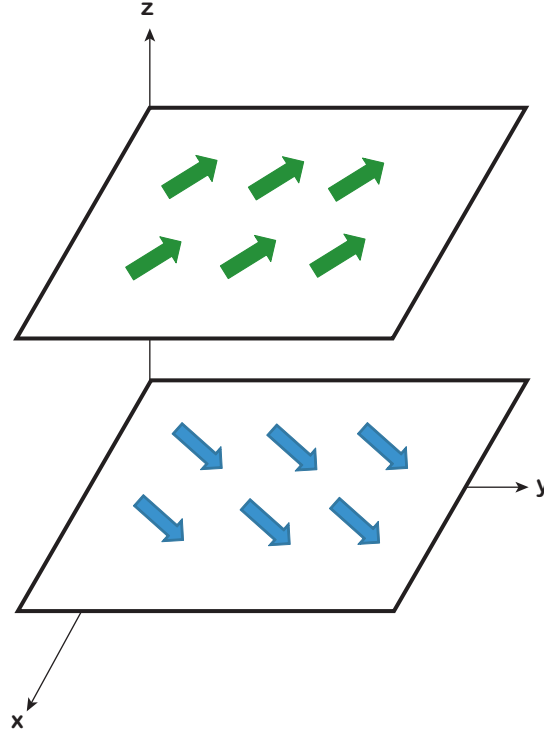


Figure 3.1: Illustration of slab fluctuations,  $\mathbf{b}^{slab}(z)$ .

vectors nearly perpendicular and parallel to the mean magnetic field (see also Dasso *et al.* 2005; Weygand *et al.* 2009). In addition to its use in the study of dropouts, the two-component model has also provided a useful description of solar wind fluctuations (Bieber *et al.* 1996; Saur & Bieber 1999; Osman & Horbury 2007) and the parallel transport of particles in interplanetary space (Beiber *et al.* 1994; Shalchi *et al.* 2008).

### 3.1.2 Spherical Geometry

Let us first introduce the coordinates that we use for simulations. Figure 3.3 illustrates the coordinates  $(\varphi, \Lambda, r)$ , where  $\varphi$  is the heliolongitude,  $\Lambda$  is the heliolatitude, and  $r$  is the radial distance from the center of the Sun. The two-component magnetic field model becomes

$$\mathbf{B}(\varphi, \Lambda, r) = \frac{\mathbf{B}_1 r_1^2}{r^2} + \frac{[\mathbf{b}^{slab}(r) + \mathbf{b}^{2D}(\varphi, \Lambda)] r_1^2}{r^2}, \quad (3.3)$$

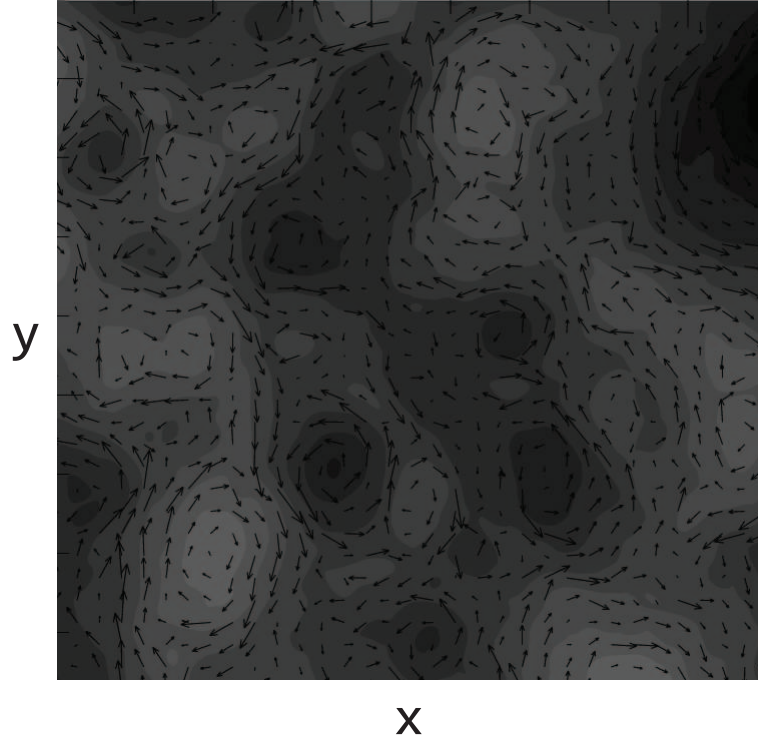


Figure 3.2: An example of contour plot of a 2D potential function  $a(x, y)$ . Arrows indicate directions of magnetic fields. Darker shading represents higher values of the potential function, whereas lighter shading represents lower values of the potential function. Near a maximum of the potential function, the magnetic field lines will go in the counter-clockwise direction. On the other hand, near minimum values of the potential function, the magnetic field lines will go in the clockwise direction.

where  $\mathbf{B}_1 = B_1 \hat{\mathbf{r}}$ , and the slab fluctuation  $\mathbf{b}^{\text{slab}}$  depends on the  $r$  coordinate, the radial distance from the Sun. The other fluctuation,  $\mathbf{b}^{2\text{D}}$ , depends on the lateral  $\varphi$  and  $\Lambda$  coordinates. For the 2D component, we can write  $\mathbf{b}^{2\text{D}}(\varphi, \Lambda) = \nabla \times [a(\varphi, \Lambda) \hat{\mathbf{r}}]$ , where  $a\hat{\mathbf{r}}$  is a vector potential for the 2D component, we call  $a(\varphi, \Lambda)$  the potential function, and  $r_1$  is a reference position, which is set to 1 AU.

### 3.2 Slab Field Generation

To numerically generate the fluctuating fields, we require a Kolmogorov power spectrum of turbulence in the inertial region of  $k$ -space. For the slab component we can write

$$P_{xx}^{\text{slab}}(k_z) = P_{yy}^{\text{slab}}(k_z) = \frac{C^{\text{slab}}}{[1 + (k_z \lambda)^2]^{5/6}}, \quad (3.4)$$

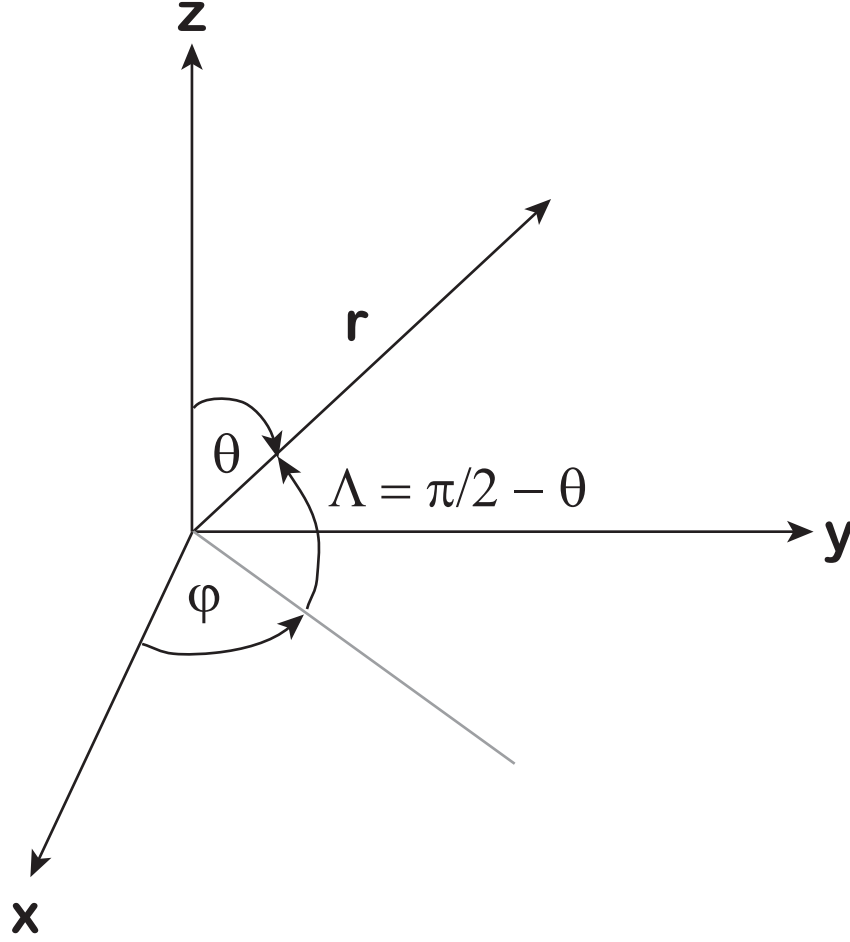


Figure 3.3: Coordinates for simulations in spherical geometry.

where  $C^{slab}$  is a normalization constant and  $\lambda$  is the parallel coherence length, set to 0.02 AU. This spectral form yields a Kolmogorov power law,  $k_z^{-5/3}$ , in the inertial range at higher  $k_z$ , and is independent of  $k_z$  in the energy-containing range at lower  $k_z$ ; such spectra have been found in observations of solar wind fluctuations (Jokipii & Coleman 1968). The magnetic field in the wave vector domain can be written as

$$b_x^{slab}(k_z) = \sqrt{P_{xx}^{slab}(k_z)} e^{i\phi_x(k_z)}, \quad (3.5)$$

where  $i$  is  $\sqrt{-1}$  and  $\phi_x$  is a random phase that is independent for each Fourier mode, varying from 0 to  $2\pi$ . For the  $y$ -component we use

$$b_y^{slab}(k_z) = \sqrt{P_{yy}^{slab}(k_z)} e^{i\phi_y(k_z)}. \quad (3.6)$$

Because of the use of random phases  $\phi_x$  and  $\phi_y$  this can be called a random-phase field.

Then we use an inverse fast Fourier transform to obtain the fluctuating magnetic fields in real space. In our simulations, we set the box length in the  $z$  direction to  $L_z = 10,000\lambda$ , and the number of grid points was  $N_z = 4,194,304$ . The field lines are traced only to a few percent of the simulation box length in order to avoid periodic effects.

### 3.3 2D Field Generation

#### 3.3.1 2D Random-Phase Field

The power spectrum of the random-phase 2D potential is

$$A(k_\perp) = \frac{C^{2D}}{[1 + (k_\perp \ell_\perp)^2]^{7/3}}, \quad (3.7)$$

where  $A(k_\perp)$  is the power spectrum of  $a(x, y)$ , defined as the Fourier transform of the correlation function  $\langle a(\mathbf{r}_0)a(\mathbf{r}_0 + \mathbf{r}) \rangle$ ,  $C^{2D}$  is a normalization constant,  $k_\perp = \sqrt{k_x^2 + k_y^2}$ , and  $\ell_\perp$  is a perpendicular coherence length, set to 0.1 AU (similar to the value used by Ruffolo *et al.* 2003). Note that  $P_{xx}(\mathbf{k}) = k_y^2 A(k_\perp)$  and  $P_{yy}(\mathbf{k}) = k_x^2 A(k_\perp)$ . This leads to an omnidirectional power spectrum,  $\mathcal{E}(k_\perp) = 2\pi k_\perp (P_{xx} + P_{yy})$ , with a Kolmogorov power law in the inertial range and a  $k_\perp^2$ -dependence of the modal power spectrum ( $P_{xx} + P_{yy}$ ) in the energy-containing range as required for homogeneity (Ruffolo *et al.* 2004; Matthaeus *et al.* 2007). The magnetic potential for the 2D component in the wave number domain is

$$a(k_x, k_y) = \sqrt{A(k_\perp)} e^{i\phi(k_x, k_y)}, \quad (3.8)$$

where  $\phi$  is a random phase. We derived  $b_x^{2D}(\mathbf{k})$  and  $b_y^{2D}(\mathbf{k})$ , and used the fast Fourier transform (FFT) algorithm (Press *et al.* 1992) to perform the inverse Fourier transform to obtain  $\mathbf{b}^{2D}(x, y)$  in the spatial domain of box lengths  $L_x = L_y = 40\lambda$ . The numbers of grid points were  $N_x = N_y = 1,024$ . An example of a 2D random-phase potential function  $a(x, y)$  generated in this manner is shown in Figure 3.4a.

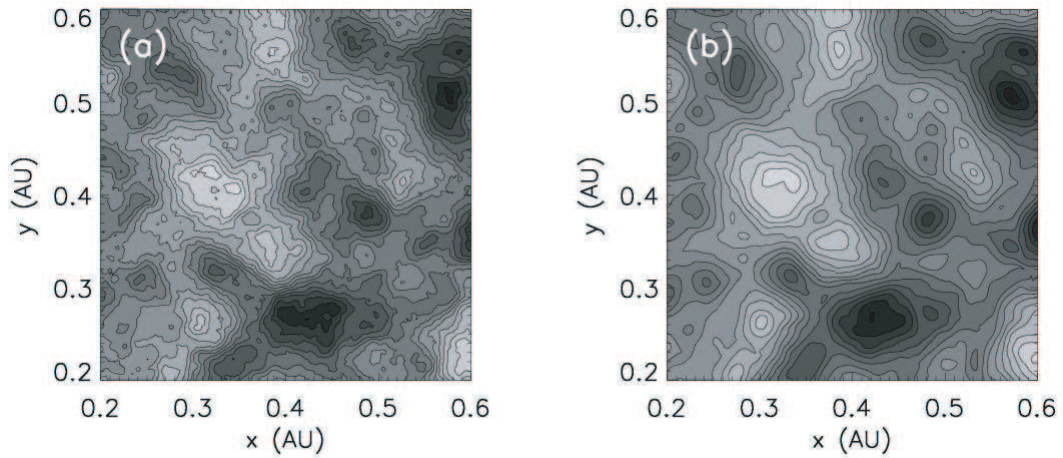


Figure 3.4: (a) Contour plot of a 2D random-phase potential function. (b) Same field after a 2D MHD procedure.

### 3.3.2 2D MHD Field

Random-phase models of magnetic fields encode the desired power spectrum, e.g., for a turbulent plasma, and since the power spectrum is the Fourier transform of the spatial correlation function, the latter should be correctly treated as well, in the ensemble average. However, random-phase models have some physical deficiencies, especially in two or more dimensions. Therefore, for the 2D magnetic field component, we have developed a procedure for “processing” a random-phase field according to MHD in two dimensions.

According to MHD, the magnetic pressure depends on  $b^2$ , so the turbulent flow will tend to make  $|\mathbf{b}|$  more uniform. Thus the current  $\mathbf{j}$ , which depends on  $\nabla \times \mathbf{b}$ , is reduced in most locations, but remains at topological “defects” where  $\mathbf{b}$  changes in magnitude and/or direction. This topological structure is a key feature of the flux tube viewpoint, and the topology requires current cores in the interior and current sheets at the flux tube boundary (Matthaeus & Lamkin 1986; Greco *et al.* 2009); these will be discussed further in Section 5.1. Along the flux tube boundary, the attraction of parallel current elements should concentrate such currents into narrow regions, such as current

sheets with magnetic reconnection. Thus the current sheets should be envisioned as not uniformly spread over the flux tube boundary but rather concentrated at narrow portions thereof.

A random-phase 2D field assumes independent Fourier modes and therefore does not incorporate the tendency of  $|\mathbf{b}|$  to become more uniform and  $|\mathbf{j}|$  to become more concentrated, which require that many Fourier modes “conspire” to concentrate changes in the magnetic field and form coherent current structures in localized regions.

In the solar wind, we expect that an initial fluctuation field, e.g., from the solar source, should undergo substantial MHD evolution before arriving at Earth. The dynamical age of the solar wind at Earth orbit can be roughly estimated from

$$\frac{T}{T_{nl}} = C_{ch} \frac{R/U}{L/Z}, \quad (3.9)$$

where  $T$  is the solar wind travel time from the Sun,  $T_{nl}$  is a nonlinear scale time, specifically, the eddy turnover time at the outer scale,  $C_{ch} = 0.5$  is a constant to account for cross-helicity (Alfvénic) effects (see Hossain *et al.* 1996),  $R$  is the distance from the Sun,  $U$  is the solar wind speed,  $L$  is the outer scale of the turbulence, and  $Z$  is the eddy velocity at the outer scale. Using  $R = 1$  AU and observations at 1 AU of  $U = 300$  to  $600$  km s<sup>-1</sup>,  $L = 0.01$  AU (Weygand *et al.* 2009), and  $Z = 20$  to  $40$  km s<sup>-1</sup> (see Smith *et al.* 2001, for observations of the normal component of  $Z^2$ ), it can be estimated that the solar wind experiences  $\sim 2$  to  $17$  nonlinear scale times on its way to Earth orbit. Because there is continual energy input (e.g., Matthaeus *et al.* 1998), the solar wind turbulence is fully developed at 1 AU, and the power spectrum is observed to be close to a Kolmogorov form (Jokipii & Coleman 1968).

In the present work we model such turbulent evolution by starting from an initial random-phase 2D field, which incorporates a turbulent power spectrum. Then a 2D pseudospectral incompressible MHD code (see Wan *et al.* 2009) is employed to evolve

the magnetic configuration according to the following equations of evolution,

$$\begin{aligned}\frac{\partial \omega}{\partial t} + \mathbf{v} \cdot \nabla \omega &= \mathbf{b} \cdot \nabla j + \nu \nabla^2 \omega \\ \frac{\partial a}{\partial t} + \mathbf{v} \cdot \nabla a &= \eta \nabla^2 a,\end{aligned}\tag{3.10}$$

in terms of the plasma vorticity  $\omega = (\nabla \times \mathbf{v}) \cdot \hat{\mathbf{z}}$ , plasma velocity  $\mathbf{v}$ , current  $j = (\nabla \times \mathbf{b}) \cdot \hat{\mathbf{z}}$ , molecular viscosity  $\nu$ , and resistivity  $\eta$ . The simulation has a  $1,024 \times 1,024$  spatial resolution and a magnetic Reynolds number of 640 at the largest scales. Because 2D MHD simulations do not include energy input to the turbulence, and use a lower Reynolds number than solar wind turbulence, their turbulent energy decays more quickly than that in the solar wind. Here, the simulation is run from  $t = 0$  to  $T_{nl}$ , which is sufficient for developing nonlinear structures (i.e., phase correlations of Fourier components) but not so long as to severely distort the power spectrum away from a Kolmogorov form. At  $t \sim T_{nl}$ , the decaying turbulence has reached the peak of its dissipation and most closely resembles steady-driven fully developed turbulence as expected in the solar wind. We then obtain the 2D MHD potential, magnetic field, and current.

For the 2D field, we map a potential function  $a_0$  of two Cartesian coordinates,  $x$  and  $y$ , onto the longitude,  $\varphi$ , and latitude,  $\Lambda = \pi/2 - \theta$ , respectively, at a reference radius  $r_0 = 1$  AU. In doing so, the only concern is that 2D structures become distorted (shortened in longitudinal distance) by a factor  $\sin \theta = \cos \Lambda$ ; thus the procedure is accurate for small values of  $|\Lambda|$ .

### 3.4 Field Line Tracing

#### 3.4.1 Cartesian Geometry

After obtaining the magnetic field at each grid point of the simulation box, magnetic field line trajectories were found by solving the coupled equations

$$\frac{dx}{dz} = \frac{b_x^{2D}(x, y) + b_x^{slab}(z)}{B_0}, \quad \frac{dy}{dz} = \frac{b_y^{2D}(x, y) + b_y^{slab}(z)}{B_0}\tag{3.11}$$

to obtain  $x(z)$  and  $y(z)$ . We solve equation (3.11) using a fourth-order Runge-Kutta method with an adaptive step size (Press *et al.* 1992). The magnetic field at each

position is obtained by linear interpolation (slab component) and bilinear interpolation (2D component). Example of trajectories of field lines in pure slab turbulence are shown in Figure 3.5, for pure 2D fluctuations in Figure 3.6, and for 2D+slab fluctuations in Figure 3.7.

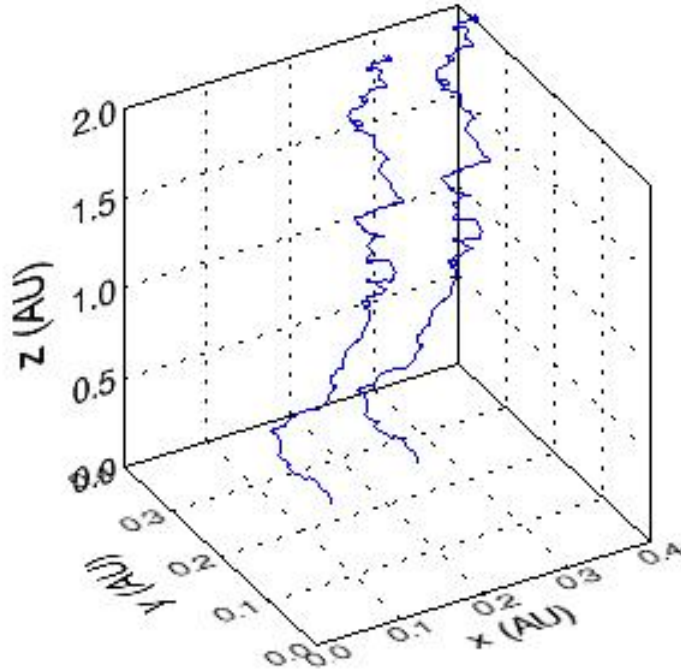


Figure 3.5: Example of two trajectories of magnetic field lines in pure slab turbulence.

### 3.4.2 Spherical Geometry

For spherical geometry, the streamline equation becomes

$$\frac{dr}{B_r} = \frac{rd\Lambda}{B_\Lambda} = \frac{r \cos \Lambda d\varphi}{B_\varphi}, \quad (3.12)$$



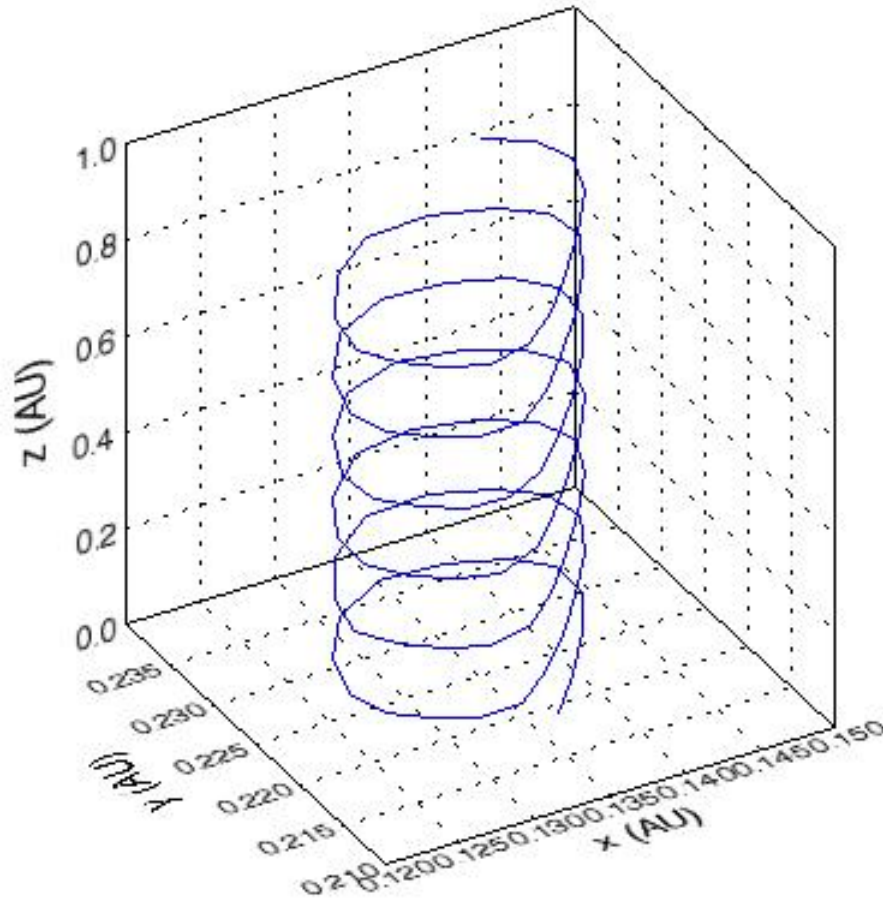


Figure 3.6: Example of a trajectory of a magnetic field line in pure 2D turbulence.

which can be written in terms of components as

$$\frac{d\Lambda}{dr} = \frac{1}{r} \frac{B_\Lambda}{B_r}, \quad (3.13)$$

$$\frac{d\varphi}{dr} = \frac{1}{r \cos \Lambda} \frac{B_\varphi}{B_r}. \quad (3.14)$$

We also solve equations (3.13) using a fourth-order Runge-Kutta method with adaptive step size. An example of a trajectory of a magnetic field line in spherical geometry is shown in Figure 3.8.

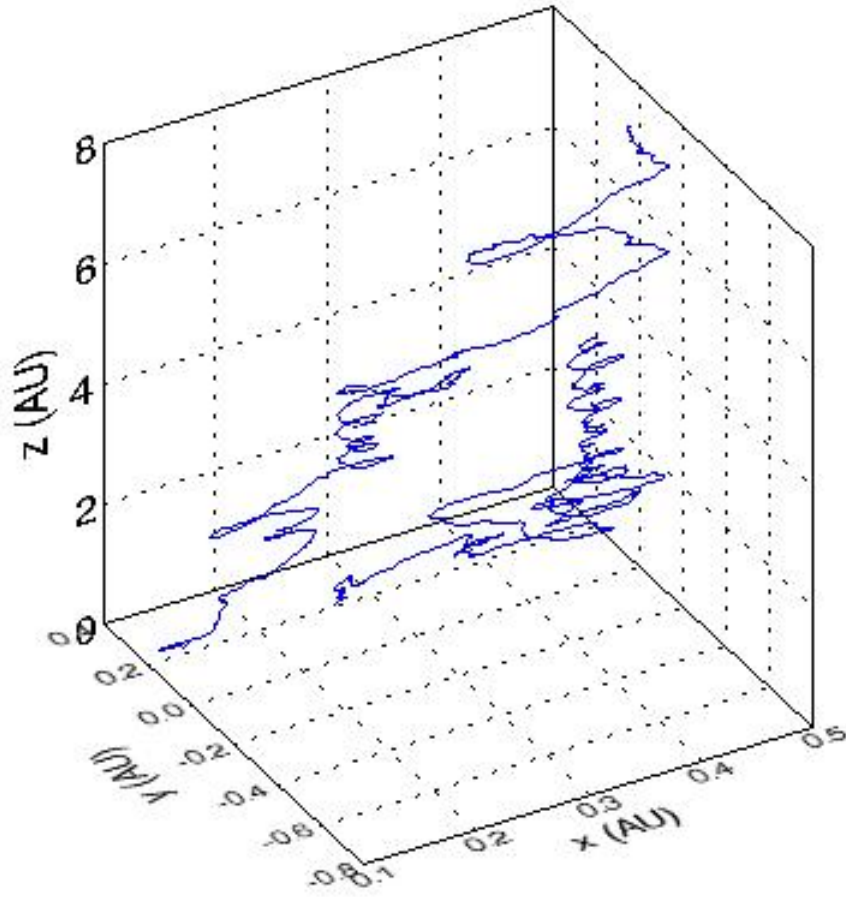


Figure 3.7: Example of two trajectories of magnetic field lines in 2D+slab turbulence.

### 3.5 Particle Tracing

#### 3.5.1 Cartesian Geometry

For particle trajectories, we solve the Newton-Lorentz equation:

$$\gamma m \dot{\mathbf{v}} = q(\mathbf{v} \times \mathbf{B}), \quad (3.15)$$

where  $\gamma = 1/\sqrt{1 - v^2/c^2}$  is the Lorentz factor,  $m$  is the particle mass,  $\mathbf{v}$  is the particle velocity,  $c$  is the speed of light, and  $q$  is the particle charge. In terms of components, eq.

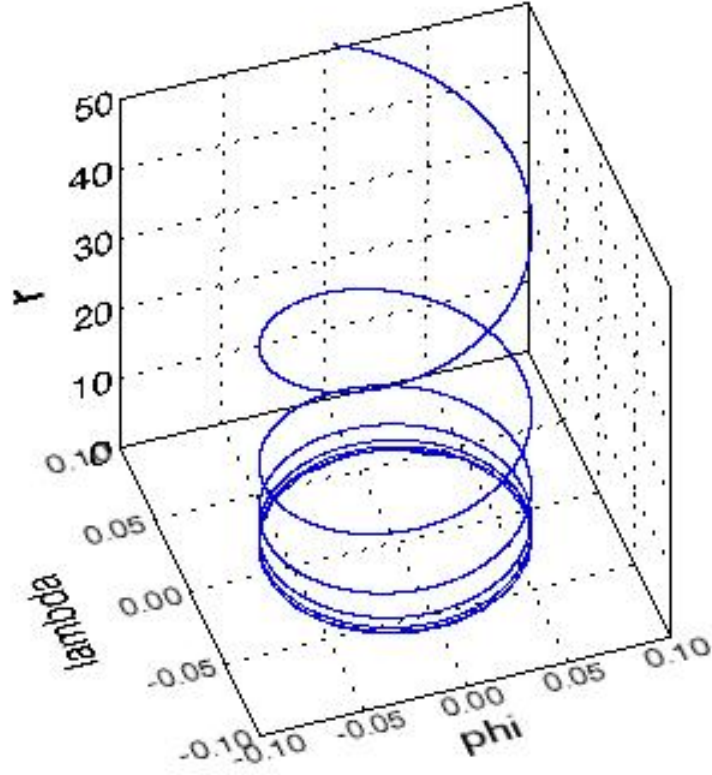


Figure 3.8: Example of a trajectory of a magnetic field line in spherical geometry.

3.15 can be written as

$$\dot{v}_x = \frac{q}{\gamma m}(v_y B_z - B_y v_z) \quad (3.16)$$

$$\dot{v}_y = \frac{q}{\gamma m}(v_z B_x - B_z v_x) \quad (3.17)$$

$$\dot{v}_z = \frac{q}{\gamma m}(v_x B_y - B_x v_y). \quad (3.18)$$

We scale the variables by  $\mathbf{v}^* = \mathbf{v}/c$ ,  $t^* = t/\tau_c$ ,  $\mathbf{B}^* = \mathbf{B}/B_0$ , and  $\alpha = (qB_0\tau_c)/(\gamma m)$ . Then the equations of motion become (see Appendix A)

$$\frac{dv_x^*}{dt^*} = \alpha(v_y^* B_z^* - B_y^* v_z^*) \quad (3.19)$$

$$\frac{dv_y^*}{dt^*} = \alpha(v_z^* B_x^* - B_z^* v_x^*) \quad (3.20)$$

$$\frac{dv_z^*}{dt^*} = \alpha(v_x^* B_y^* - B_x^* v_y^*). \quad (3.21)$$

These equations are solved by using a fourth-order Runge-Kutta method with adaptive step size. Some results will be shown in Chapter 5.

### 3.5.2 Spherical Geometry

Starting from the Lagrangian, then we get the Hamiltonian. Then we can find equations of motion for a particle in spherical geometry as follows (See Appendix B):

$$v_\varphi = r \cos \Lambda \dot{\varphi} \quad (3.22)$$

$$v_\Lambda = r \dot{\Lambda} \quad (3.23)$$

$$v_r = \dot{r} \quad (3.24)$$

$$\dot{v}_\varphi = -\frac{v_r v_\varphi}{r} + \frac{v_\Lambda v_\varphi}{r \cot \Lambda} + \frac{q}{\gamma m} (v_\Lambda B_r - B_\Lambda v_r) \quad (3.25)$$

$$\dot{v}_\Lambda = -\frac{v_\varphi^2}{r \cot \Lambda} - \frac{v_r v_\Lambda}{r} + \frac{q}{\gamma m} (v_r B_\varphi - v_\varphi B_r) \quad (3.26)$$

$$\dot{v}_r = \frac{v_\Lambda^2}{r} + \frac{v_\varphi^2}{r} + \frac{q}{\gamma m} (v_\varphi B_\Lambda - v_\Lambda B_\varphi). \quad (3.27)$$

These equations are also solved by using a fourth-order Runge-Kutta method with adaptive step size. The results will be shown in Chapter 6.

## CHAPTER IV

### NEW NUMERICAL SIMULATION TECHNIQUES

In this chapter, we present three new numerical techniques. The first two are useful for testing the particle trajectory code. The third concerns how to find LTBs.

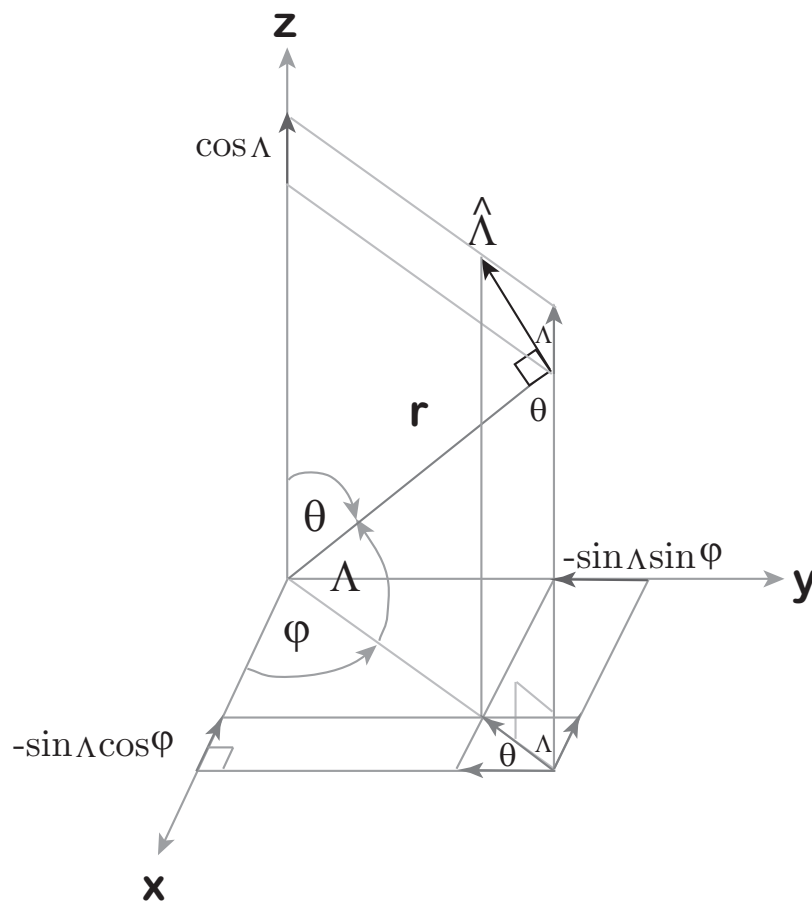


Figure 4.1: Components of  $\hat{\Lambda}$  in spherical geometry.

#### 4.1 Test with a Uniform Magnetic Field in the $x$ Direction

The best way to test a computer simulation code, and our proper use of the code, is to perform simulations for a simple case for which we already know the answer. In this case, we want to know whether every component of our equations of motion is treated properly, e.g., only a radial field cannot satisfy this purpose because some of the components are equal to zero. Hence we select a magnetic field that has all three components in spherical geometry. For this technique, we trace particle trajectories in spherical geometry for a magnetic field that is equivalent to a uniform field in the  $x$  direction. We can find the magnetic field by noting that the spherical geometry that we use has the following unit vectors:

$$\hat{\phi} = -\sin \varphi \hat{x} + \cos \varphi \hat{y}, \quad (4.1)$$

$$\hat{\Lambda} = -\sin \Lambda \cos \varphi \hat{x} - \sin \Lambda \sin \varphi \hat{y} + \cos \Lambda \hat{z}, \quad (4.2)$$

$$\hat{r} = \cos \Lambda \cos \varphi \hat{x} + \cos \Lambda \sin \varphi \hat{y} + \sin \Lambda \hat{z}, \quad (4.3)$$

where  $\hat{\Lambda}$  can be found as in Figure 4.1. We can find the magnetic field in spherical

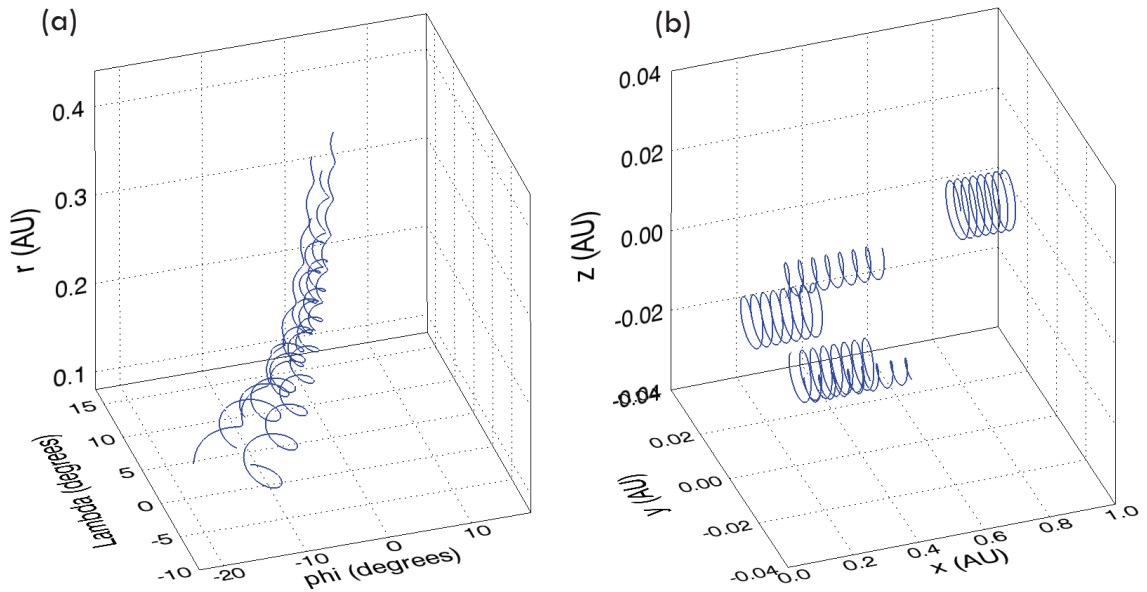


Figure 4.2: Test particles of 1 GeV in (a) spherical geometry and transforming to (b) Cartesian coordinates.

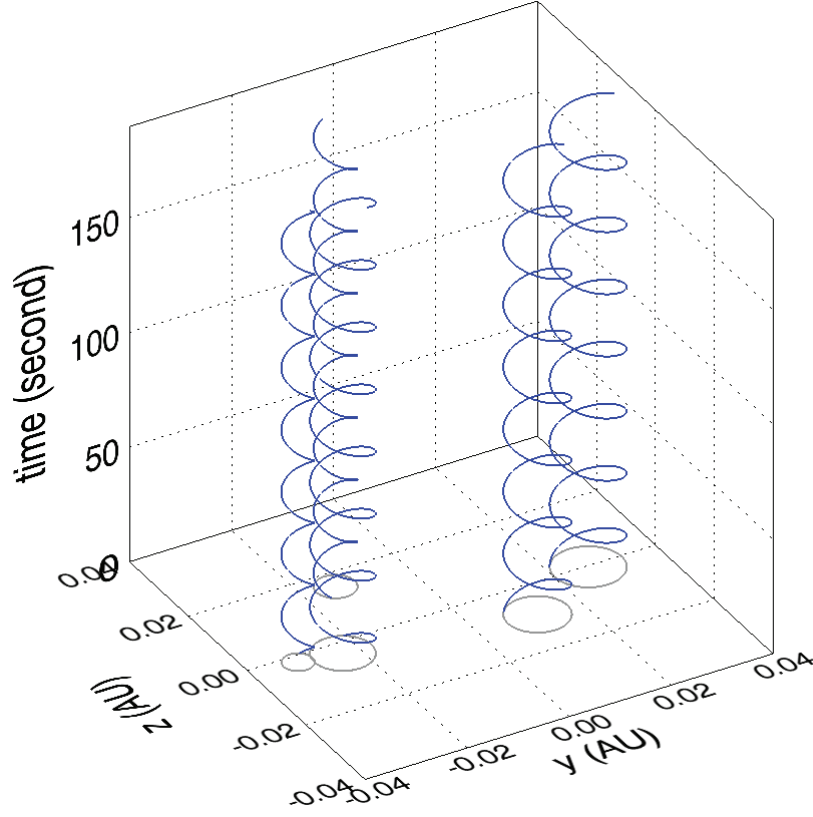


Figure 4.3: Trajectories of particles in the  $y$ - $z$  plane vs. time. The gyromotions are circles (shown in grey color) moving clockwise with time.

coordinates from

$$B_0 \hat{x} = B_0 [(\hat{x} \cdot \hat{\varphi})\hat{\varphi} + (\hat{x} \cdot \hat{\Lambda})\hat{\Lambda} + (\hat{x} \cdot \hat{r})\hat{r}] \quad (4.4)$$

$$= B_0 [-\sin \varphi \hat{\varphi} - \sin \Lambda \cos \varphi \hat{\Lambda} + \cos \Lambda \cos \varphi \hat{r}]. \quad (4.5)$$

We traced particles of energy 1 GeV. The results are shown in Figs. 4.2 and 4.3. The gyro-radius of these particles is about 0.007684-0.007689 AU, compared with the gyro-radius from theory, 0.007558 AU. From these results, we can conclude that our particle code is working properly for all components.

## 4.2 Test with a Radial Field

We use this technique to test whether we use the correct value of the magnetic field. Only looking at the trajectories or scatter plots cannot tell us that we used the

correct value for the magnetic field. For example, a proton will gyrate clockwise along a uniform magnetic field despite of the weakness or strongness of the field. Therefore, to make sure that we have used the correct value of the magnetic field, we have to measure other physical quantities, in this case the gyroradius and gyrofrequency.

For this technique, we traced proton trajectories in a radial field and determined the gyroradius and the gyrofrequency of the protons. We can compare the gyroradius  $R$  from 1) graphs of results at 1.0 AU, 2) the expected formula  $R = v_{\perp}/\omega$  using values output by the simulation program, where  $v_{\perp} = v \sin \theta$  and  $\theta$  is the pitch angle, which is the angle between the velocity of the particle and magnetic field, and 3) the value expected based on input values at 0.1 AU. Similarly, we compare values of the gyrofrequency, which should be given by  $\omega = qB/\gamma m$ . Figures 4.4 - 4.7 show plots of  $\varphi$  and  $\Lambda$  vs. time. Gyro-radii and gyro-frequencies from theory and the simulations are shown for protons of energy 1 MeV, 10 MeV, 100 MeV, and 1 GeV in Tables 4.1 and 4.2, respectively. We can calculate the gyrofrequency from the graphs by fitting crests (troughs) with  $2^{nd}$ -order polynomials to find the maxima (minima). Then the time difference between two maxima or minima is the period  $T$ . Then we can find the gyrofrequency from  $\omega = 2\pi/T$ . The gyroradius is also determined from the graphs. In order to calculate the gyroradius from the formula based on simulation values, we first calculate the pitch angle of the particle from  $\theta = \arccos(\mathbf{v} \cdot \mathbf{B})/(|\mathbf{v}||\mathbf{B}|)$ . Then we find the gyroradius by the definition given. We use the gyroradius in terms of angle because of two reasons: first, we perform the simulations in angular coordinates and second, the angular gyroradius is expected to be equal at all distances  $r$ . From the results, with little difference between the various values, we can conclude that we have used the correct value of the magnetic field.



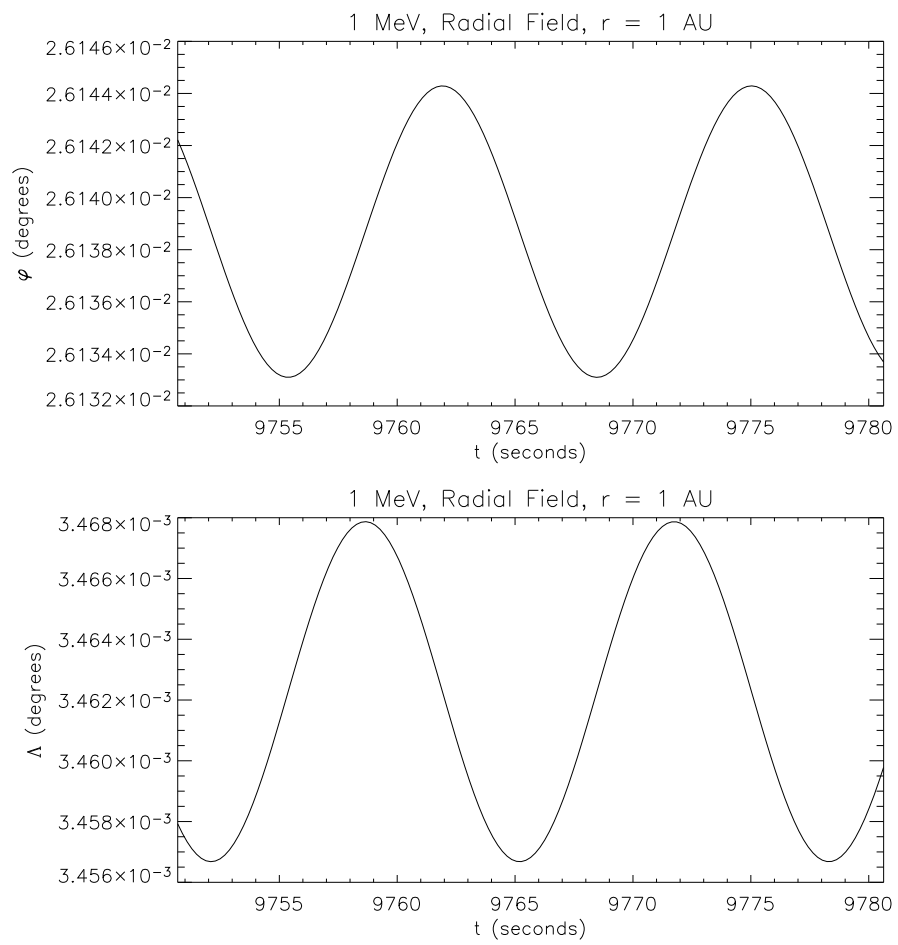


Figure 4.4: Upper panel shows  $\varphi$  versus time and lower panel shows  $\Lambda$  versus time from simulations of 1 MeV protons.

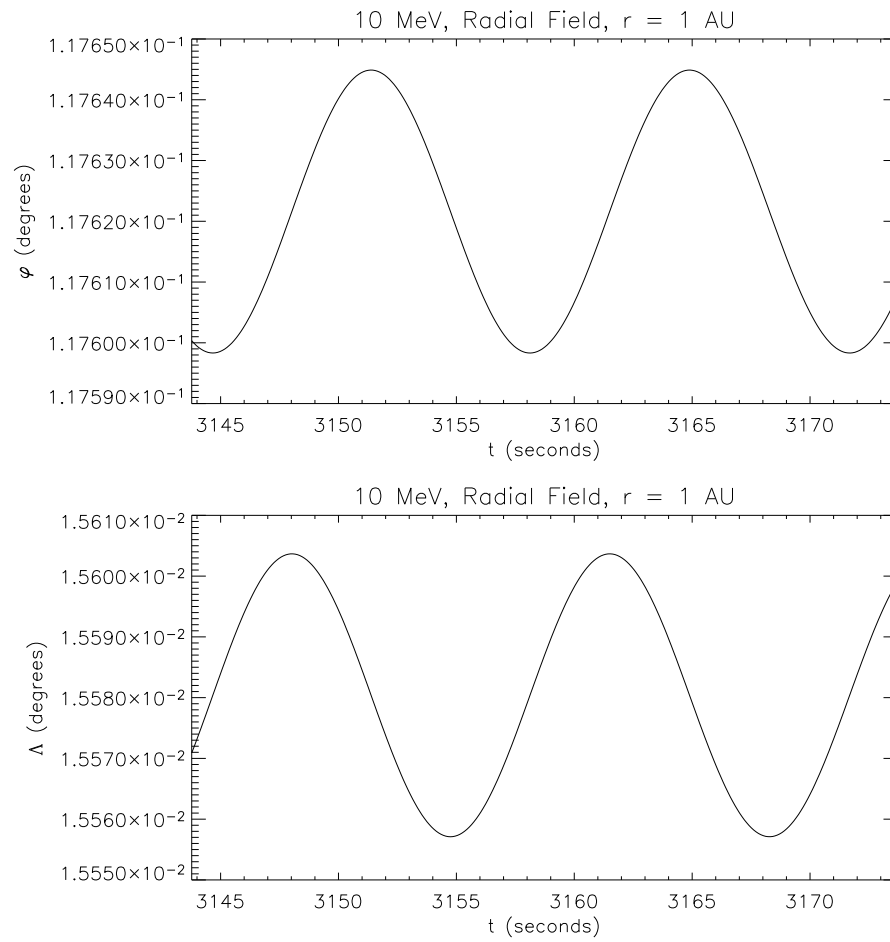


Figure 4.5: Upper panel shows  $\varphi$  versus time and lower panel shows  $\Lambda$  versus time from simulations of 10 MeV protons.

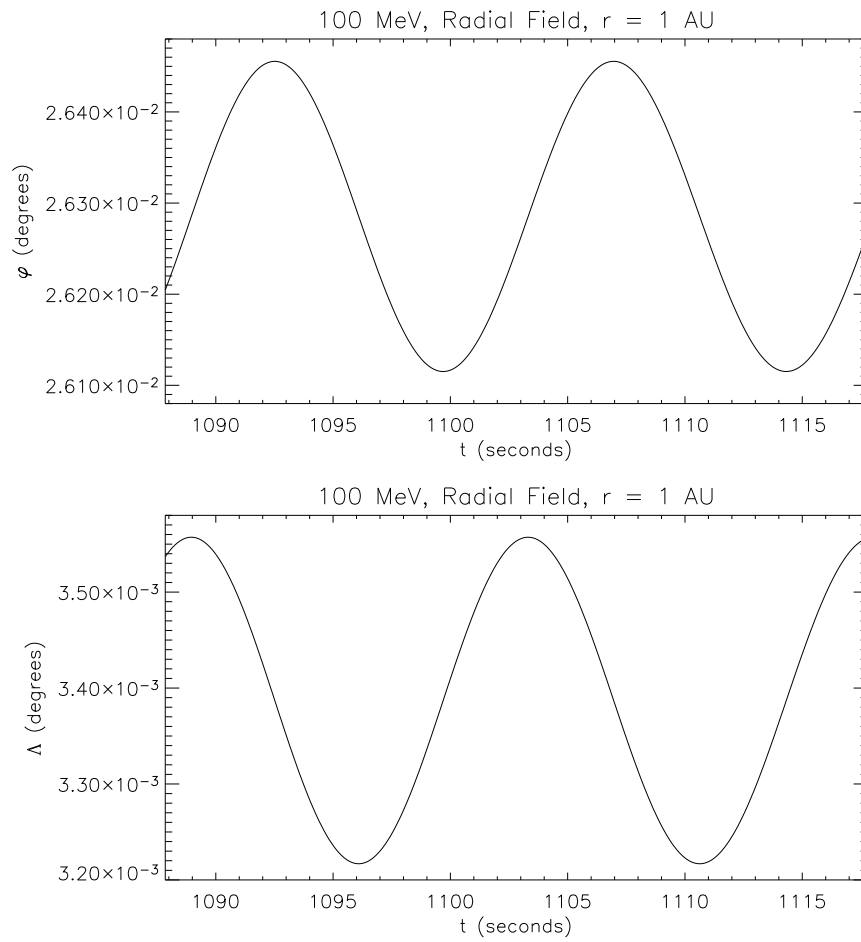


Figure 4.6: Upper panel shows  $\varphi$  versus time and lower panel shows  $\Lambda$  versus time from simulations of 100 MeV protons.

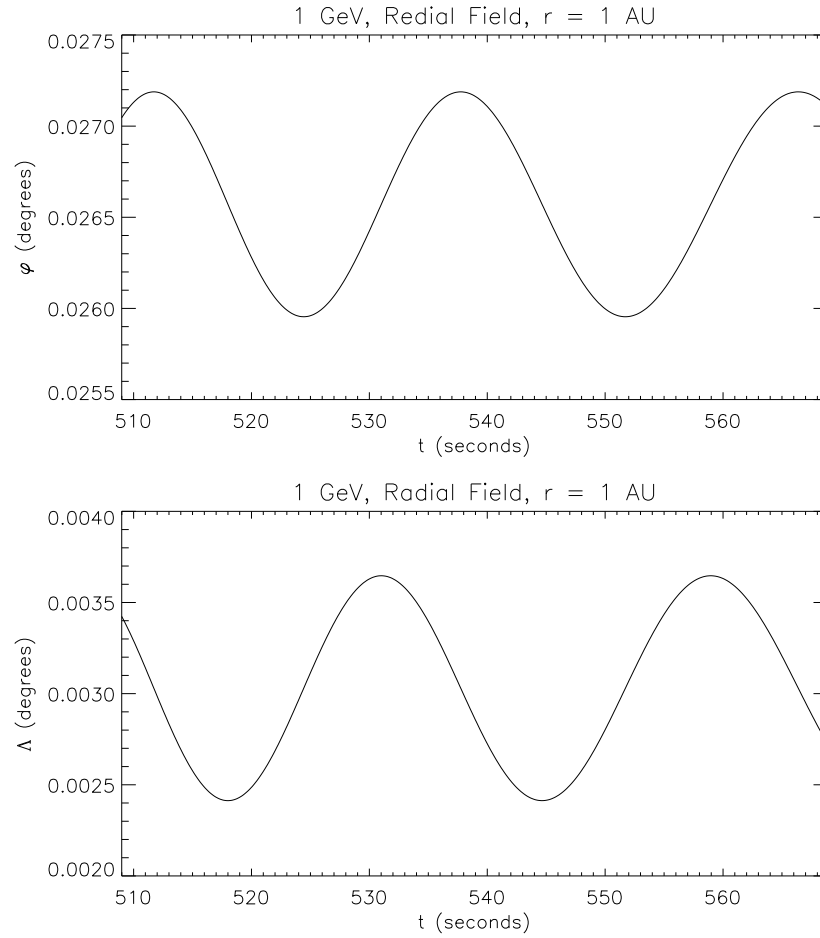


Figure 4.7: Upper panel shows  $\varphi$  versus time and lower panel shows  $\Lambda$  versus time from simulations of 1 GeV protons.

Table 4.1: Gyro-radius of protons at various energies for initial input and also for  $B = 5$  nT (at  $r = 1.0$  AU) from theory, simulations and from graphs.

Energy (MeV)	Pitch angle at 0.1 AU (rad)	Gyro-radius, at 0.1 AU (rad)	Gyro-radius, at 1.0 AU, simulations (rad)	Gyro-radius, at 1.0 AU, graphs (rad)
1	0.29383	$5.5939 \times 10^{-6}$	$5.5966 \times 10^{-6}$	$5.5932 \times 10^{-6}$
10	0.39025	$2.3301 \times 10^{-5}$	$2.3301 \times 10^{-5}$	$2.3281 \times 10^{-5}$
100	1.0337	$1.7034 \times 10^{-5}$	$1.7034 \times 10^{-4}$	$1.7022 \times 10^{-4}$
1000	0.95532	$6.1763 \times 10^{-4}$	$6.1763 \times 10^{-4}$	$6.1713 \times 10^{-4}$

Table 4.2: Gyro-frequency of protons at various energies for initial input and also for  $B = 5 \text{ nT}$  (at  $r = 1.0 \text{ AU}$ ) from theory, simulations and from graphs.

Energy (MeV)	Gyro-frequency, at 0.1 AU theory (rad/s)	Gyro-frequency, at 0.1 AU simulations (rad/s)	Gyro-frequency, at 1.0 AU theory (rad/s)	Gyro-frequency, at 1.0 AU, simulations (rad/s)	Gyro-frequency, at 1.0 AU, graphs (rad/s)
1	47.843	47.843	0.47843	0.47843	0.47695
10	47.389	47.389	0.47412	0.47389	0.47195
100	43.281	43.281	0.43281	0.43281	0.42887
1000	23.184	23.182	0.23184	0.23182	0.22998

### 4.3 Finding LTBs

LTBs are contours of constant potential  $a$  in the  $x$ - $y$  plane whose average 2D fluctuation energy is maximized with respect to neighboring contours, i.e.,

$$\text{Maximize : } |b^{2D}|_{av}^2 = \frac{1}{L} \oint |b^{2D}(x, y)|^2 d\ell, \quad (4.6)$$

where  $|b^{2D}|$  is the local strength of the 2D magnetic field,  $d\ell$  follows an equipotential contour, and  $L$  is the length of the contour. While any flux surface can cause topological trapping, LTBs possess a local maximum in  $|b^{2D}|_{av}^2$ , which is related to the suppression of slab diffusion, so they define flux surfaces that field lines cross with particular difficulty. As such, they are likely to coincide with sharp gradients in the density of field lines connected to the source, i.e., dropout features. LTBs were indeed found to play this role in simulations using random-phase 2D+slab magnetic fields (Chuychai *et al.* 2007). The present work examines whether they still serve as good indicators of dropout features when using more physically realistic 2D MHD fields, or whether intense field regions or current sheets provide better indicators.

We find LTBs by the following procedure. We begin with the results of the 2D MHD procedure for the magnetic potential  $a(x, y)$  at each  $1024 \times 1024$  grid points, and trace contours of constant potential. We consider square cells between grid points, and the cell boundaries are lines between neighboring grid points. Values of  $a$  are stepped upward or downward from zero with a constant spacing of 0.05 in units of  $B_0\lambda$ . For a given value of  $a$ , the tracing of equipotential contours uses linear interpolation along the cell boundary to find where contours exit and enter each 2D cell. For simplicity, contour segments within a cell are taken to be straight lines. When there are two entrance points and two exit points for the same cell, the pairing of entrance and exit points is based on the values of  $a$  at the four surrounding grid points, in a manner consistent with bilinear interpolation of  $a$  within the cell. Segments in adjacent cells are then linked to form closed contours. (When identifying the boundaries of the simulation region with periodic boundary conditions, there are no open contours.)

For each contour, the integration in equation (4.6) is approximated by summing over segments within cells, taking the integral along each segment to be represented by  $|b^{2D}|^2$  at the segment center times the segment length. We plot  $|b^{2D}|_{av}^2$  for each contour line, and visually compare these values between neighboring contours. Contours that have a maximal value compared with neighboring contours are identified as LTBs.

## CHAPTER V

### LOCAL TRAPPING BOUNDARIES IN A 2D MHD + SLAB FIELD

Observations of the interplanetary medium, and in particular the solar wind and magnetic fields evolving from their solar source, have revealed a complex spatial and temporal structure in plasma and magnetic properties. In addition to large-scale discontinuities such as corotating interaction regions, coronal mass ejections, and their associated shocks, as well as magnetic sector boundaries, there is also strong evidence for small-scale structure and filamentary connection to the Sun. Such evidence includes strong tails in statistical distributions of changes in magnetic field direction and plasma properties (e.g., Bruno *et al.* 2001; Borovsky 2008; Li 2008; Greco *et al.* 2009). In addition, particularly useful probes of magnetic connection are solar energetic particles (SEPs) from impulsive solar flares. Such flares occur as discrete events and inject particles from a small region of the solar surface (Reames *et al.* 1990), and SEPs of energies  $\lesssim 10$  MeV follow magnetic field lines quite closely, so the particles serve as excellent tracers of magnetic connection from a localized particle source at the Sun.

Previous computer simulations that traced turbulent magnetic field lines as described above have found sharp gradients in the density of field lines connected to the source as a function of  $x$  and  $y$  (Ruffolo *et al.* 2003; Zimbardo *et al.* 2004). The proposed physical mechanisms are (1) temporary topological trapping along flux surfaces of constant 2D potential  $a(x, y)$ , with eventual diffusive escape due to the slab fluctuations (Ruffolo *et al.* 2003), and (2) suppressed diffusive escape where the 2D field is strong (Chuychai *et al.* 2005). Combining the two ideas leads to the concept of local trapping boundaries (LTBs), i.e., 2D flux surfaces where the 2D field is particularly strong (Chuychai *et al.* 2007).



In the present work, we aim to rectify shortcomings in the turbulence models by using the output of 2D MHD simulation in place of 2D random-phase fields. With a 2D MHD model, microphysics of the plasma can be produced, i.e., current sheets and structures resembling flux tubes. Kittinaradorn *et al.* (2009) has used a 2D MHD + slab field with filamentary magnetic connection to explain “moss” emission in the solar transition region. Here, we examine the general properties of the 2D MHD field, in comparison with the random-phase field, and trace magnetic field lines in a 2D MHD + slab field in order to examine the expected dropout features of SEPs from impulsive solar flares. We find that dropout features, i.e., sharp changes in magnetic connection to a localized source, are frequently associated with LTBs, are sometimes associated with strong 2D magnetic fluctuations, and are only infrequently associated with current sheets. Thus a more realistic model of turbulent fluctuations can incorporate some attractive features of the flux tube view and is consistent with the lack of an observed association between dropouts and intense magnetic fields or currents.

### 5.1 Characteristics of the 2D MHD Field

Figure 5.1 shows an example of the effects of the 2D MHD procedure. Figure 5.1(a) shows contours of equal potential  $a(x, y)$  for a 2D random-phase field. When adding the mean field  $B_0\hat{\mathbf{z}}$ , the combined magnetic field twists along flux surfaces defined by the contours of constant  $a$ . This 2D random-phase field was used as the initial configuration for a 2D MHD procedure, and Figure 5.1(b) shows the equipotential contours for the resulting 2D MHD field. While the larger-scale turbulent features remain similar, the most obvious difference is that the random-phase contours are more irregular. These are smoothed in the 2D MHD field because irregularities in magnetic pressure are relieved by the fluid flow, tending to produce a smoother field magnitude  $|\mathbf{b}|$ . This is consistent with previous findings that MHD turbulence leads to the formation of many flux tubes, which relax locally at every stage of evolution while interacting with one another at their boundaries (Servidio *et al.* 2008). A related effect is that for this 2D MHD field, the

spacing between contours, which indicates  $|\mathbf{b}|$ , is more uniform in many places.

Nevertheless, some variations in  $b^2$  remain in the 2D MHD model, as shown in Figure 5.1(c). Note the tendency of regions with strong  $b^2$  to be somewhat aligned with the equipotential contours. This is not particular to the 2D MHD procedure, but is rather related to the solenoidal property  $\nabla \cdot \mathbf{b} = 0$ , or in Fourier space,  $\mathbf{k} \cdot \mathbf{b} = 0$ . Variations in the field are also indicated by the current  $\mathbf{j}$ . For the 2D MHD field, as discussed earlier, the current can be highly concentrated in narrow current cores and current sheets (Figure 5.1(d)). We will discuss these in more detail shortly. A comparison of the power spectra of the 2D random-phase and 2D MHD models is presented in Figure 5.2. Here we plot the omnidirectional power spectra,  $\mathcal{E}(k_\perp)$ , as estimated from  $|b_x^{2D}|^2 + |b_y^{2D}|^2$  summed over Fourier modes in all directions with  $k_\perp$  near the value of interest. Both spectra are normalized to the same energy  $\langle b^2 \rangle^{2D}$ , which is the integral of the power spectrum, and magnetic fields are expressed in units of  $B_0$ . By construction, the 2D random phase model has a power spectrum that rises with  $k_\perp$  in the energy-containing range (at low  $k_\perp$ ) and obeys the Kolmogorov law  $\mathcal{E} \propto k^{-5/3}$  in an inertial range at higher  $k_\perp$ . The rollover at and above  $k_\perp \approx 4000$  is an artifact of the limited extent of the FFT grid in some directions in  $\mathbf{k}$ -space. The 2D MHD spectrum is steeper at high  $k_\perp$  than the 2D random-phase spectrum. This occurs because during the 2D MHD procedure, the turbulent cascade proceeds faster for higher  $k_\perp$ . Since the 2D MHD simulation is run for a fixed time duration, only the high- $k_\perp$  portion of the spectrum is eroded by the turbulent cascade. Because of the overall normalization, the 2D MHD spectrum at low  $k_\perp$  becomes higher than the 2D random-phase spectrum. Figure 5.3 shows surface plots of various quantities for the 2D random-phase and 2D MHD models; the vertical scales are for magnetic fields in units of  $B_0$  and lengths in units of  $\lambda$ . In the 2D random-phase models, many wave modes are superimposed with appropriate amplitudes but random phases. This leads to random, irregular structures. It is seen that the magnetic potential,  $a(x, y)$ , is much smoother in the 2D MHD model, because of the tendency of magnetic

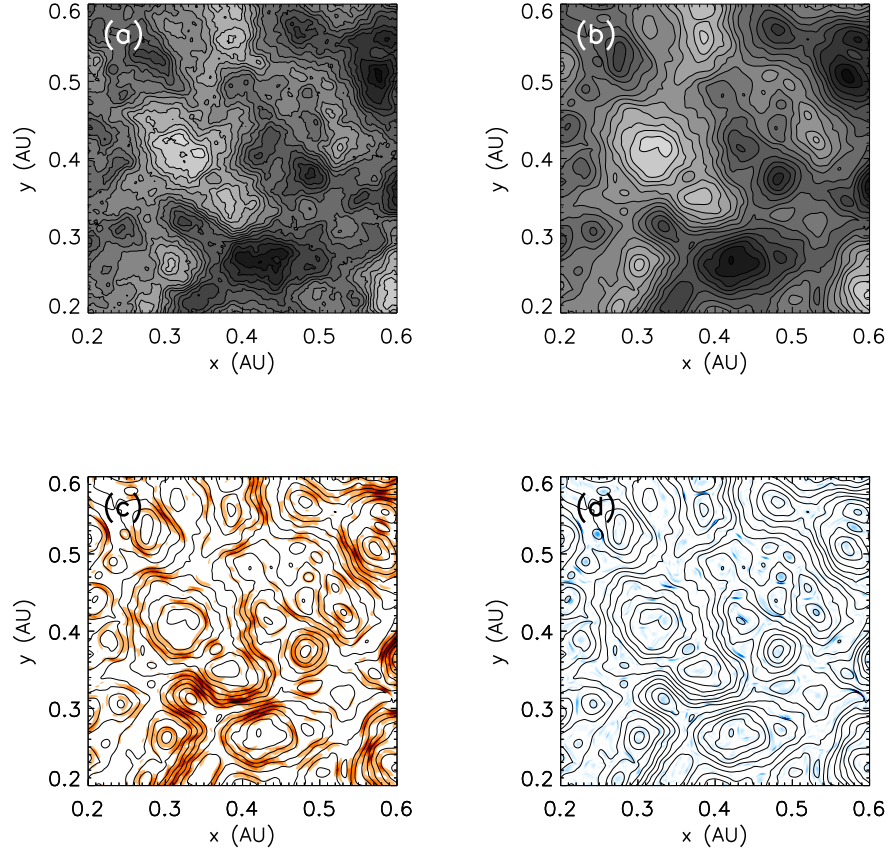


Figure 5.1: A 2D component of magnetic turbulence can be defined in terms of an irregular potential function  $a(x, y)$ , whose curl is  $\mathbf{b}^{2D}$ . We compare contours of constant potential, i.e., magnetic flux surfaces, for (a) a 2D random-phase field, in which  $a$  is a random function with a turbulent power spectrum, and (b) the same field after a 2D MHD procedure. A darker shading indicates a higher value of  $a$ . For the 2D MHD field, the contours of constant potential are superimposed with coloring to indicate (c)  $b^2$  and (d)  $j^2$ , for a current  $\mathbf{j} = \nabla \times \mathbf{b}$ . The 2D MHD field is a more physically realistic model, reproducing aspects of the flux tube viewpoint, but with the current concentrated in narrow current sheets. The present work examines the level of association between  $b^2$  or  $j^2$  and sharp changes in field line connection over a distance of 1 AU, which relates to dropouts (sharp density changes) in solar energetic particles as observed near Earth.

pressure to smooth variations in  $b^2$ . Similarly, the 2D MHD magnetic energy  $b^2$  is seen to typically vary less sharply (over longer distance scales) than the 2D random-phase magnetic energy.

Variations in the magnetic field can be expressed in terms of the current,  $\mathbf{j} = \nabla \times \mathbf{b}$ , which for the 2D fields is exactly along the  $z$ -direction, so we will simply

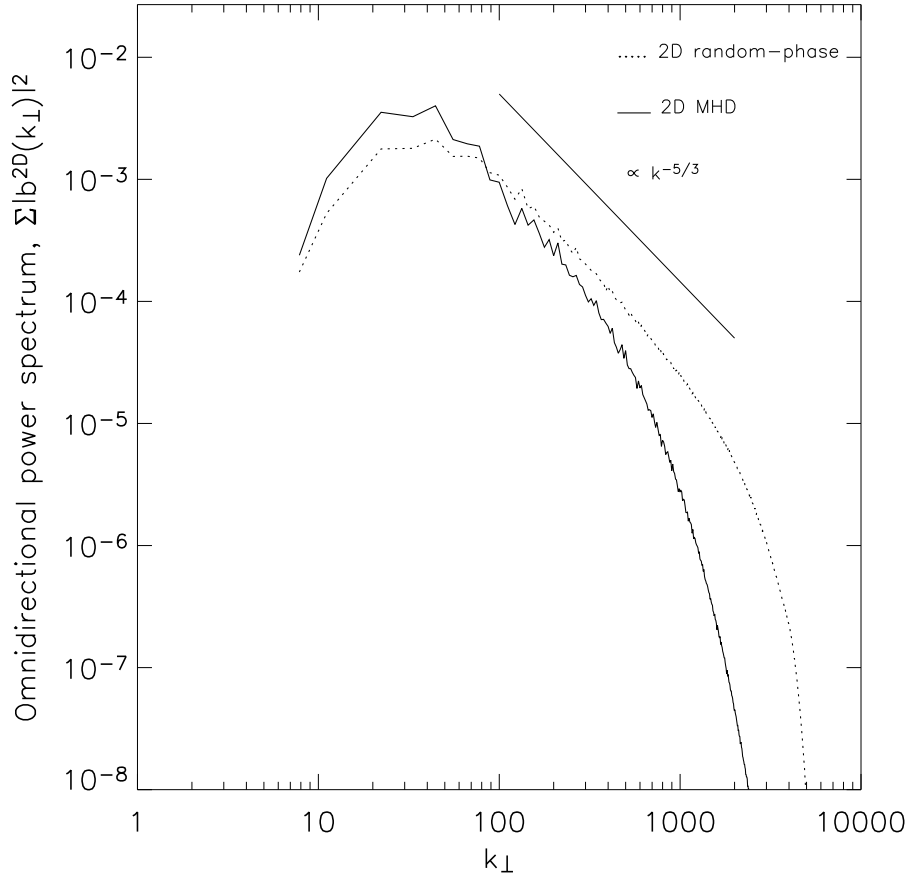


Figure 5.2: Omnidirectional power spectra of 2D random-phase and 2D MHD turbulent magnetic field models, normalized to the same total energy. After the fixed-time 2D MHD procedure, the high-wavenumber portion of the spectrum has been eroded by the turbulent cascade, which affects the overall normalization.

use  $j$  to refer to the  $z$ -component. The 2D MHD procedure follows the scalar magnetic potential  $a$  in Fourier space, and the current density is computed algebraically in  $\mathbf{k}$  space. For the 2D random-phase field we infer the current in the spatial domain by finite differencing, which we call  $j_{FD}$ .

For comparison purposes, Figures 5.3(e) and 5.3(f) show  $j_{FD}$  in real space, for both fields. In most locations, the current is greatly reduced in the 2D MHD model, because of the tendency to smooth variations in the field magnitude. This is related to rapid relaxation and suppression of nonlinearity (Servidio *et al.* 2008). However, inso-

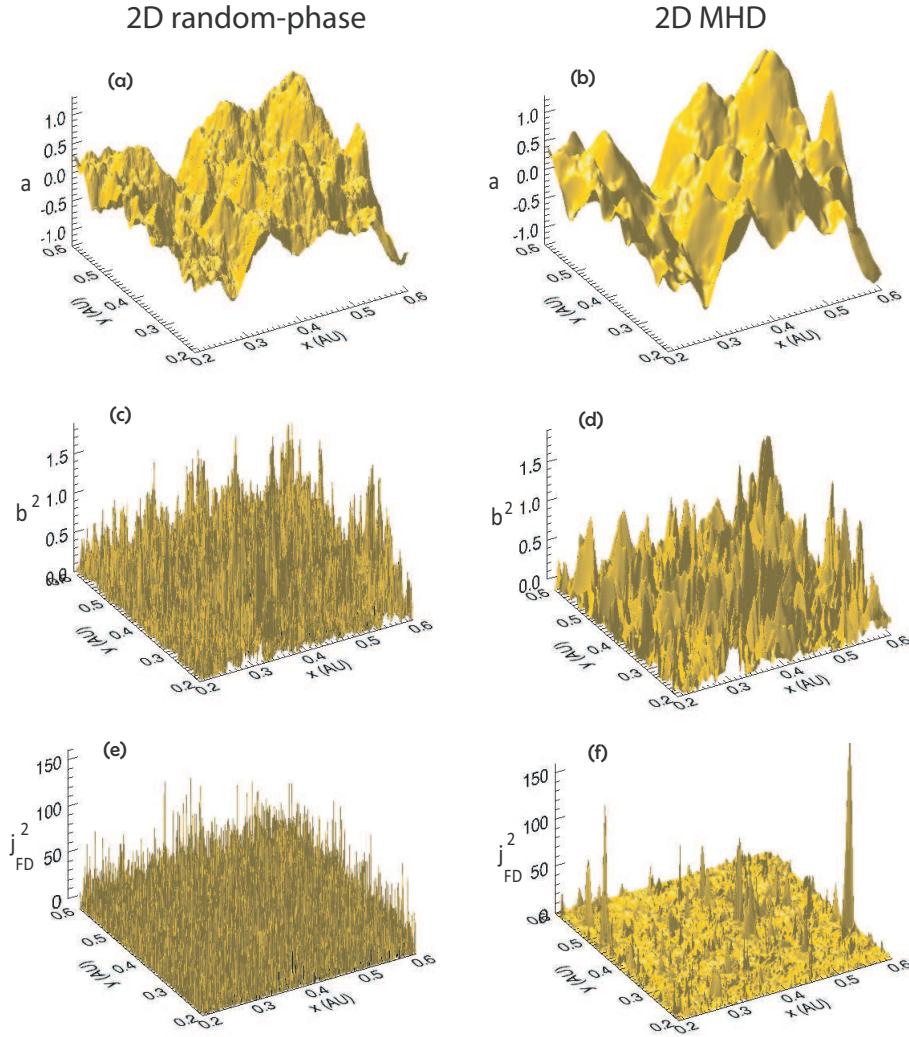


Figure 5.3: Comparison of quantities pertaining to two models of 2D magnetic turbulence, 2D random-phase (left panels) and 2D MHD (right panels): (a)-(b) Magnetic potential,  $a$ . (c)-(d) Magnetic energy,  $b^2$ . (e)-(f)  $j_{FD}^2$ , where the current  $\mathbf{j}_{2D}$  is determined from finite differencing of  $\mathbf{b}$ . In the more physical 2D MHD model,  $a$  is smoother,  $b$  varies more gradually, and  $j$  is concentrated in narrow current sheets.

far as the 2D MHD procedure is not continued long enough for all magnetic fields to reconnect and change topology completely, strong persistent current features are generated associated with islands and at certain topological defects. These can be identified as current cores or current sheets (see Figure 2 of Kittinaradorn et al. 2009; see also Greco et al. 2009). Current cores are found at O-points, i.e., maxima or minima in the potential, where the magnetic field goes to zero; this is a topological defect where the

magnetic pressure  $b^2$  cannot be uniform. In the flux tube view, current cores are at the centers of flux tubes. Current sheets are typically found at X-points, i.e., saddle points in the potential, where the field again goes to zero. In particular, when two regions of plasma with oppositely directed magnetic fields flow toward each other, the magnetic field lines can reconnect in a thin boundary region (Sweet 1958; Parker 1963a; Petschek 1964). Such sharp, localized changes in  $\mathbf{b}$  correspond to the strongest currents in the 2D MHD model, dominating the visual features in Figures 5.1(d) and 5.3(f).

Note that a view of distinct, independent flux tubes with sharp boundaries would seem to require a sharp change in  $\mathbf{b}$  and a strong current  $j$  all around the flux tube boundaries. However, in our 2D MHD results, the current sheets are found to be quite localized, encompassing only a small fraction of a flux surface (see Figure 5.1(d)), which is physically reasonable given the attraction of parallel current structures. This is also a feature of modern models and simulations of magnetic reconnection (Priest *et al.* 2000). In the 2D MHD model, one could say that neighboring flux tube structures are coordinated to arrange a concentration of current in current sheets of limited extent, which to some extent contradicts the view of independent flux tubes with sharp boundaries. Furthermore, if the boundary of a “flux tube” is defined as a flux surface that includes a current sheet, one can have concentric flux tube boundaries, and boundaries that along most of their surface have no sharp field gradients.

The results shown in Figure 5.3 are consistent with the scenario described by Matthaeus & Montgomery (1980). 2D MHD exhibits a dual cascade of magnetic excitation to larger scales (lower wavenumbers) and current density to smaller-scale, coherent structures (at higher wavenumbers). Such phase coherence of Fourier modes cannot be obtained in random-phase models.

It is interesting to quantitatively confirm that the 2D random-phase and 2D MHD models have different statistical distributions of quantities related to the magnetic field. For the simulated distributions of magnetic potential, magnetic field, and current,

Table 5.1: Moments of various quantities for magnetic field models

Model	Quantity	4 <sup>th</sup> moment <sup>a</sup>	6 <sup>th</sup> moment <sup>b</sup>
Slab random-phase	$b_x$	3.02	15.43
	$b_y$	2.95	14.36
2D random-phase	$a$	3.04	14.51
	$b_x$	3.06	15.94
	$b_y$	2.93	13.98
	$j_{FD}^c$	3.01	15.18
2D MHD	$a$	3.04	14.50
	$b_x$	<i>2.76</i>	<i>12.37</i>
	$b_y$	<i>2.67</i>	<i>11.02</i>
	$j_{FD}^c$	<i>7.65</i>	<i>331.28</i>
	$j$	<i>6.80</i>	<i>242.05</i>

<sup>a</sup>Normalized to second moment squared, e.g.,  $\langle b_x^4 \rangle / (\langle b_x^2 \rangle)^2$ . The value would be 3 for a Gaussian distribution. Italics indicate values significantly different from 3.

<sup>b</sup>Normalized to second moment cubed, e.g.,  $\langle b_x^6 \rangle / (\langle b_x^2 \rangle)^3$ . The value would be 15 for a Gaussian distribution. Italics indicate values significantly different from 15.

<sup>c</sup>FD indicates finite differencing.

we have determined the fourth moment (kurtosis) and, as a check, the sixth moment as well (Table 5.1). The fourth moment is divided by the variance squared to yield a dimensionless quantity, which would be 3 for a Gaussian distribution. Similarly, the sixth moment is divided by the variance cubed, which would be 15 for a Gaussian distribution. For a distribution with weaker tails than a Gaussian, the normalized fourth and sixth moments would be lower than 3 and 15, respectively, and for a distribution with stronger tails they would be higher. The uncertainty of our determination can be estimated by comparing values for  $b_x$  and  $b_y$  for all models. These should be the same because the models are axisymmetric. From these we estimate uncertainties of about 0.08 and 1.19 for the fourth and sixth moments, respectively. In Table 5.1, for the slab and 2D random-phase fields, all the quantities have fourth and sixth moments that are consistent with Gaussian values. This is perhaps not surprising because random-phase quantities represent the superposition of a large number of independent Fourier modes, so the resulting quantity should have a Gaussian distribution by the central limit theorem. On the other hand, some quantities in the 2D MHD model are significantly different

from Gaussian values. The distribution of potential values is still consistent with a Gaussian distribution, perhaps because the main effect of the 2D MHD procedure on  $a$  is to smooth small-scale irregularities. However, the magnetic fields have fourth and sixth moments that are significantly lower than Gaussian values, apparently due to the physical process that the magnetic pressure becomes more uniform on small scales. The currents are the most non-Gaussian. There is a reduction of the current in most places but strong concentration in current sheets leads to strongly enhanced non-Gaussian tails in the distribution (see also Wan *et al.* 2009). While the current  $j$  derived from Fourier modes has lower moments than that derived from finite differencing of the field, both have moments that are much higher than Gaussian values. The non-Gaussian 2D MHD distributions of  $b_x$ ,  $b_y$ , and  $j$  arise from MHD and can be understood physically, so these are taken to be more physically reasonable than the Gaussian distributions of random-phase fields.

Here we have characterized the physically attractive features of the 2D MHD model, and in particular how it incorporates elements of the flux tube view. Next, we review the mechanisms that have been identified as underlying dropout features, and consider whether the physically realistic features of 2D MHD simulations should actually affect to those mechanisms.

## 5.2 Reasons for Dropout Features

If one accepts that SEP dropout features are associated with the filamentation of magnetic connection to the particle source (Mazur *et al.* 2000; Giacalone *et al.* 2000), then the next question is why such filamentation occurs with sharp boundaries, given that field line diffusion over 1 AU is expected to lead to a substantial spread in magnetic connection (Ruffolo *et al.* 2003, 2004).

One specific mechanism, developed in the context of the 2D+slab magnetic field model, is topological trapping of field lines along flux surfaces of constant 2D potential  $a(x, y)$ , with eventual diffusive escape due to the slab fluctuations (Ruffolo *et al.*



2003). In essence the mean field and 2D field are viewed as the main determinants of field line motion, along such 2D flux surfaces, with slab fluctuations as a perturbation; this approach is justified by the minor (15 to 20%) contribution of slab fluctuations to the total fluctuation energy (Beiber *et al.* 1994; Bieber *et al.* 1996).

An additional mechanism is the suppression of diffusive escape when the 2D field is strong or irregular (Chuychai *et al.* 2005, 2007). This mechanism has also been demonstrated for particle orbits (Tooprakai *et al.* 2007). However, the demonstrations of both mechanisms for turbulent fields have so far employed random-phase simulations.

While it is clearly more realistic to use 2D MHD fields in place of 2D random-phase fields, it is not clear whether this will actually influence the mechanisms for dropout features. In the flux tube view, it has been proposed that field lines are confined within small-scale flux tubes (Borovsky 2008) (which is indeed largely the case for large-scale flux ropes, e.g., in magnetic clouds). However, in our 2D MHD simulation results, flux tube-like structures are found to have weak variations in magnetic fields across most of their “boundaries.” Topological trapping applies to any flux surface, and it is not clear that flux surfaces that contain current sheets over narrow portions should trap field lines more effectively.

According to Chuychai *et al.* (2007), the flux surfaces that trap field lines most effectively are those with high 2D magnetic energy, a key factor in the suppression of slab diffusive escape, i.e., the LTBs. (The other key factor, the irregularity of the 2D equipotential contour, is not considered in the definition of LTBs, and is indeed less important when using a 2D MHD model where such irregularity is greatly reduced; see Figure 5.1.) The LTBs are not necessarily found at boundaries of flux tube-like structures. While it is physically more realistic to use a 2D MHD model that allows for current sheets, it is not clear that the current sheets should play a major role in field line trapping, as has been expected in the flux tube view (see also Chollet & Giacalone 2008).

### 5.3 Associations with Dropout Features

The observed lack of a strong association between magnetic field changes (such as current sheets) and dropout features has been expressed as a criticism of explanations of dropouts in terms of turbulence (Chollet & Giacalone 2008), though it actually poses more of a challenge to the flux tube viewpoint. Previous turbulence models expected dropout features to occur along LTBs, which encapsulate the two identified mechanisms for field line trapping, but those models did not allow for strong current sheets are not able to directly address such observations. We note that Mazur *et al.* (2000) reported a general lack of an association with magnetic or plasma signatures. This can be taken to rule out a strong association between the magnetic field intensity and dropout features, and in the present work we examine whether turbulence models predict such an association. Our simulation results for a 2D MHD model, which does allow for current sheets, are shown in Figure 5.4. Given the mean magnetic field along  $\hat{z}$  and two-component 2D+slab magnetic turbulence, we have traced 10,000 magnetic field lines from initial locations within a circle of radius 0.1 AU. The scatter plots in Figure 5.4 show  $(x, y)$  locations of the same field lines after tracing them for a distance  $z$  of 1.0 AU. We also traced trajectories for protons of various energies. Up to  $\sim 1$  GeV, the maps of where particle and field line trajectories intersect  $z = 1$  AU are very similar as shown in Figure 5.5. (Note that observations of dropouts have typically been for particles below  $\sim 1$  MeV/nucleon.) Thus we conclude that the locus of field line trajectories is a good proxy for where the SEPs will travel on their way out from the source. The sharp gradients in the density of points in Figure 5.4 are locations where a spacecraft traversed by solar wind with such a magnetic structure would observe dropouts. In Figure 5.4(a), the scatter plot of field line locations is superimposed with contours of equal potential  $a(x, y)$  as in Figure 5.1(b), for a regular spacing in  $a$ . It is clear that the boundaries of field line connectivity are related to the equipotential contours, i.e., 2D flux surfaces. This is evidence for topological trapping (Ruffolo *et al.* 2003). Though “islands” or flux

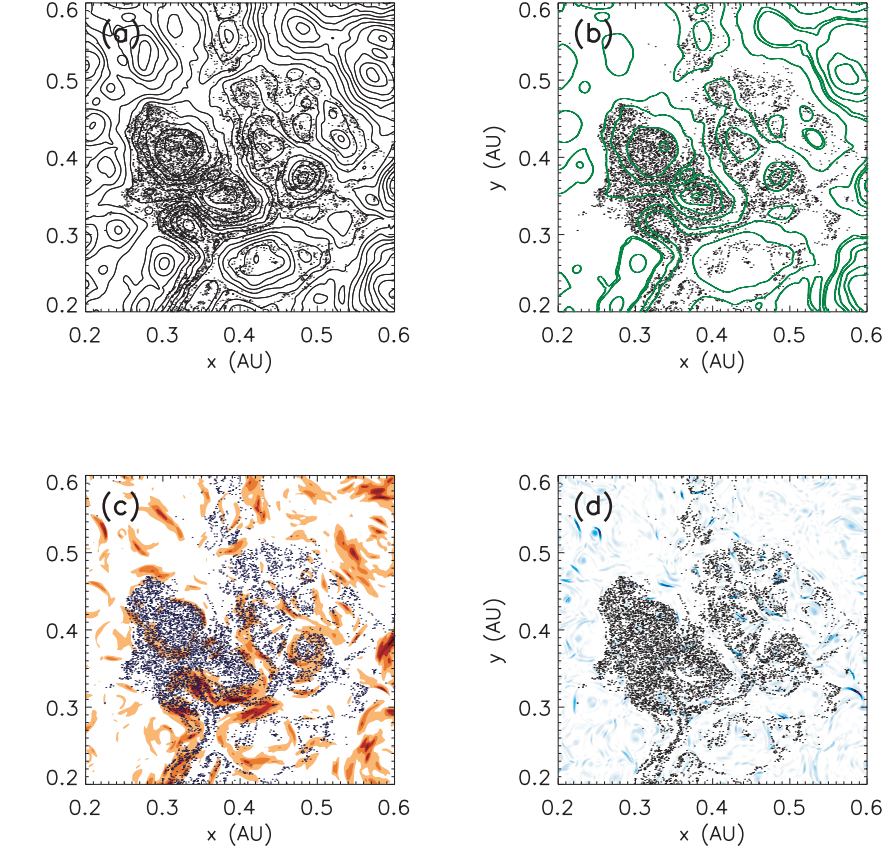


Figure 5.4: For a mean magnetic field along  $\hat{z}$  and two-component magnetic turbulence, we trace 10,000 magnetic field lines from initial locations within a circle of radius 0.1 AU. These scatter plots show  $(x, y)$  locations of field lines after a distance  $z$  of 1.0 AU, superimposed with indications of (a) contours of constant potential  $a(x, y)$  at equal intervals  $\Delta a$  (b) local trapping boundaries (LTBs; contours) (green), (c)  $b^2$  (red), and (d)  $j^2$  (blue). Sharp gradients in magnetic connection to the source, i.e., dropout features, are seen to be associated frequently with LTBs, sometimes with large  $b^2$ , and infrequently with current sheets.

tube-like structures are clearly seen, from this plot alone, it is not clear what determines the location of dropout features. In several locations, they are clearly not associated with the visual “boundary” of a flux rope [e.g., at the coordinates (0.34,0.43), (0.40,0.50), and (0.47,0.39)].

Figure 5.4(b) superimposes the scatter plot with LTBs, particular flux surfaces where  $|b^{2D}|_{av}^2$  has a maximum for the 2D component (see Eq. [4.6]). In numerous locations (including the specific locations mentioned above), the LTBs correctly identify which flux surfaces serve as boundaries in field line connectivity. Physically, these flux

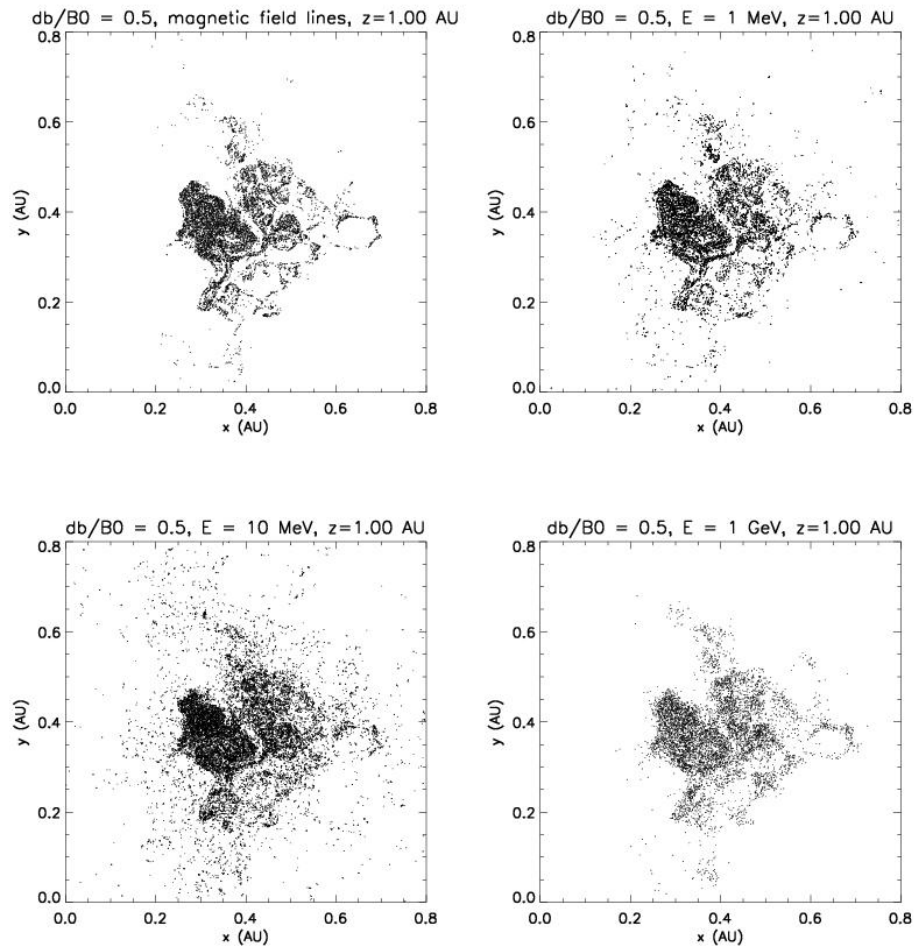


Figure 5.5: Scatter plots of magnetic field lines and particle trajectories in 2D MHD+slab turbulence at  $z = 1.0$  AU.

surfaces are particularly difficult for field lines to penetrate because of the suppression of slab diffusion across contours where the 2D field is strong (Chuychai *et al.* 2005, 2007). In many cases, field lines from the initial source region remain present (or absent) on both sides of an LTB, so not all locations along LTBs are associated with dropouts. Likewise, not all sharp boundaries in field line connectivity are associated with LTBs (they can also be associated with the boundary of the initial source region, as deformed by the mapping to 1 AU), but on the whole there is a reasonably good association.

Note that LTBs are often concentric, and thus do not serve as proper boundaries of islands or flux tubes. They are quite specific to field line connectivity and related

phenomena such as dropouts. They are not space-filling, in the sense that some field lines can travel out from the injection region without having to cross an LTB. This is an important requirement for consistency with the high rate of diffusion observed over long time scales (Kaghashvili *et al.* 2006).

We also examine whether the simulation results indicate an association with strong turbulent magnetic fields. Such an association has not been obvious in observations (Mazur *et al.* 2000). Here we specifically examine an association with  $|b^{2D}|^2$  (Figure 5.4(c)). In the simulation results, there is a degree of association, notably near the coordinates (0.34,0.43), but it is substantially weaker than the association with LTBs. The reason is that topological trapping naturally occurs along an entire flux surface, whereas only some portions of an LTB have high 2D fields. In spacecraft observations, variations in the 2D field strength are not readily isolated from other magnetic field fluctuations. Thus a moderate degree of association between dropout features and  $|b^{2D}|^2$  may be difficult to observe in the interplanetary medium, where there are independently varying slab fluctuations, and the mean field itself varies over large scales.

Finally, Figure 5.4(d) shows that dropout features are typically not associated with the current sheets in this model. Thus the observed lack of association between dropouts and current sheets or sharp magnetic field changes should not be construed as in conflict with turbulence models.

It is perhaps vexing that the physical mechanisms for field line trapping result in a better association with LTBs, which are mathematical constructs and difficult to identify in magnetic field observations along a one-dimensional spacecraft trajectory, than with current sheets, which are relatively easy to identify. However, nature is not obliged to provide easy diagnostics.

## CHAPTER VI

# COLLIMATION OF PARTICLE TRAJECTORIES IN SPHERICAL GEOMETRY

In this chapter, we report on our results from tracing particle trajectories in spherical geometry. We first simulated protons of low energy, and then of higher energy. We found that for low energy particles, we can observe the dropout phenomenon as in Cartesian geometry. For higher energy particles, we found something interesting, the “collimation effect.” We perform computer simulations to confirm the theory of collimation in 3 cases: particles of 10 GeV moving in a single 2D island, particles of 10 GeV moving in pure 2D turbulence, and finally magnetic field lines and particles of various energies moving in 2D MHD + slab turbulence.

### 6.1 Low-Energy Particle Trajectories and Dropouts

In this section, we perform computer simulations tracing particle trajectories of 1 MeV, 10 MeV and 1 GeV. The results are shown in Figure 6.8. For comparison, we also trace magnetic field lines. Both particles and magnetic field lines were initially uniformly distributed in a circle of radius 10 degrees. All particles began at  $r_0 = 0.05$  AU as measured from the center of the Sun. The ratio of the root-mean-squared fluctuating field  $b$  to  $B_0$  was 0.5.

From the results, we can conclude that SEPs of energy less than 1 GeV follow field lines very closely, so “dropout” patterns can be modeled by field line tracing just as well as particle tracing.

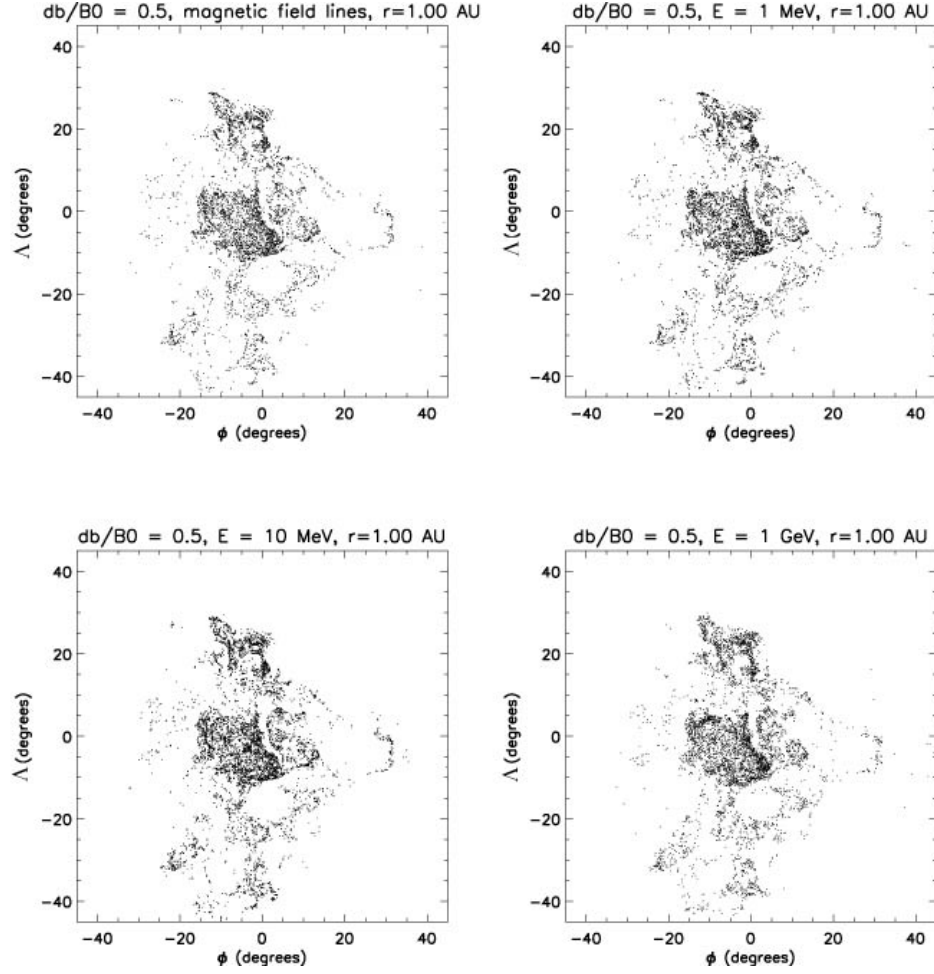


Figure 6.1: Scatter plots of magnetic field trajectories and proton trajectories for various energies at 1 AU. The upper left panel is a scatter plot of magnetic field lines. The upper right panel is for 1 MeV protons. The bottom left panel is for 10 MeV protons and the bottom right panel is for 1 GeV protons.

## 6.2 Collimation of Particle Beams in a Gaussian Flux Rope

### 6.2.1 Simulations

We demonstrate the collimation effect by performing computer simulations for a simple case, i.e., a charged particle moving in a Gaussian flux rope. In this scenario, a positive potential function can be written in the form:

$$a = \frac{r_1}{r} A_0 \exp\left(-\frac{1 - \cos \Delta}{\sigma^2}\right), \quad (6.1)$$

where  $\Delta$  is the angular distance which can be written in general as

$$\cos \Delta = \cos(\varphi - \varphi_0) \cos \Lambda \cos \Lambda_0 + \sin \Lambda \sin \Lambda_0. \quad (6.2)$$

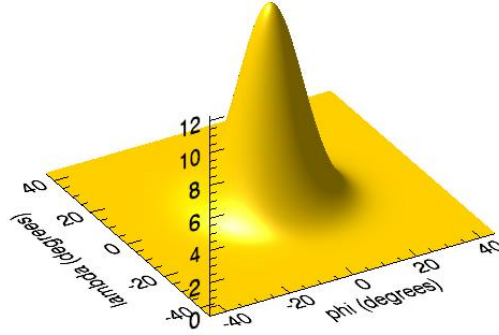


Figure 6.2: Surface plot of a positive 2D Gaussian potential function.

Note that the vector potential is  $\mathbf{a} = a\hat{r}$ . In our case  $\varphi_0 = \Lambda_0 = 0$ , hence eq. (6.2) becomes

$$\cos \Delta = \cos \varphi \cos \Lambda. \quad (6.3)$$

Taking the curl of eq. (6.1), we will get the magnetic field

$$b_\varphi^{2D} = -\frac{r_1 A_0 \cos \varphi \sin \Lambda}{r^2 \sigma^2} \exp\left(-\frac{1 - \cos \Delta}{\sigma^2}\right) \quad (6.4)$$

$$b_\Lambda^{2D} = \frac{r_1 A_0 \sin \varphi}{r^2 \sigma^2} \exp\left(-\frac{1 - \cos \Delta}{\sigma^2}\right). \quad (6.5)$$

Now consider  $(b^{2D})^2$ ,

$$\begin{aligned} (b^{2D})^2 &= \left[ \frac{r_1 A_0}{r^2 \sigma^2} \exp\left(-\frac{1 - \cos \Delta}{\sigma^2}\right) \right]^2 (\sin^2 \varphi + \cos^2 \varphi \sin^2 \Lambda) \\ &= \left[ \frac{r_1 A_0}{r^2 \sigma^2} \exp\left(-\frac{1 - \cos \Delta}{\sigma^2}\right) \right]^2 [(1 - \cos^2 \varphi) + \cos^2 \varphi (1 - \cos^2 \Lambda)] \\ &= \left[ \frac{r_1 A_0}{r^2 \sigma^2} \exp\left(-\frac{1 - \cos \Delta}{\sigma^2}\right) \right]^2 (1 - \cos^2 \varphi \cos^2 \Lambda) \\ &= \left[ \frac{r_1 A_0}{r^2 \sigma^2} \exp\left(-\frac{1 - \cos \Delta}{\sigma^2}\right) \right]^2 (1 - \cos^2 \Delta), \end{aligned} \quad (6.6)$$



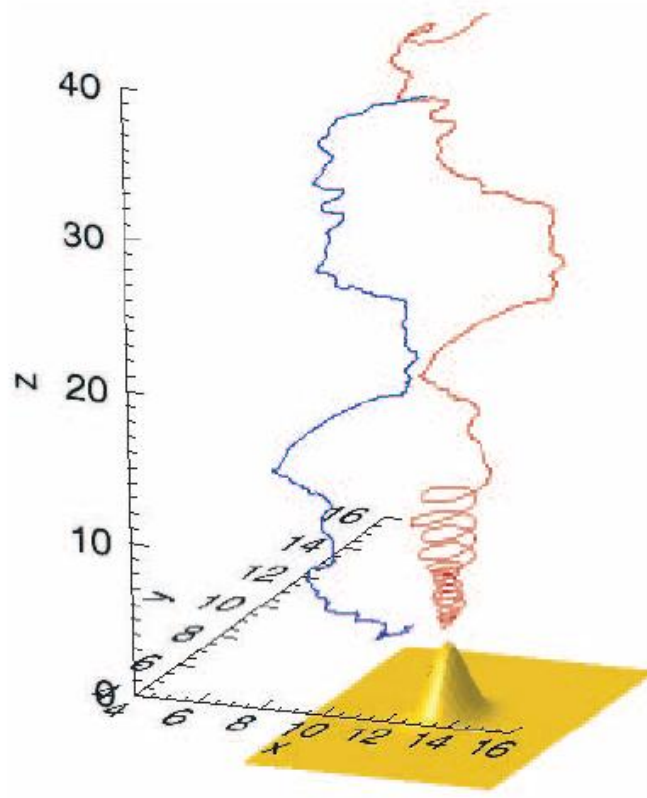


Figure 6.3: Field line trapping in a positive 2D Gaussian magnetic island + slab turbulence. [Image Credit: Chuychai et al. 2007]

hence

$$b^{2D} = \frac{r_1 A_0 \sin \Delta}{r^2 \sigma^2} \exp\left(-\frac{1 - \cos \Delta}{\sigma^2}\right), \quad (6.7)$$

We can find  $b_{max}^{2D}$  from eq. (6.7):

$$\left. \frac{db^{2D}}{d\Delta} \right|_{\Delta_{max}} = 0 = \cos \Delta_{max} \exp\left(\frac{\cos \Delta_{max} - 1}{\sigma^2}\right) - \frac{\sin^2 \Delta_{max}}{\sigma^2} \exp\left(\frac{\cos \Delta_{max} - 1}{\sigma^2}\right) \quad (6.8)$$

then

$$\begin{aligned} \sin^2 \Delta_{max} &= \sigma^2 \cos \Delta_{max} \\ 1 - \cos^2 \Delta_{max} &= \sigma^2 \cos \Delta_{max} \\ \cos^2 \Delta_{max} + \sigma^2 \cos \Delta_{max} - 1 &= 0. \end{aligned} \quad (6.9)$$

Therefore

$$b_{max}^{2D} = \frac{r_1 A_0}{r^2 \sigma} \sqrt{\cos \Delta_{max}} \exp\left(-\frac{1 - \cos \Delta_{max}}{\sigma^2}\right). \quad (6.10)$$

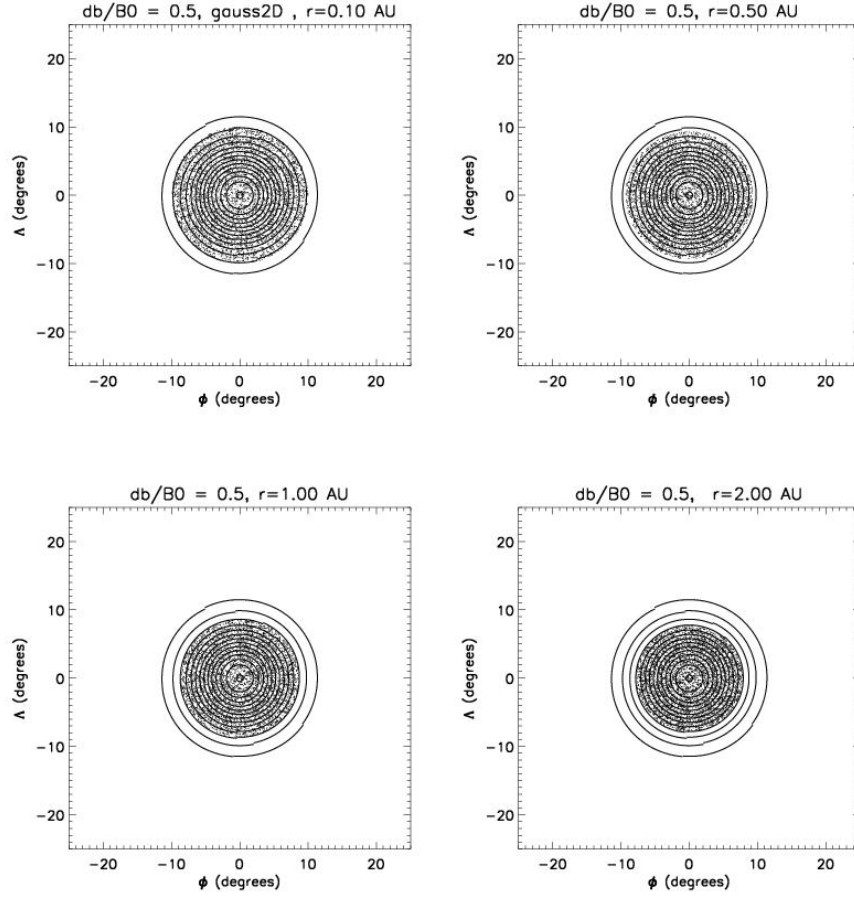


Figure 6.4: Scatter plots of 10 GeV proton trajectories at various distances in a positive 2D Gaussian island. The upper left panel shows initial positions of particles at  $r = 0.1$  AU. The next panel is for particles at  $r = 0.5$  AU. The bottom left panel is for particles at  $r = 1.0$  AU and the last panel is for particles at  $r = 2.0$  AU.

Equation (6.9) has two roots:

$$\cos \Delta_{max} = -\frac{\sigma^2}{2} \pm \sqrt{1 + \frac{\sigma^4}{4}}. \quad (6.11)$$

We choose the positive root because  $\cos \Delta$  has values between -1 and 1 and the negative root is outside that range. Then we find  $A_0$  by our choice of normalization of  $b_{max}^{2D}$ ,

$$b_{max}^{2D} = 0.5B_r, \quad (6.12)$$

where

$$B_r = \frac{B_0 r_1^2}{r^2}. \quad (6.13)$$

Then

$$A_0 = 0.5 \frac{\sigma}{\sqrt{\cos \Delta_{max}}} \frac{B_0 r^2}{r_1} \exp\left(\frac{1 - \cos \Delta_{max}}{\sigma^2}\right). \quad (6.14)$$

In the simulations, we use  $\sigma = 5$  degrees and  $r_1 = 1.0$  AU. We simulated 5,000 protons of energy 10 GeV. The particles were initially uniformly distributed in a circle of radius 10 degrees. The results are shown in Figure 6.4. From the Figure, it is seen that these positively charged particles are drawn toward the high potential region. This effect depends on the strength of the magnetic field and energy of particles. We find that for lower energy particles, the effect is weaker.

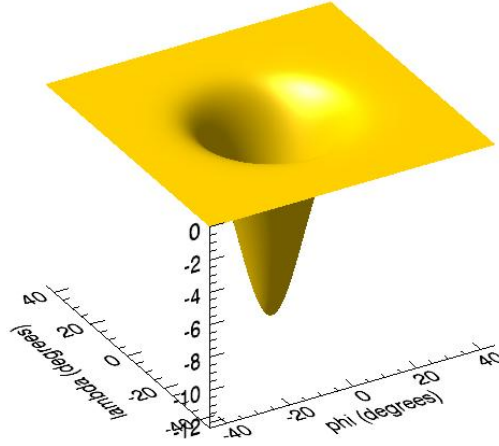


Figure 6.5: Surface plot of a negative 2D Gaussian potential function.

We also examine another extreme case, e.g., for a low potential function with  $A_0 \rightarrow -A_0$ . The magnetic field of this case is:

$$b_\varphi^{2D} = \frac{r_1 A_0 \cos \varphi \sin \Lambda}{r^2 \sigma^2} \exp\left(-\frac{1 - \cos \Delta}{\sigma^2}\right) \quad (6.15)$$

$$b_\Lambda^{2D} = -\frac{r_1 A_0 \sin \varphi}{r^2 \sigma^2} \exp\left(-\frac{1 - \cos \Delta}{\sigma^2}\right). \quad (6.16)$$

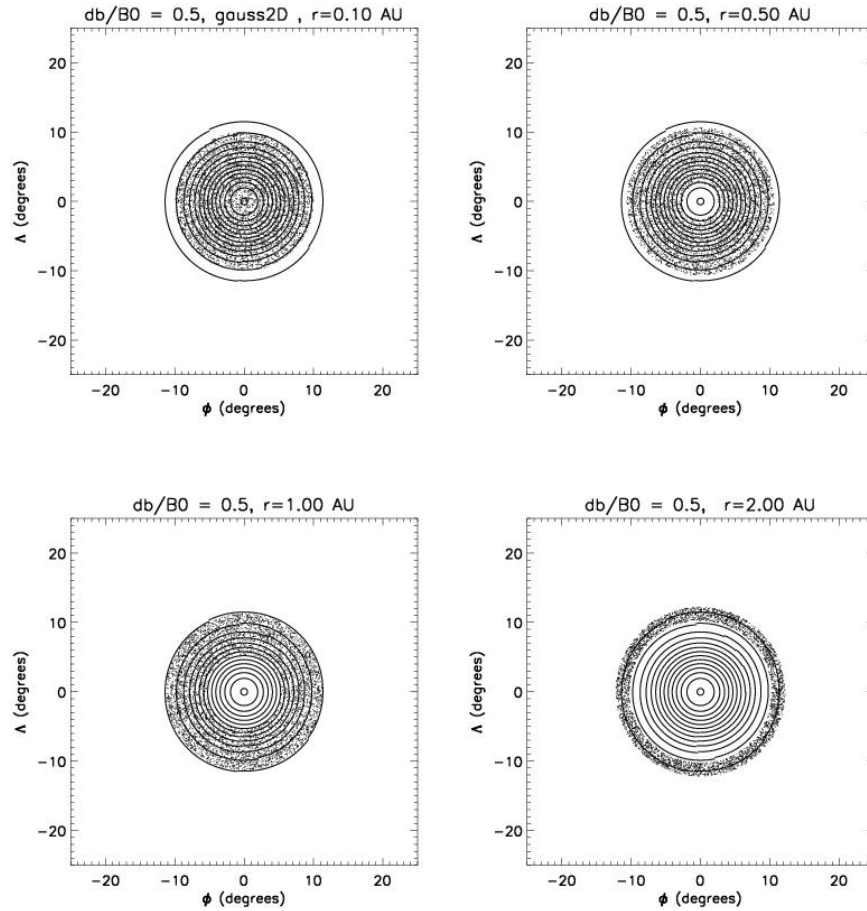


Figure 6.6: Scatter plots of 10 GeV proton trajectories at various distances in a negative 2D Gaussian island. The upper left panel shows initial positions of particles at  $r = 0.1$  AU. The next panel is for particles at  $r = 0.5$  AU. The bottom left panel is for particles at  $r = 1.0$  AU and the last panel is for particles at  $r = 2.0$  AU.

We also use the same initial condition as in the previous simulation. The results are shown in Figure 6.6. These positive particles move away from the low potential.

### 6.2.2 Theory

There are two main physical reasons for the attraction of positive particles to high-potential O-points: the curvature drift and gradient drift. Let us consider the

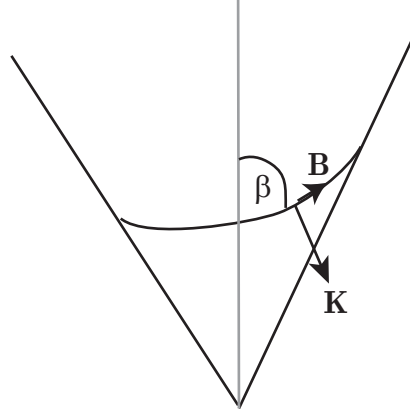


Figure 6.7: Definitions of  $\mathbf{K}$  and  $\beta$  for a conical flux rope.

curvature drift first. The curvature of a curve can be defined by

$$\mathbf{K} = \frac{\mathbf{R}_c}{R_c^2}, \quad (6.17)$$

where  $R_c$  is the radius of curvature and  $\mathbf{R}_c$  points from the center of curvature to the point of interest. The curvature drift is given by (Krittinatham 2009)

$$\mathbf{v}_c = \frac{mv_{\parallel}^2}{qB^2} \frac{\mathbf{R}_c \times \mathbf{B}}{R_c^2} = \frac{mv_{\parallel}^2}{qB^2} \mathbf{K} \times \mathbf{B}. \quad (6.18)$$

Let us further envision a particle moving with speed  $v_{\parallel}$  along  $\hat{B}$ , using the guiding center approximation.

Let us model a conical “flux rope” or “island” of the 2D topology. For convenience, let us define a spherical coordinate system so the polar axis passes through the O-point. Let us also assume azimuthal symmetry, so there is no dependence on  $\varphi$ . Let the magnetic field be

$$\mathbf{B} = B_0 \frac{r_0^2}{r^2} \hat{r} + b(\theta, r) \hat{\varphi}. \quad (6.19)$$

We define an aspect angle  $\beta$ :

$$\tan \beta = \frac{b(\theta, r)}{B_0 r_0^2 / r^2}. \quad (6.20)$$

Figure 6.7 illustrates  $\beta$  and  $\mathbf{K}$  for a conical flux rope. A way to calculate  $\mathbf{K}$  is to consider acceleration perpendicular to the velocity of a hypothetical particle moving exactly along

$\mathbf{B}$  with constant speed  $v_{\parallel}$ ,

$$a_{\perp} = \frac{v_{\parallel}^2}{R_c}, \quad \frac{1}{R_c} = \frac{a_{\perp}}{v_{\parallel}^2}, \quad (6.21)$$

where  $\mathbf{a}_{\perp}$  is inward. Therefore,  $\mathbf{K}$  can be written as

$$\mathbf{K} = -\frac{\mathbf{a}_{\perp}}{v_{\parallel}^2}. \quad (6.22)$$

We assume that  $v_{\parallel}$  is fixed, so  $\dot{\mathbf{v}}_{\parallel}$  is perpendicular to  $\mathbf{B}$ . Substituting  $\mathbf{a}_{\perp} = \dot{\mathbf{v}}_{\parallel}$  into eq. (6.22), we get

$$\mathbf{K} = -\frac{\dot{\mathbf{v}}_{\parallel}}{v_{\parallel}^2}. \quad (6.23)$$

In order to find  $\mathbf{v}_{\parallel}$  and  $\dot{\mathbf{v}}_{\parallel}$ , we first write  $\mathbf{v}_{\parallel}$  in spherical coordinates:

$$\mathbf{v}_{\parallel} = v_{\parallel}(\cos \beta \hat{r} + \sin \beta \hat{\varphi}). \quad (6.24)$$

Then  $\mathbf{v}_{\parallel}$  can be written in terms of Cartesian coordinates as:

$$\begin{aligned} \mathbf{v}_{\parallel} &= v_{\parallel}(\cos \beta \sin \theta \cos \varphi \hat{x} + \cos \beta \sin \theta \sin \varphi \hat{y} \\ &+ \cos \beta \cos \theta \hat{z} - \sin \beta \sin \varphi \hat{x} + \sin \beta \cos \varphi \hat{y}). \end{aligned} \quad (6.25)$$

The field line lies along a cone of constant  $\theta$ , but  $\varphi$  and  $\beta$  can change when moving along the field line. Then

$$\begin{aligned} \frac{\dot{\mathbf{v}}_{\parallel}}{v_{\parallel}} &= \dot{\varphi}[\cos \beta \sin \theta(-\sin \varphi \hat{x} + \cos \varphi \hat{y}) - \sin \beta(\cos \varphi \hat{x} + \sin \varphi \hat{y})] \\ &+ \dot{\beta}[-\sin \beta \sin \theta(\cos \varphi \hat{x} + \sin \varphi \hat{y}) - \sin \beta \cos \theta \hat{z} \\ &+ \cos \beta(-\sin \varphi \hat{x} + \cos \varphi \hat{y})], \end{aligned} \quad (6.26)$$

or in terms of spherical coordinates,

$$\frac{\dot{\mathbf{v}}_{\parallel}}{v_{\parallel}} = \dot{\varphi}[\cos \beta \sin \theta \hat{\varphi} - \sin \beta(\sin \theta \hat{r} + \cos \theta \hat{\theta})] + \dot{\beta}[-\sin \beta \hat{r} + \cos \beta \hat{\varphi}] \quad (6.27)$$

Note that  $r \sin \theta \dot{\varphi} = v_{\varphi} = v_{\parallel} \sin \beta$ . Replacing  $\dot{\varphi} = v_{\parallel} \sin \beta / (r \sin \theta)$ , and noting that  $\dot{\beta} = v_{\parallel} \cos \beta \beta'$  where  $\beta' \equiv \partial \beta / \partial r$  we have

$$\mathbf{K} = -\frac{\sin \beta}{r \sin \theta} \left( \cos \beta \sin \theta \hat{\varphi} - \sin \beta \cos \theta \hat{\theta} - \sin \beta \sin \theta \hat{r} \right) + \cos \beta \beta' [\sin \beta \hat{r} - \cos \beta \hat{\varphi}] \quad (6.28)$$

The magnetic field can be written in terms of  $\beta$  as

$$\frac{\mathbf{B}}{B} = \sin \beta \hat{\phi} + \cos \beta \hat{r}. \quad (6.29)$$

Then the  $\theta$ -component of  $\mathbf{K} \times \mathbf{B}/B$  is

$$\left( \mathbf{K} \times \frac{\mathbf{B}}{B} \right)_\theta = -\frac{\sin \beta}{r} - \cos \beta \beta' \quad (6.30)$$

Finally, the curvature drift along  $\hat{\theta}$  is

$$v_{c,\theta} = -\frac{mv_\parallel^2}{qB} \left( \frac{\sin \beta}{r} + \cos \beta \beta' \right). \quad (6.31)$$

Note that in our simulations,  $b \propto r^{-2}$ , so from eq. (6.20)  $\beta$  is constant with  $r$  and  $\beta' = 0$ . Thus the drift is inward for  $\beta > 0$ , or a positive Gaussian. Another approach for estimating the curvature drift (a Hamiltonian approach) can be found in Appendix C.

Now we consider the gradient drift. The gradient drift is given by (Krittinatham 2009)

$$\mathbf{v}_g = \frac{mv_\perp^2}{2qB} \frac{\mathbf{B} \times \vec{\nabla} B}{B^2} \quad (6.32)$$

For the  $\theta$ -component, we have

$$v_{g,\theta} = \frac{mv_\perp^2}{2qB} \frac{\sin \beta}{B} \frac{\partial B}{\partial r}, \quad (6.33)$$

where  $B = B_0 \sec \beta$ , then finally we have

$$v_{g,\theta} = \frac{mv_\perp^2}{qB} \sin \beta \left( -\frac{1}{r} + \frac{\tan \beta}{2} \beta' \right) \quad (6.34)$$

for the gradient drift velocity. In our simulations,  $\beta' = 0$ , and this is same as the result for the curvature drift, except  $v_\parallel^2 \rightarrow v_\perp^2$ .

## 6.3 Simulation of Collimation of Particle Beams by 2D Turbulent Structure

### 6.3.1 Pure 2D Turbulence

We now consider the more complicated situation of particles in pure 2D turbulence. In this case, the 2D structure is composed of islands of many sizes rather

than a single island. Also the topology of islands is irregular. We generate the potential of pure 2D random-phase turbulence by methods explained in Chapter 3. After generation of the potential we then traced the motion of protons. In this case, we simulated 5,000 protons of energy 10 GeV. The results are shown in Figure 6.8. The particles were initially uniformly distributed in a circle of radius 10 degrees. All particles began at  $r_0 = 0.05$  AU as measured from the center of the Sun. The ratio of the root-mean-squared fluctuating field  $b$  to  $B_0$  is 1.

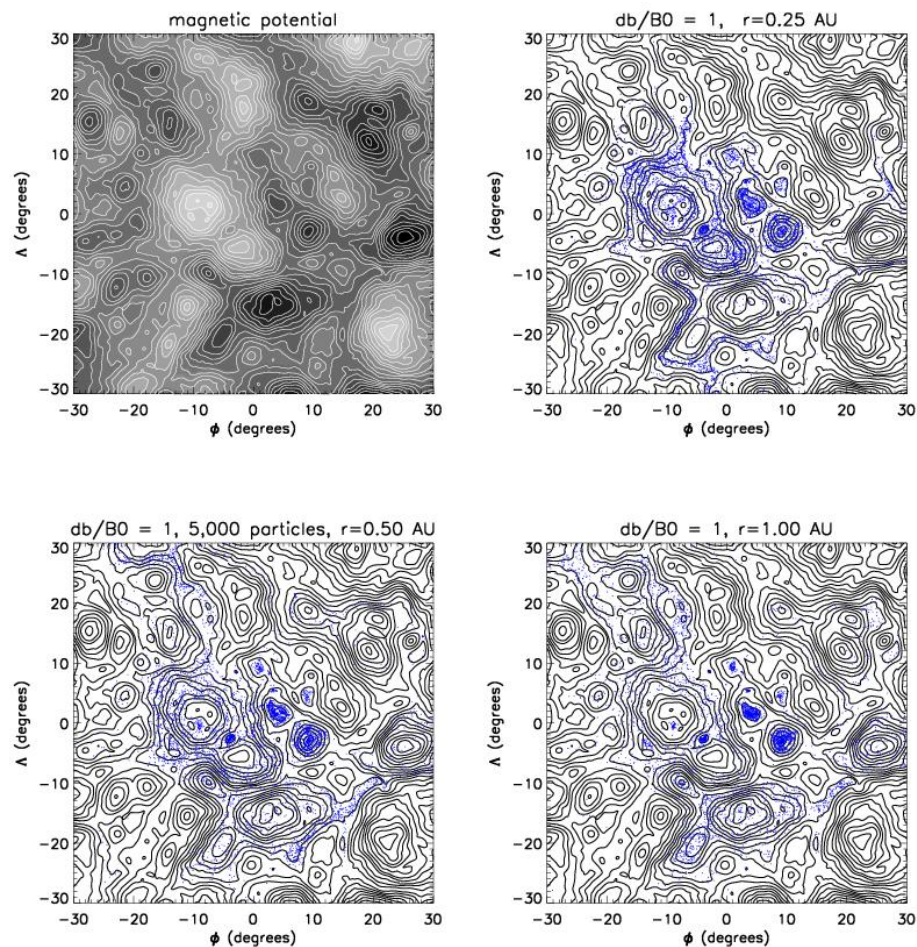


Figure 6.8: Scatter plots of 10 GeV proton trajectories at various distances. The upper left panel is a contour plot of the vector potential. Darker color indicates higher potential values and lighter color indicates lower potential values. The next panel is for particles at  $r = 0.25$  AU. The bottom left panel is for particles at 0.5 AU. The last panel is for particles at 1.0 AU.

From the results, we can see that particles are dramatically drawn toward



high potential and drifted away from low potential.

### 6.3.2 2D MHD + Slab Turbulence

Finally, we consider the most complicated situation, particles in 2D MHD + slab turbulence. We start with 5,000 magnetic field lines and protons in a circle of radius 10 degrees. Proton energies were 10 MeV, 3 GeV, and 10 GeV. Both magnetic field lines and particles started at  $r_0 = 0.05$  AU as measured from the center of the Sun. The ratio of slab energy to 2D energy is 20:80 and ratio of the root-mean-squared fluctuating field  $b$  to  $B_0$  is 0.5. The results of simulations are shown in Figure 6.9.

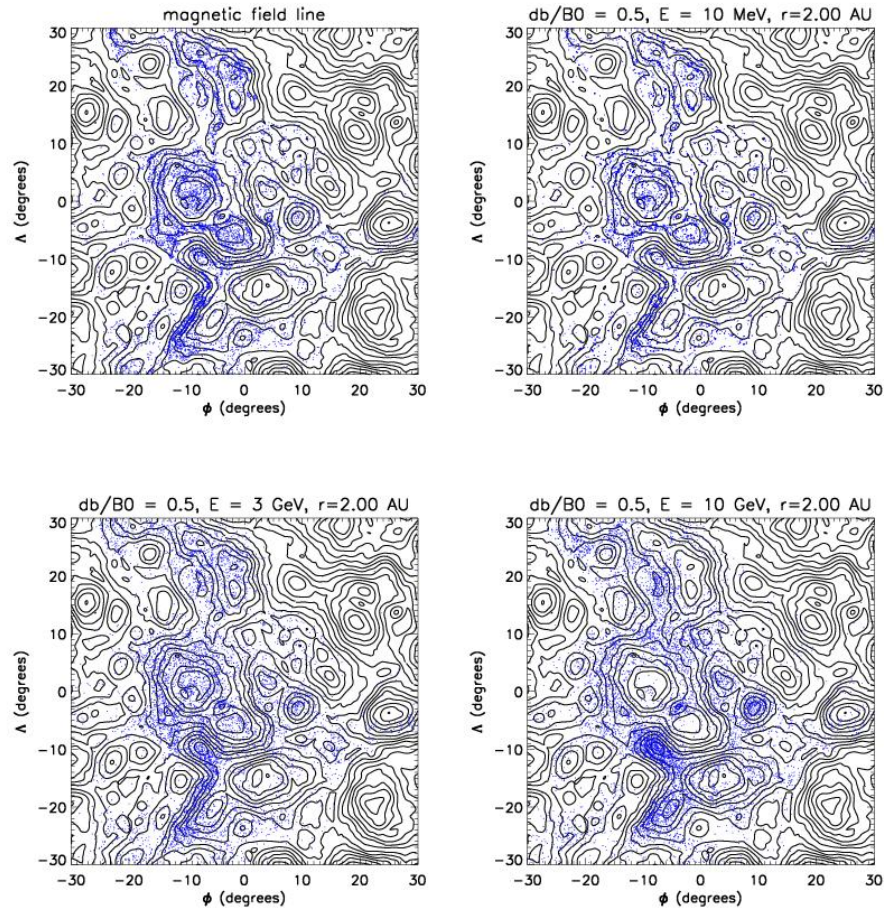


Figure 6.9: Scatter plots of magnetic field trajectories and proton trajectories for various energies at 2 AU. The upper left panel is a scatter plot of magnetic field lines. The upper right panel is for 10 MeV protons. The bottom left panel is for 3 GeV protons and the bottom right panel is for 10 GeV protons.

The magnetic field lines are spread out to both high and low potential regions. Protons of 10 MeV tightly follow the field lines, so the scatter plot looks similar to that for field lines. For protons of 3 GeV, there can be some accumulation at high potential. Protons of 10 GeV form collimated beams at potential maxima. In this case, we observed a lower collimation effect than for pure 2D turbulence, because particles can diffuse out from the island due to slab turbulence.

## CHAPTER VII

### CONCLUSIONS

Recent theoretical progress to explain SEP dropouts has identified mechanisms for sharp changes in field line connection from a source to an observing region at a distance of 1 AU, in the context of random-phase turbulence models. A viewpoint involving “spaghetti” of independent flux tubes has also been proposed to explain various discontinuities in solar wind plasma properties.

Here we improve a random-phase turbulence model by using a 2D MHD procedure. The 2D MHD model contains narrow current sheets and structures reminiscent of flux tubes, with non-Gaussian statistics for  $\mathbf{b}$  and  $\mathbf{j}$ . To the extent that flux tubes can be defined, they are not independent but rather coordinated with their neighbors to avoid strong changes in magnetic field along their boundaries, except at current sheets of narrow extent.

Our simulations indicate that magnetic field line trajectories to 1 AU serve as good proxies for arrival locations of protons up to 1 GeV in energy. Thus sharp changes in magnetic connection to a localized source are a proxy for SEP dropout features. We identified LTBs as 2D flux surfaces with maximal  $|b^{2D}|_{av}^2$  compared with neighboring flux surfaces. Our simulation results indicate that dropout features are frequently associated with LTBs, sometimes associated with strong 2D magnetic fluctuations, and only infrequently associated with current sheets. The mechanisms identified in the context of random-phase two-component fields can still explain dropout features with the 2D MHD model. In sum, we have developed a more realistic model of turbulent fluctuations in the solar wind, including current sheets, which is consistent with the poor association observed between dropout features and intense magnetic fields or currents.

Simulations in spherical geometry give us an interesting result: a “collima-

tion” effect. This is a process in which positively charged particles are shepherded to form beams along 2D potential maxima. The process is caused by curvature and gradient drifts. This should occur for relativistic SEP ions. Such particles are driven away from potential minima. We have demonstrated the effect of collimation in three cases: a single 2D Gaussian island, pure 2D turbulence and 2D+slab turbulence. We found that for protons of energy  $\geq 3$  GeV, the collimation effect can be observed. For future work, we will investigate whether this effect can be applied to understand observations of the highest energy SEPs.

## REFERENCES

- BEIBER, J. W., MATTHAEUS, W. H., SMITH, C. W., WANNER, W., KALLENRODE, M. & WIBBERENZ, G., 1994 “Proton and electron mean free paths: The Palmer consensus revisited,” *Astrophys. J.* **420**, 294–306.
- BIEBER, J. W., WANNER, W. & MATTHAEUS, W. H., 1996 “Dominant two-dimensional solar wind turbulence with implications for cosmic ray transport,” *J. Geophys. Res.* **101**, 2511–2522.
- BOROVSKY, J. E., 2008 “Flux tube texture of the solar wind: Strands of the magnetic carpet at 1 AU?” *J. Geophys. Res. (Space Physics)* **113**, 8110.
- BRUNO, R., CARBONE, V., VELTRI, P., PIETROPAOLO, E. & BAVASSANO, B., 2001 “Identifying intermittency events in the solar wind,” *Planet. Space Sci.* **49**, 1201–1210.
- CANE, H. V. & ERICKSON, W. C., 2003 “Energetic particle propagation in the inner heliosphere as deduced from low-frequency (100 kHz) observations of type III radio bursts,” *J. Geophys. Res. (Space Physics)* **108**, 1203.
- CANE, H. V., WIBBERENZ, G., RICHARDSON, I. G. & VON ROSENVINGE, T. T., 1999 “Cosmic ray modulation and the solar magnetic field,” *Geophys. Res. Lett.* **26**, 565–568.
- CHOLLET, E. E. & GIACALONE, J., 2008 “Multispacecraft Analysis of Energetic Ion Flux Dropouts,” *Astrophys. J.* **688**, 1368–1373.
- CHUYCHAI, P., RUFFOLO, D., MATTHAEUS, W. H. & MEECHAI, J., 2007 “Trapping and Diffusive Escape of Field Lines in Two-Component Magnetic Turbulence,” *Astrophys. J.* **659**, 1761–1776.
- CHUYCHAI, P., RUFFOLO, D., MATTHAEUS, W. H. & ROWLANDS, G., 2005 “Suppressed Diffusive Escape of Topologically Trapped Magnetic Field Lines,” *Astrophys. J. Lett.* **633**, L49–L52.
- COLEMAN, P. J., JR., 1968 “Turbulence, Viscosity, and Dissipation in the Solar-Wind Plasma,” *Astrophys. J.* **153**, 371.

- CRAVENS, T. E., 1997 *Physics of Solar System Plasmas* (Cambridge University Press, Cambridge).
- DASSO, S., MILANO, L. J., MATTHAEUS, W. H. & SMITH, C. W., 2005 “Anisotropy in Fast and Slow Solar Wind Fluctuations,” *Astrophys. J. Lett.* **635**, L181–L184.
- GIACALONE, J., JOKIPII, J. R. & MATTHAEUS, W. H., 2006 “Structure of the Turbulent Interplanetary Magnetic Field,” *Astrophys. J. Lett.* **641**, L61–L64.
- GIACALONE, J., JOKIPII, J. R. & MAZUR, J. E., 2000 “Small-scale Gradients and Large-scale Diffusion of Charged Particles in the Heliospheric Magnetic Field,” *Astrophys. J. Lett.* **532**, L75–L78.
- GOLDREICH, P. & SRIDHAR, S., 1995 “Toward a theory of interstellar turbulence. 2: Strong alfvénic turbulence,” *Astrophys. J.* **438**, 763–775.
- GOSLING, J. T., SKOUG, R. M., MCCOMAS, D. J. & MAZUR, J. E., 2004 “Correlated Dispersionless Structure in Suprathermal Electrons and Solar Energetic Ions in the Solar Wind,” *Astrophys. J.* **614**, 412–419.
- GRECO, A., MATTHAEUS, W. H., SERVIDIO, S., CHUYCHAI, P. & DMITRUK, P., 2009 “Statistical Analysis of Discontinuities in Solar Wind ACE Data and Comparison with Intermittent MHD Turbulence,” *Astrophys. J. Lett.* **691**, L111–L114.
- HIGDON, J. C., 1984 “Density fluctuations in the interstellar medium: Evidence for anisotropic magnetogasdynamic turbulence. I - Model and astrophysical sites,” *Astrophys. J.* **285**, 109–123.
- HOSSAIN, M., GRAY, P. C., PONTIUS, D. H., MATTHAEUS, W. H. & OUGHTON, S., 1996 “Is the Alfvén-wave propagation effect important for energy decay in homogeneous MHD turbulence?” in D. Winterhalter, J. T. Gosling, S. R. Habbal, W. S. Kurth, & M. Neugebauer, (ed.) *American Institute of Physics Conference Series*, vol. 382 of *American Institute of Physics Conference Series*, pp. 358–361.
- JOKIPII, J. R. & COLEMAN, P. J., JR., 1968 “Cosmic-Ray Diffusion Tensor and Its Variation Observed with Mariner 4,” *J. Geophys. Res.* **73**, 5495.
- JOKIPII, J. R. & PARKER, E. N., 1968 “Random Walk of Magnetic Lines of Force in Astrophysics,” *Phys. Rev. Lett.* **21**, 44–47.

- KAGHASHVILI, E. K., ZANK, G. P. & WEBB, G. M., 2006 “Propagation of Energetic Charged Particles in the Solar Wind: Effects of Intermittency in the Medium,” *Astrophys. J.* **636**, 1145–1150.
- KITTINARADORN, R., RUFFOLO, D. & MATTHAEUS, W. H., 2009 “Solar Moss Patterns: Heating of Coronal Loops by Turbulence and Magnetic Connection to the Footpoints,” *Astrophys. J. Lett.* **702**, L138–L142.
- KOLMOGOROV, A., 1941 “The Local Structure of Turbulence in Incompressible Viscous Fluid for Very Large Reynolds’ Numbers,” *Akademiia Nauk SSSR Doklady* **30**, 301–305.
- KRITTINATHAM, W., 2009 *Drift motions of energetic particles in an interplanetary magnetic cloud*, Ph.D. thesis, Mahidol University.
- LEAMON, R. J., SMITH, C. W., NESS, N. F., MATTHAEUS, W. H. & WONG, H. K., 1998 “Observational constraints on the dynamics of the interplanetary magnetic field dissipation range,” *J. Geophys. Res.* **103**, 4775.
- LI, G., 2008 “Identifying Current-Sheet-like Structures in the Solar Wind,” *Astrophys. J. Lett.* **672**, L65–L68.
- MATTHAEUS, W. H., BIEBER, J. W., RUFFOLO, D., CHUYCHAI, P. & MINNIE, J., 2007 “Spectral Properties and Length Scales of Two-dimensional Magnetic Field Models,” *Astrophys. J.* **667**, 956–962.
- MATTHAEUS, W. H., GOLDSTEIN, M. L. & ROBERTS, D. A., 1990 “Evidence for the presence of quasi-two-dimensional nearly incompressible fluctuations in the solar wind,” *J. Geophys. Res.* **95**, 20673–20683.
- MATTHAEUS, W. H., GRAY, P. C., PONTIUS, D. H., JR. & BIEBER, J. W., 1995 “Spatial Structure and Field-Line Diffusion in Transverse Magnetic Turbulence,” *Phys. Rev. Lett.* **75**, 2136–2139.
- MATTHAEUS, W. H. & LAMKIN, S. L., 1986 “Turbulent magnetic reconnection,” *Phys. Fluids* **29**, 2513–2534.
- MATTHAEUS, W. H. & MONTGOMERY, D., 1980 “Selective decay hypothesis at high mechanical and magnetic Reynolds numbers,” in *International Conference on Nonlinear Dynamics, New York, NY, Dec. 17-21, 1979.*, vol. 357, pp. 203–222.

- MATTHAEUS, W. H., SMITH, C. W. & OUGHTON, S., 1998 “Dynamical age of solar wind turbulence in the outer heliosphere,” *J. Geophys. Res.* **103**, 6495.
- MATTHAEUS, W. H., ZANK, G. P. & OUGHTON, S., 1996 “Phenomenology of hydro-magnetic turbulence in a uniformly expanding medium.” *J. Plasma Phys.* **56**, 659–675.
- MAZUR, J. E., MASON, G. M., DWYER, J. R., GIACALONE, J., JOKIPII, J. R. & STONE, E. C., 2000 “Interplanetary magnetic field line mixing deduced from impulsive solar flare particles,” *Astrophys. J. Lett.* **532**, L79–L82.
- MCCRACKEN, K. G. & NESS, N. F., 1966 “The Collimation of Cosmic Rays by the Interplanetary Magnetic Field,” *J. Geophys. Res.* **71**, 3315.
- MCKIBBEN, R. B., 2005 “Cosmic-ray diffusion in the inner heliosphere,” *Adv. in Space Res.* **35**, 518–531.
- MCKIBBEN, R. B., LOPATE, C. & ZHANG, M., 2001 “Simultaneous Observations of Solar Energetic Particle Events by imp 8 and the Ulysses Cospin High Energy Telescope at High Solar Latitudes,” *Space Science Reviews* **97**, 257–262.
- MEYER-VERNET, N., 2007 *Basics of The Solar Wind* (Cambridge University Press, Cambridge).
- MONTGOMERY, D., 1982 “Major disruptions, inverse cascades, and the Strauss equations,” *Physica Scripta* **2**, 83.
- MORAAL, H., 1976 “Observations of the eleven-year cosmic-ray modulation cycle,” *Space Science Reviews* **19**, 845–920.
- OSMAN, K. T. & HORBURY, T. S., 2007 “Multispacecraft Measurement of Anisotropic Correlation Functions in Solar Wind Turbulence,” *Astrophys. J. Lett.* **654**, L103–L106.
- OUGHTON, S., PRIEST, E. R. & MATTHAEUS, W. H., 1994 “The influence of a mean magnetic field on three-dimensional magnetohydrodynamic turbulence,” *J. Fluid Mech.* **280**, 95–117.
- PARKER, E. N., 1963a “The Solar-Flare Phenomenon and the Theory of Reconnection and Annihilation of Magnetic Fields.” *Astrophys. J. Supp.* **8**, 177.
- PARKER, E. N., 1963b *Interplanetary dynamical processes*. (Wiley Interscience, New York).



- PARKER, E. N., 1965 “The passage of energetic charged particles through interplanetary space,” *Planet. Space Sci.* **13**, 9.
- PETSCHEK, H. E., 1964 “Magnetic Field Annihilation,” *NASA Special Publication* **50**, 425.
- POMMOIS, P., ZIMBARDO, G. & VELTRI, P., 2005 “Energetic particle transport in anisotropic magnetic turbulence,” *Adv. in Space. Res.* **35**, 647–652.
- PRESS, W. H., TEUKOLSKY, S. A., VETTERLING, W. T. & FLANNERY, B. P., 1992 *Numerical recipes in FORTRAN: The art of scientific computing*, 2 edn. (Cambridge University Press, Cambridge).
- PRIEST, E., FORBES, T. & MURDIN, P., 2000 *Magnetohydrodynamics* (Cambridge University Press, Cambridge).
- PRIEST, E. R., 1994 “Magnetohydrodynamics,” in A. O. Benz & T. J.-L. Courvoisier, (ed.) *Saas-Fee Advanced Course 24: Plasma Astrophysics* (Springer-Verlag Berlin Heidelberg, Heidelberg).
- REAMES, D. V., 1992 “Trapping and Escape of the High Energy Particles Responsible for Major Proton Events,” in Z. Svestka, B. V. Jackson, & M. E. Machado, (ed.) *IAU Colloq. 133: Eruptive Solar Flares*, vol. 399 of *Lecture Notes in Physics*, Berlin Springer Verlag, p. 180.
- REAMES, D. V., CANE, H. V. & VON ROSENVINGE, T. T., 1990 “Energetic particle abundances in solar electron events,” *Astrophys. J.* **357**, 259–270.
- REINECKE, J. P. L., McDONALD, F. B. & MORAAL, H., 2000 “Cosmic radiation in the heliosphere at successive solar minima 5. Modulation of anomalous cosmic ray helium during the three consecutive solar minimum periods of 1977/1978, 1987, and 1997,” *J. Geophys. Res.* **105**, 27439–27446.
- ROELOF, E. C., 1969 “Propagation of Solar Cosmic Rays in the Interplanetary Magnetic Field,” in H. Ögelman & J. R. Wayland, (ed.) *Lectures in High-Energy Astrophysics*, p. 111.
- RUFFOLO, D., 2002 *Classical Mechanics* (Chulalongkorn University Press, Bangkok).
- RUFFOLO, D. & KHUMLUMLERT, T., 1995 “Formation, propagation, and decay of coherent pulses of solar cosmic rays,” *Geophys. Res. Lett.* **22**, 2073–2076.

- RUFFOLO, D., MATTHAEUS, W. H. & CHUYCHAI, P., 2003 “Trapping of solar energetic particles by the small-scale topology of solar wind turbulence,” *Astrophys. J. Lett.* **597**, L169–L172.
- RUFFOLO, D., MATTHAEUS, W. H. & CHUYCHAI, P., 2004 “Separation of Magnetic Field Lines in Two-Component Turbulence,” *Astrophys. J.* **614**, 420–434.
- SAHRAOUI, F., GOLDSTEIN, M. L., ROBERT, P. & KHOTYAINTEV, Y. V., 2009 “Evidence of a Cascade and Dissipation of Solar-Wind Turbulence at the Electron Gyroscale,” *Phys. Rev. Lett.* **102**, 231102.
- SAUR, J. & BIEBER, J. W., 1999 “Geometry of low-frequency solar wind magnetic turbulence: Evidence for radially aligned Alfvénic fluctuations,” *J. Geophys. Res.* **104**, 9975–9988.
- SERVIDIO, S., MATTHAEUS, W. H. & DMITRUK, P., 2008 “Depression of Nonlinearity in Decaying Isotropic MHD Turbulence,” *Phys. Rev. Lett.* **100**, 095005.
- SHALCHI, A., BIEBER, J. W. & MATTHAEUS, W. H., 2008 “Pitch-angle scattering in pure two-dimensional and two-component turbulence,” **483**, 371–381.
- SHEBALIN, J. V., MATTHAEUS, W. H. & MONTGOMERY, D., 1983 “Anisotropy in MHD turbulence due to a mean magnetic field,” *J. Plasma Phys.* **29**, 525–547.
- SMITH, C. W., MATTHAEUS, W. H., ZANK, G. P., NESS, N. F., OUGHTON, S. & RICHARDSON, J. D., 2001 “Heating of the low-latitude solar wind by dissipation of turbulent magnetic fluctuations,” *J. Geophys. Res.* **106**, 8253–8272.
- SWEET, P. A., 1958 “The Neutral Point Theory of Solar Flares,” in B. Lehnert, (ed.) *Electromagnetic Phenomena in Cosmical Physics*, vol. 6 of *IAU Symposium*, p. 123.
- TENNEKES, H. & LUMLEY, J. L., 1972 *A First Course in Turbulence* (The MIT Press, Cambridge).
- TOOPRAKAI, P., CHUYCHAI, P., MINNIE, J., RUFFOLO, D., BIEBER, J. W. & MATTHAEUS, W. H., 2007 “Temporary topological trapping and escape of charged particles in a flux tube as a cause of delay in time asymptotic transport,” *Geophys. Res. Lett.* **34**, L17105.

- VERMA, M. K., ROBERTS, D. A. & GOLDSTEIN, M. L., 1995 “Turbulent heating and temperature evolution in the solar wind plasma,” *J. Geophys. Res.* **100**, 19839–19850.
- WAN, M., OUGHTON, S., SERVIDIO, S. & MATTHAEUS, W. H., 2009 “Generation of non-Gaussian statistics and coherent structures in ideal magnetohydrodynamics,” *Phys. Plasmas* **16**, 080703.
- WEYGAND, J. M., MATTHAEUS, W. H., DASSO, S., KIVELSON, M. G., KISTLER, L. M. & MOUIKIS, C., 2009 “Anisotropy of the Taylor scale and the correlation scale in plasma sheet and solar wind magnetic field fluctuations,” *J. Geophys. Res. (Space Physics)* **114**, 7213.
- ZIMBARDO, G., POMMOIS, P. & VELTRI, P., 2004 “Magnetic flux tube evolution in solar wind anisotropic magnetic turbulence,” *J. Geophys. Res. (Space Physics)* **109**, 2113.

## APPENDICES

## APPENDIX A

### NON-DIMENSIONALIZATION

The motion of a charged particle in a uniform magnetic field is governed by the Newton-Lorentz equation, which is

$$\frac{d\mathbf{v}}{dt} = \frac{q}{\gamma m} \mathbf{v} \times \mathbf{B}. \quad (\text{A.1})$$

In terms of components, we have

$$\frac{dv_x}{dt} = \frac{q}{\gamma m} (v_y B_z - B_y v_z) \quad (\text{A.2})$$

$$\frac{dv_y}{dt} = \frac{q}{\gamma m} (v_z B_x - B_z v_x) \quad (\text{A.3})$$

$$\frac{dv_z}{dt} = \frac{q}{\gamma m} (v_x B_y - B_x v_y). \quad (\text{A.4})$$

We normalized these equations by the speed of light  $c$ , the mean magnetic field  $B_0$ , and the slab bendover scale  $\lambda$ . In order to do that we use dimensionless variables:

$$\mathbf{v}^* = \frac{\mathbf{v}}{c}, \quad (\text{A.5})$$

$$\mathbf{B}^* = \frac{\mathbf{B}}{B_0}, \quad (\text{A.6})$$

$$t^* = \frac{t}{\tau_c}, \quad (\text{A.7})$$

where  $\tau_c = \lambda/c$ . Substituting eqs. (A.5) - (A.7) into (A.2) - (A.4), we get

$$\frac{dv_x^*}{dt^*} = \frac{qB_0\tau_c}{\gamma m} (v_y^* B_z^* - B_y^* v_z^*), \quad (\text{A.8})$$

$$\frac{dv_y^*}{dt^*} = \frac{qB_0\tau_c}{\gamma m} (v_z^* B_x^* - B_z^* v_x^*), \quad (\text{A.9})$$

$$\frac{dv_z^*}{dt^*} = \frac{qB_0\tau_c}{\gamma m} (v_x^* B_y^* - B_x^* v_y^*). \quad (\text{A.10})$$

We introduce  $\alpha = qB_0\tau_c/(\gamma m)$ , and then eqs. (A.8) - (A.10) become

$$\frac{dv_x^*}{dt^*} = \alpha (v_y^* B_z^* - B_y^* v_z^*), \quad (\text{A.11})$$

$$\frac{dv_y^*}{dt^*} = \alpha (v_z^* B_x^* - B_z^* v_x^*), \quad (\text{A.12})$$

$$\frac{dv_z^*}{dt^*} = \alpha (v_x^* B_y^* - B_x^* v_y^*). \quad (\text{A.13})$$

This method can be used both in Cartesian and spherical geometry.

## APPENDIX B

### DERIVATION OF EQUATIONS OF PARTICLE MOTION IN SPHERICAL GEOMETRY

In terms of our preferred coordinates  $(\varphi, \Lambda, r)$ , the Lagrangian for a charged particle in a static magnetic field is (Ruffolo 2002)

$$\mathcal{L} = \frac{m}{2}(\dot{r}^2 + r^2\dot{\Lambda}^2 + r^2 \cos^2 \Lambda \dot{\varphi}^2) + q\dot{r}A_r + qr\dot{\Lambda}A_\Lambda + qr \cos \Lambda \dot{\varphi}A_\varphi. \quad (\text{B.1})$$

We find  $p_i \equiv \partial\mathcal{L}/\partial\dot{q}_i$ :

$$p_\varphi = \frac{\partial\mathcal{L}}{\partial\dot{\varphi}} = mr^2 \cos^2 \Lambda \dot{\varphi} + qr \cos \Lambda A_\varphi \quad (\text{B.2})$$

$$p_\Lambda = \frac{\partial\mathcal{L}}{\partial\dot{\Lambda}} = mr^2 \dot{\Lambda} + qr A_\Lambda \quad (\text{B.3})$$

$$p_r = \frac{\partial\mathcal{L}}{\partial\dot{r}} = m\dot{r} + qA_r. \quad (\text{B.4})$$

Then  $\dot{\varphi}$ ,  $\dot{\Lambda}$ , and  $\dot{r}$  are

$$\dot{\varphi} = \frac{p_\varphi - qr \cos \Lambda A_\varphi}{mr^2 \cos^2 \Lambda} \quad (\text{B.5})$$

$$\dot{\Lambda} = \frac{p_\Lambda - qr A_\Lambda}{mr^2} \quad (\text{B.6})$$

$$\dot{r} = \frac{p_r - qA_r}{m}. \quad (\text{B.7})$$

The Hamiltonian,  $H \equiv \sum p_i \dot{q}_i - \mathcal{L}$ , is

$$H = \frac{(p_r - qA_r)^2}{2m} + \frac{(p_\Lambda - qr A_\Lambda)^2}{2mr^2} + \frac{(p_\varphi - qr \cos \Lambda A_\varphi)^2}{2mr^2 \cos^2 \Lambda}, \quad (\text{B.8})$$

where  $A$  depends on the position. Then Hamilton's equations are

$$\begin{aligned} \dot{p}_\varphi = -\frac{\partial H}{\partial \varphi} &= \frac{(p_r - qA_r)}{m} \left( q \frac{\partial A_r}{\partial \varphi} \right) + \frac{(p_\Lambda - qrA_\Lambda)}{mr} \left( q \frac{\partial A_\Lambda}{\partial \varphi} \right) \\ &+ \frac{(p_\varphi - qr \cos \Lambda A_\varphi)}{mr \cos \Lambda} \left( q \frac{\partial A_\varphi}{\partial \varphi} \right) \end{aligned} \quad (\text{B.9})$$

$$\begin{aligned} \dot{p}_\Lambda = -\frac{\partial H}{\partial \Lambda} &= \frac{(p_r - qA_r)}{m} \left( q \frac{\partial A_r}{\partial \Lambda} \right) + \frac{(p_\Lambda - qrA_\Lambda)}{mr^2} \left( qr \frac{\partial A_\Lambda}{\partial \Lambda} \right) \\ &+ \frac{(p_\varphi - qr \cos \Lambda A_\varphi)}{mr^2 \cos^2 \Lambda} \left( -qr \sin \Lambda A_\varphi + qr \cos \Lambda \frac{\partial A_\varphi}{\partial \Lambda} \right) \\ &- \frac{(p_\varphi - qr \cos \Lambda A_\varphi)^2}{(mr^2 \cos^2 \Lambda)^2} (mr^2 \cos \Lambda \sin \Lambda) \end{aligned} \quad (\text{B.10})$$

$$\begin{aligned} \dot{p}_r = -\frac{\partial H}{\partial r} &= \frac{(p_r - qA_r)}{m} \left( q \frac{\partial A_r}{\partial r} \right) + \frac{(p_\Lambda - qrA_\Lambda)}{mr^2} \left( qA_\Lambda + qr \frac{\partial A_\Lambda}{\partial r} \right) \\ &+ mr \frac{(p_\Lambda - qrA_\Lambda)^2}{(mr^2)^2} \\ &+ \frac{(p_\varphi - qr \cos \Lambda A_\varphi)}{mr^2 \cos^2 \Lambda} \left( q \cos \Lambda A_\varphi + q \cos \Lambda r \frac{\partial A_\varphi}{\partial r} \right) \\ &+ \frac{(p_\varphi - qr \cos \Lambda A_\varphi)^2}{mr^3 \cos^2 \Lambda} \end{aligned} \quad (\text{B.11})$$

$$\dot{\varphi} = \frac{\partial H}{\partial p_\varphi} = \frac{p_\varphi - qr \cos \Lambda A_\varphi}{mr^2 \cos^2 \Lambda} \quad (\text{B.12})$$

$$\dot{\Lambda} = \frac{\partial H}{\partial p_\Lambda} = \frac{p_\Lambda - qrA_\Lambda}{mr^2} \quad (\text{B.13})$$

$$\dot{r} = \frac{\partial H}{\partial p_r} = \frac{p_r - qA_r}{m}. \quad (\text{B.14})$$

Recall that the velocity components are defined by

$$v_\varphi = r \cos \Lambda \dot{\varphi} \quad (\text{B.15})$$

$$v_\Lambda = r \dot{\Lambda} \quad (\text{B.16})$$

$$v_r = \dot{r}. \quad (\text{B.17})$$

Writing (B.2) - (B.4) in terms of  $v_i$ ,

$$p_\varphi = mr \cos \Lambda v_\varphi + qr \cos \Lambda A_\varphi \quad (\text{B.18})$$

$$p_\Lambda = mr v_\Lambda + qr A_\Lambda \quad (\text{B.19})$$

$$p_r = mv_r + qA_r. \quad (\text{B.20})$$



Then taking derivatives with respect to time we get

$$\begin{aligned} \dot{p}_\varphi &= m(\cos \Lambda v_r v_\varphi - \sin \Lambda v_\Lambda v_\varphi + r \cos \Lambda \dot{v}_\varphi) \\ &+ q \left[ \cos \Lambda v_r A_\varphi - \sin \Lambda v_\Lambda A_\varphi + r \cos \Lambda \left( \dot{r} \frac{\partial A_\varphi}{\partial r} + \dot{\Lambda} \frac{\partial A_\varphi}{\partial \Lambda} + \dot{\varphi} \frac{\partial A_\varphi}{\partial \varphi} \right) \right] \end{aligned} \quad (\text{B.21})$$

$$\dot{p}_\Lambda = m v_r v_\Lambda + m r \dot{v}_\Lambda + q v_r A_\Lambda + q r \left( \dot{r} \frac{\partial A_\Lambda}{\partial r} + \dot{\Lambda} \frac{\partial A_\Lambda}{\partial \Lambda} + \dot{\varphi} \frac{\partial A_\Lambda}{\partial \varphi} \right) \quad (\text{B.22})$$

$$\dot{p}_r = m \dot{v}_r + q \left( \dot{r} \frac{\partial A_r}{\partial r} + \dot{\Lambda} \frac{\partial A_r}{\partial \Lambda} + \dot{\varphi} \frac{\partial A_r}{\partial \varphi} \right) \quad (\text{B.23})$$

We can find the magnetic field from taking the curl of the vector potential  $\mathbf{A}$ ,

$$\begin{aligned} \nabla \times \mathbf{A} &= \frac{1}{r^2 \cos \Lambda} \left( \frac{\partial A_r}{\partial \Lambda} - \frac{\partial(r A_r)}{\partial r} \right) r \cos \Lambda \hat{\varphi}, \\ &+ \frac{1}{r^2 \cos \Lambda} \left( \frac{\partial(r \cos \Lambda A_\varphi)}{\partial r} - \frac{\partial A_r}{\partial A_r} \right) r \hat{\Lambda}, \\ &+ \frac{1}{r^2 \cos \Lambda} \left( \frac{\partial(r A_\Lambda)}{\partial \varphi} - \frac{\partial(r \cos \Lambda A_\varphi)}{\partial \Lambda} \right) \hat{r}, \end{aligned} \quad (\text{B.24})$$

or in terms of components,

$$B_\varphi = \frac{1}{r} \left( \frac{\partial A_r}{\partial \Lambda} - \frac{\partial(r A_\Lambda)}{\partial r} \right) = \frac{1}{r} \frac{\partial A_r}{\partial \Lambda} - \frac{A_\Lambda}{r} - \frac{\partial A_\Lambda}{\partial r}, \quad (\text{B.25})$$

$$B_\Lambda = \frac{1}{r} \left( \frac{\partial(r A_\varphi)}{\partial r} - \frac{1}{\cos \Lambda} \frac{\partial A_r}{\partial \varphi} \right) = \frac{A_\varphi}{r} + \frac{\partial A_\varphi}{\partial r} - \frac{1}{r \cos \Lambda} \frac{\partial A_r}{\partial \varphi}, \quad (\text{B.26})$$

$$B_r = \frac{1}{r \cos \Lambda} \left( \frac{\partial A_\Lambda}{\partial \varphi} - \frac{\partial(\cos \Lambda A_\varphi)}{\partial \Lambda} \right) = \frac{1}{r \cos \Lambda} \frac{\partial A_\Lambda}{\partial \varphi} + \frac{\sin \Lambda A_\varphi}{r \cos \Lambda} - \frac{1}{r} \frac{\partial A_\varphi}{\partial \Lambda}. \quad (\text{B.27})$$

Equating eqs. (B.9) - (B.11) with eqs. (B.21) - (B.23), using (B.25) - (B.27) and rewriting in terms of  $\dot{v}_i$ , we will get

$$\begin{aligned} v_r \left( q \frac{\partial A_r}{\partial \varphi} \right) + v_\Lambda \left( q \frac{\partial A_\Lambda}{\partial \varphi} \right) + v_\varphi \left( q \frac{\partial A_\varphi}{\partial \varphi} \right) &= m(\cos \Lambda v_r v_\varphi - \sin \Lambda v_\Lambda v_\varphi + r \cos \Lambda \dot{v}_\varphi) \\ &+ q \cos \Lambda v_r A_\varphi - q \sin \Lambda v_\Lambda A_\varphi + q r \cos \Lambda v_r \frac{\partial A_\varphi}{\partial r} \\ &+ q \cos \Lambda v_\Lambda \frac{\partial A_\varphi}{\partial \Lambda} + q v_\varphi \frac{\partial A_\varphi}{\partial \varphi} \end{aligned}$$

$$\begin{aligned} r \cos \Lambda \dot{v}_\varphi &= v_r \left( \frac{q}{m} \frac{\partial A_r}{\partial \varphi} \right) + v_\Lambda \left( \frac{q}{m} \frac{\partial A_\Lambda}{\partial \varphi} \right) - \frac{q}{m} \cos \Lambda v_r A_\varphi + \frac{q}{m} \sin \Lambda v_\Lambda A_\varphi \\ &- \frac{q}{m} r \cos \Lambda v_r \frac{\partial A_\varphi}{\partial r} - \frac{q}{m} \cos \Lambda v_\Lambda \frac{\partial A_\varphi}{\partial \Lambda} - \cos \Lambda v_r v_\varphi + \sin \Lambda v_\Lambda v_\varphi \end{aligned}$$

$$\begin{aligned}
\dot{v}_\varphi &= \frac{q}{m} \left[ v_r \left( \frac{1}{r \cos \Lambda} \frac{\partial A_r}{\partial \varphi} - \frac{A_\varphi}{r} - \frac{\partial A_\varphi}{\partial r} \right) + v_\Lambda \left( \frac{1}{r \cos \Lambda} \frac{\partial A_\Lambda}{\partial \varphi} + \frac{\sin \Lambda A_\varphi}{r \cos \Lambda} - \frac{1}{r} \frac{\partial A_\varphi}{\partial \Lambda} \right) \right] \\
&\quad - \frac{v_r v_\varphi}{r} + \frac{v_\Lambda v_\varphi}{r \cot \Lambda} \\
\dot{v}_\varphi &= -\frac{v_r v_\varphi}{r} + \frac{v_\Lambda v_\varphi}{r \cot \Lambda} + \frac{q}{m} (v_\Lambda B_r - B_\Lambda v_r) \tag{B.28}
\end{aligned}$$

$$\begin{aligned}
&v_r \left( q \frac{\partial A_r}{\partial \Lambda} \right) + v_\Lambda \left( q \frac{\partial A_\Lambda}{\partial \Lambda} \right) + v_\varphi \left( -q \frac{\sin \Lambda}{\cos \Lambda} A_\varphi + q \frac{\partial A_\varphi}{\partial \Lambda} \right) - v_\varphi^2 m \frac{\sin \Lambda}{\cos \Lambda} \\
&= m v_r v_\Lambda + m r \dot{v}_\Lambda + q v_r A_\Lambda + q r v_r \frac{\partial A_\Lambda}{\partial r} + q v_\Lambda \frac{\partial A_\Lambda}{\partial \Lambda} + q \frac{v_\varphi}{\cos \Lambda} \frac{\partial A_\Lambda}{\partial \varphi}
\end{aligned}$$

$$\begin{aligned}
\dot{v}_\Lambda &= \frac{v_r}{r} \left( \frac{q}{m} \frac{\partial A_r}{\partial \Lambda} \right) + v_\varphi \left( -\frac{q}{m} \frac{\sin \Lambda}{r \cos \Lambda} A_\varphi + \frac{q}{m} \frac{1}{r} \frac{\partial A_\varphi}{\partial \Lambda} \right) - \frac{v_\varphi^2 \sin \Lambda}{r \cos \Lambda} \\
&\quad - \frac{v_r v_\Lambda}{r} - \frac{q}{m} v_r \frac{A_\Lambda}{r} - \frac{q}{m} v_r \frac{\partial A_\Lambda}{\partial r} - \frac{q}{m} \frac{v_\varphi}{r \cos \Lambda} \frac{\partial A_\Lambda}{\partial \varphi} \\
&= \frac{q}{m} \left[ v_r \left( \frac{1}{r} \frac{\partial A_r}{\partial \Lambda} - \frac{A_\Lambda}{r} - \frac{\partial A_\Lambda}{\partial r} \right) + v_\varphi \left( -\frac{\sin \Lambda}{r \cos \Lambda} A_\varphi + \frac{1}{r} \frac{\partial A_\varphi}{\partial \Lambda} - \frac{1}{r \cos \Lambda} \frac{\partial A_\Lambda}{\partial \varphi} \right) \right] \\
&\quad - \frac{v_\varphi^2}{r \cot \Lambda} - \frac{v_r v_\Lambda}{r} \\
\dot{v}_\Lambda &= -\frac{v_\varphi^2}{r \cot \Lambda} - \frac{v_r v_\Lambda}{r} + \frac{q}{m} (v_r B_\varphi - v_\varphi B_r) \tag{B.29}
\end{aligned}$$

$$\begin{aligned}
v_r \left( q \frac{\partial A_r}{\partial r} \right) &+ \frac{v_\Lambda}{r} \left( q A_\Lambda + q r \frac{\partial A_\Lambda}{\partial r} \right) + m \frac{v_\Lambda^2}{r} + m \frac{v_\varphi^2}{r} + \frac{v_\varphi}{r \cos \Lambda} \left( q \cos \Lambda A_\varphi + q \cos \Lambda r \frac{\partial A_\varphi}{\partial r} \right) \\
&= m \dot{v}_r + q v_r \frac{\partial A_r}{\partial r} + q \frac{v_\Lambda}{r} \frac{\partial A_r}{\partial \Lambda} + q \frac{v_\varphi}{r \cos \Lambda} \frac{\partial A_r}{\partial \varphi}
\end{aligned}$$

$$\begin{aligned}
\dot{v}_r &= \frac{q}{m} \left[ v_\Lambda \left( \frac{A_\Lambda}{r} + \frac{\partial A_\Lambda}{\partial r} - \frac{1}{r} \frac{\partial A_r}{\partial \Lambda} \right) + v_\varphi \left( \frac{A_\varphi}{r} + \frac{\partial A_\varphi}{\partial r} - \frac{1}{r \cos \Lambda} \frac{\partial A_\varphi}{\partial \Lambda} \right) \right] \\
&\quad + \frac{v_\Lambda^2}{r} + \frac{v_\varphi^2}{r} \\
\dot{v}_r &= \frac{v_\Lambda^2}{r} + \frac{v_\varphi^2}{r} + \frac{q}{m} (v_\varphi B_\Lambda - v_\Lambda B_\varphi). \tag{B.30}
\end{aligned}$$

We take special relativity into account by converting  $m$  to  $\gamma m$ :

$$\dot{v}_\varphi = -\frac{v_r v_\varphi}{r} + \frac{v_\Lambda v_\varphi}{r \cot \Lambda} + \frac{q}{\gamma m} (v_\Lambda B_r - B_\Lambda v_r) \tag{B.31}$$

$$\dot{v}_\Lambda = -\frac{v_\varphi^2}{r \cot \Lambda} - \frac{v_r v_\Lambda}{r} + \frac{q}{\gamma m} (v_r B_\varphi - v_\varphi B_r) \tag{B.32}$$

$$\dot{v}_r = \frac{v_\Lambda^2}{r} + \frac{v_\varphi^2}{r} + \frac{q}{\gamma m} (v_\varphi B_\Lambda - v_\Lambda B_\varphi). \tag{B.33}$$

In the program, we solve eqs. (B.31) - (B.33) and the following forms of eqs. (B.15) - (B.17).

$$\dot{\varphi} = \frac{v_{\varphi}}{r \cos \Lambda} \quad (\text{B.34})$$

$$\dot{\Lambda} = \frac{v_{\Lambda}}{r} \quad (\text{B.35})$$

$$\dot{r} = v_r. \quad (\text{B.36})$$

## APPENDIX C

### CURVATURE DRIFT IN A CONICAL FLUX ROPE: HAMILTONIAN APPROACH

Suppose a charged particle moves in a conical flux rope. We will set up  $\mathbf{B}$  and  $\mathbf{A}$  for twist along conical flux surfaces. As in Section 6.1.2, we use spherical coordinates with  $\theta = 0$  along the central axis of the conical flux rope. Here we use a Hamiltonian approach to derive the same result for the curvature drift as in Section 6.1.2.

For  $(B_0 r_0^2 / r^2) \hat{r}$ , we use  $\mathbf{A}$  along  $\hat{\varphi}$ :

$$\begin{aligned}
 \frac{1}{r \sin \theta} \left( \frac{\partial(\sin \theta A_\varphi)}{\partial \theta} \right) &= B_r = \frac{B_0 r_0^2}{r^2} \\
 \frac{\partial(\sin \theta A_\varphi)}{\partial \theta} &= \frac{B_0 r_0^2}{r} \sin \theta \\
 -\sin \theta A_\varphi &= \frac{B_0 r_0^2}{r} \cos \theta \\
 A_\varphi &= -\frac{B_0 r_0^2 \cot \theta}{r}.
 \end{aligned} \tag{C.1}$$

Then we add twist along conical flux surfaces,  $b_\varphi(\theta, r)$ , using  $A_r(\theta, r)$ .

Recalling the Hamiltonian for a charged particle moving in a magnetic field, eq. (B.8), we obtain

$$H = \frac{(p_r - qA_r)^2}{2m} + \frac{(p_\theta - qrA_\theta)^2}{2mr^2} + \frac{(p_\varphi - qr \sin \theta A_\varphi)^2}{2mr^2 \sin^2 \theta}. \tag{C.2}$$

In this case, our Hamiltonian becomes

$$H = \frac{[p_r - qA_r(\theta, r)]^2}{2m} + \frac{p_\theta^2}{2mr^2} + \frac{(p_\varphi + qB_0 r_0^2 \cos \theta)^2}{2mr^2 \sin^2 \theta}. \tag{C.3}$$

The Hamilton equations are

$$\dot{r} = \frac{\partial H}{\partial p_r} = \frac{p_r - qA_r}{m} \quad (\text{C.4})$$

$$\dot{\theta} = \frac{\partial H}{\partial p_\theta} = \frac{p_\theta}{mr^2} \quad (\text{C.5})$$

$$\dot{\varphi} = \frac{\partial H}{\partial p_\varphi} = \frac{p_\varphi + qB_0r_0^2 \cos \theta}{mr^2 \sin^2 \theta} \quad (\text{C.6})$$

$$\dot{p}_r = -\frac{\partial H}{\partial r} = q \frac{\partial A_r}{\partial r} \frac{[p_r - qA_r(\theta, r)]}{m} + \frac{p_\theta^2}{mr^3} + \frac{(p_\varphi + qB_0r_0^2 \sin \theta)^2}{mr^3 \sin^2 \theta} \quad (\text{C.7})$$

$$\begin{aligned} \dot{p}_\theta = -\frac{\partial H}{\partial \theta} &= q \frac{\partial A_r(\theta, r)}{\partial \theta} \frac{[p_r - qA_r(\theta, r)]}{m} + \frac{qB_0r_0^2(p_\varphi + qB_0r_0^2 \cos \theta)}{mr^2 \sin \theta} \\ &+ \frac{\cos \theta (p_\varphi + qB_0r_0^2 \cos \theta)^2}{mr^2 \sin^3 \theta} \end{aligned} \quad (\text{C.8})$$

$$\dot{p}_\varphi = -\frac{\partial H}{\partial \varphi} = 0. \quad (\text{C.9})$$

Considering eq. (C.6), we can write

$$p_\varphi = mr^2 \sin^2 \theta \dot{\varphi} - q \cos \theta B_0r_0^2. \quad (\text{C.10})$$

We also have

$$r \sin \theta \dot{\varphi} = v_\varphi = v_{\parallel} \sin \beta. \quad (\text{C.11})$$

Using eq. (C.11), then eq. (C.10) can be written as

$$p_\varphi = \text{constant} = mr \sin \theta v_{\parallel} \sin \beta - q \cos \theta B_0r_0^2. \quad (\text{C.12})$$

Taking the time derivative of eq. (C.12), assuming as in section 6.1.2 that  $v_{\parallel}$  is constant,

$$\begin{aligned} \dot{p}_\varphi &= m\dot{r} \sin \theta v_{\parallel} \sin \beta + mr \cos \theta \dot{\theta} v_{\parallel} \sin \beta \\ &+ mr \sin \theta v_{\parallel} \cos \beta \dot{\beta} + q \sin \theta \dot{\theta} B_0r_0^2 \\ &= 0. \end{aligned} \quad (\text{C.13})$$

Comparing the two terms with  $\dot{\theta}$ , and noting that  $B_0r_0^2 = B_r r^2$ , we have

$$\frac{q \sin \theta B_0r_0^2}{mr \cos \theta v_{\parallel} \sin \beta} = \frac{\gamma v}{v_{\parallel}} \frac{r \tan \theta}{R_L \sin \beta}, \quad (\text{C.14})$$

where  $R_L$  is the gyroradius along the axis of the conical flux rope, for  $\mathbf{B} = B_r \hat{r}$ . We assume  $r \gg R_L$ , so the second term with  $\dot{\theta}$  in eq. (C.13) dominates over the first. We

use  $\dot{r} = v_{\parallel} \cos \beta$  and  $\dot{\beta} = v_{\parallel} \cos \beta \beta'$ . Then eq. (C.13) becomes

$$q \sin \theta \dot{\theta} B_r r^2 = -m v_{\parallel}^2 \cos \beta \sin \theta \sin \beta - m r \sin \theta v_{\parallel}^2 \cos^2 \beta \beta' \quad (\text{C.15})$$

We can write  $\dot{\theta}$  at the  $r$  of interest, using  $r_0 = r$  and  $B_r = B \cos \beta$ , as

$$\dot{\theta} = -\frac{m v_{\parallel}^2 (\sin \beta + r \cos \beta \beta')}{q B r^2}. \quad (\text{C.16})$$

Then  $v_{\theta}$  can be written as

$$v_{\theta} = r \dot{\theta} = -\frac{m v_{\parallel}^2 (\sin \beta + r \cos \beta \beta')}{q B r}, \quad (\text{C.17})$$

which is same as the curvature drift calculated in Section 6.1.2.

## BIOGRAPHY

<b>NAME</b>	Ms. Achara Seripienlert
<b>DATE OF BIRTH</b>	26th August 1981
<b>PLACE OF BIRTH</b>	Bangkok, Thailand
<b>INSTITUTIONS ATTENDED</b>	Thammasat University, 1999–2002 Bachelor of Science (Physics) Mahidol University, 2003–2006 Master of Science (Physics) Mahidol University, 2006–Present Doctor of Philosophy (Physics)
<b>HOME ADDRESS</b>	293 Bangkok-Nonthaburi Road, Bangsue Bangkok 10800 Thailand
<b>E-MAIL</b>	achara.seri@gmail.com